

REPORT DOCUMENTATION PAGE

AFRL-SR-BL-TR-98-

9

Public reporting burden for this collection of information is estimated to average 1 hour per response gathering and maintaining the data needed, and completing and reviewing the collection of information, including suggestions for reducing this burden, to Washington Headquarters, Davis Highway, Suite 1204, Arlington, VA 22202-4302, and to the Office of Management and Budget, Paperwork Project (0704-0188), Washington, DC 20503.

0702

data sources,
aspect of this
reports, 1215 Jefferson

1. AGENCY USE ONLY (Leave blank)		2. REPORT DATE August 1998	3. REPORT TYPE AND DATES COVERED Final Technical Report 1 Apr 93 to 30 Jun 98	
4. TITLE AND SUBTITLE Advanced Instrumentation and Measurement for Early Nondestructive Evaluation of Damage and defects in Aerostructures and Aging Aircraft			5. FUNDING NUMBERS F49620-93-1-0257	
6. AUTHOR(S) Jan d. Achenbach Isaac M. Daniel Sridhar Krishnaswamy				
7. PERFORMING ORGANIZATION NAME(S) AND ADDRESS(ES) Northwestern University 2137 N. Sheridan Road Evanston, IL 60208-3020			8. PERFORMING ORGANIZATION REPORT NUMBER	
9. SPONSORING/MONITORING AGENCY NAME(S) AND ADDRESS(ES) AFOSR/NA 801 N. Randolph Street Rm 732 Arlington, VA 22203-1977			10. SPONSORING/MONITORING AGENCY REPORT NUMBER	
11. SUPPLEMENTARY NOTES				
12a. DISTRIBUTION AVAILABILITY STATEMENT Approved for public release; distribution unlimited.			12b. DISTRIBUTION CODE	
13. ABSTRACT (Maximum 200 words) This report details the KU part of an AFOSR sponsored Vanderbilt/Northwestern University Research Initiative (URI) project. The project was divided into several tasks. New laser based ultrasonic techniques were developed including a Sagnac interferometer. This interferometer is a common-path device that is robust enough to be operated in the field. An adaptive heterodyne interferometer using photorefractive recording media was also developed for detecting ultrasound on rough surfaces. In another task, self-focussing ultrasonic arrays were devised capable of automatically focussing on surface breaking and interior flaws. Measurement models for characterizing this device were validated through direct interferometric measurements. Also, a full-field dynamic holographic interferometer was developed for disbond detection with high spatial resolution. This device allows for real-time automatic frequency scanning of an adhesively-bonded composite structure in order to make visible any underlying disbanded regions. In addition, this report describes the application and results of nondestructive evaluation (NDE) and other methods to the detection and characterization of the integrity of composite materials and the evaluation of the effectiveness and reliability of composite repairs for aging aircraft. Real-time NDE methods were developed and applied to composite laminates under monotonic loading to failure. Results from ultrasonic, acoustic emission (AE) and matrix cracking measurements were correlated with the macroscopic response of the material and its degradation. The effectiveness of composite patches in controlling damage propagation in a cracked aluminum substrate under fatigue conditions was also investigated by means of ultrasonic and acousto-ultrasonic methods.				
14. SUBJECT TERMS			15. NUMBER OF PAGES 77	
			16. PRICE CODE	
17. SECURITY CLASSIFICATION OF REPORT Unclassified	18. SECURITY CLASSIFICATION OF THIS PAGE Unclassified	19. SECURITY CLASSIFICATION OF ABSTRACT Unclassified	20. LIMITATION OF ABSTRACT UL	

**Advanced Instrumentation and Measurements for Early
Nondestructive Evaluation of Damage and Defects in
Aerostructures and Aging Aircraft**

AFOSR: F49620-93-1-0257

**Air Force University Research Initiative in Materials Degradation
and Fatigue in Aerospace Structures**

**Final Project Report
August 1998**

Submitted by

Jan D. Achenbach
Isaac M. Daniel
Sridhar Krishnaswamy

Northwestern University
2137 N. Sheridan Road
Evanston, IL 60208-3020.

19981113 035

TABLE OF CONTENTS

Introduction	iii
Task 1. NDE Instrumentation Development	
Task 1.2.1 Laser-based Ultrasonics for Flaw Detection	1.2.1/1-
1.2.2 Dynamic Holography	1.2.2/1-16
Task 2. NDE Theory and Techniques	
Task 2.2.5 Measurement Models for Ultrasonics	2.2.5/1-5
Task 2.3 Time Reversal Techniques for Ultrasonic NDE.....	2.3/1-9
Task 4. Damage Detection in Composite Materials (Northwestern).....	4/1-5

INTRODUCTION

This AFOSR sponsored Vanderbilt/Northwestern University Research Initiative (URI) project was directed towards the development of advanced instrumentation and measurement techniques suitable for detection and analysis of cracking and corrosion in aging aircraft. The project was divided into several tasks which range from the development of NDE instrumentation, theoretical measurement models and experimental techniques to more basic studies of the initiation and development of fatigue cracks and the magnetic measurement of the electrical currents that are generated in aluminum structures. The measurement techniques developed include: SQUID magnetometry; laser interferometry, ultrasonics, and advanced image processing methods.

This final project report pertains only to the Northwestern University part of this multi-university project. Vanderbilt University will submit its report separately to the AFOSR. The tasks performed at Northwestern University are:

Task	Title	Investigator
1.2.1	Laser-Based Ultrasonics for flaw detection	J. D. Achenbach
1.2.2	Dynamic holographic interferometry	S. Krishnaswamy
2.2.5	Measurement models for ultrasonics	J. D. Achenbach
2.	Self focusing techniques for ultrasonic NDE (JDA)	J. D. Achenbach
4.	Damage detection in composite materials	I. M. Daniel

The objectives and accomplishments in each of these tasks is described in detail in the following sections.

TASK 1. NDE INSTRUMENTATION DEVELOPMENT (Northwestern)

1.2 NDE Instrumentation

The objective of Task 1.2 is to develop advanced ultrasonic and optical instrumentation for NDE.

1.2.1 Laser-Based Ultrasonics for Flaw Detection

1. Objectives:

To exploit the advantages of laser-based ultrasonics (LBU) -- point generation and point detection, non-contact, remote placement of equipment by using fiber optics, easy scanning, curved surfaces -- for NDE of structures. The LBU technique uses a laser to excite ultrasound and a single- or dual-probe laser interferometer for the measurement of ultrasonic signals.

2. Accomplishments/New Findings:

A portable fiberized laser-based ultrasonics system for non-contact generation and detection of ultrasonic waves is being developed. The system consists of two main parts: the generation unit and the detection unit. The generation unit employs a portable, cavity-folded Q-switched Nd:YAG laser as the ultrasound generation source. The Nd:YAG laser can deliver an infrared beam (1064 nm wavelength) with pulse energy up to 200 mJ at 10 ns pulse duration. The output beam is coupled to a high-power fiber for ultrasound generation at a remote location and at areas with limited access.

The laser-based ultrasound detection unit is based on a fiberized Sagnac interferometer. This interferometer is truly path-matched, and therefore is insensitive to low frequency thermal fluctuations and vibratory noise.

In recent work a new laser based technique -- the Scanning Laser Source (SLS) technique -- for the detection of small surface-breaking cracks on rough and curved surfaces has been developed. This technique allows detection of flaws by monitoring the variations of ultrasonic amplitude and frequency (flaw signature) as the laser ultrasonic source is scanned across the object and passes over any defects. Typical flaw signatures for different kinds of surface breaking defects have been obtained.

Conventional ultrasonic flaw detection methodologies require the generation of an ultrasonic wave packet that travels through a structure, and the subsequent detection of reflections of this wave packet from any existing flaws within the structure. Laser-based ultrasonics has thus far followed the same methodology except that the generation and detection of the ultrasonic wave packets were done using lasers. The limitations on the size of flaws that can be detected using this approach are set by the ultrasonic reflectivity of the flaws for the particular wavelength used, and by the sensitivity of the particular ultrasonic detector used. In view of their expected small reflectivity, the reflected wave packets from very small flaws are often too weak to be detected with existing laser detectors, which typically have significantly lower sensitivity than conventional piezo-electric transducers (PZT).

As part of this project an alternate approach for ultrasonic detection of surface-breaking small cracks using laser-based techniques has been developed. In this approach, the ultrasound generation source, which is a point or line-focused high-power laser beam, is swept across the test specimen surface and passes over any existing surface-breaking flaws (Figure 1).

The generated surface ultrasonic wave packet is detected at a fixed location on the test specimen. It is found that the amplitude and frequency of the measured ultrasonic signal have specific variations

The generated surface ultrasonic wave packet is detected at a fixed location on the test specimen. It is found that the amplitude and frequency of the measured ultrasonic signal have specific variations

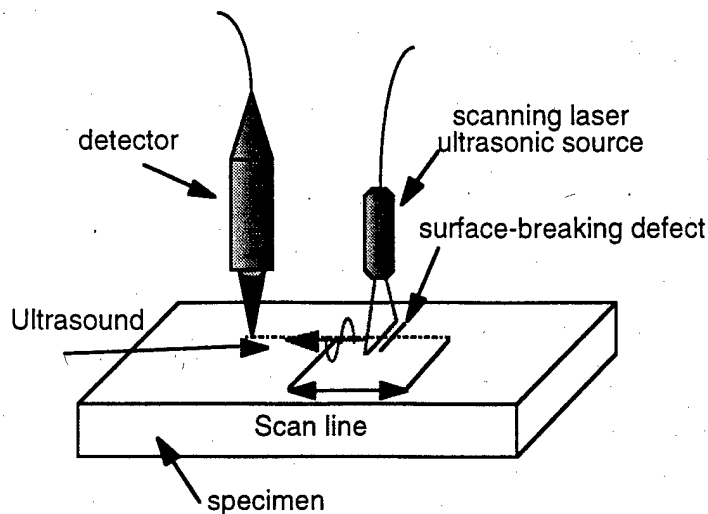


Figure 1. Principle of the Scanning Laser Source method with laser detection.

when the laser source approaches and passes over the defect. Proof of concept experiments have been carried out for flat specimens with EDM notches of various sizes, and an actual engine disk, all of which were provided by Allied Signal Engines.

A typical characteristic signature for a surface-breaking notch of 0.2 mm depth on a flat specimen is shown in Figure 2. The following aspects of this signature should be noted:

(1) When the source is far ahead of the defect, the generated ultrasonic *direct* signal is of sufficient amplitude above the noise floor to be unambiguously picked up by the laser detector (Figure 3a). Also, a weak reflection from the flaw is barely visible amidst the noise.

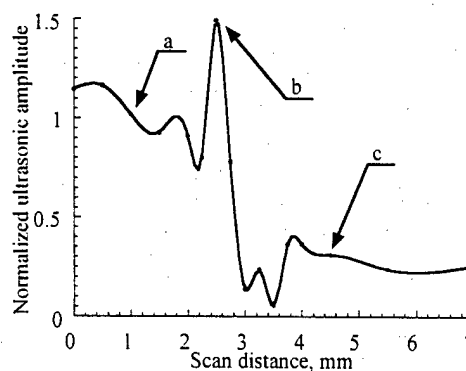


Figure 2. Typical characteristic signature of ultrasonic amplitude vs. SLS location as the source is scanned over a defect: (a) far ahead, (b) close to, and (c) behind the defect.

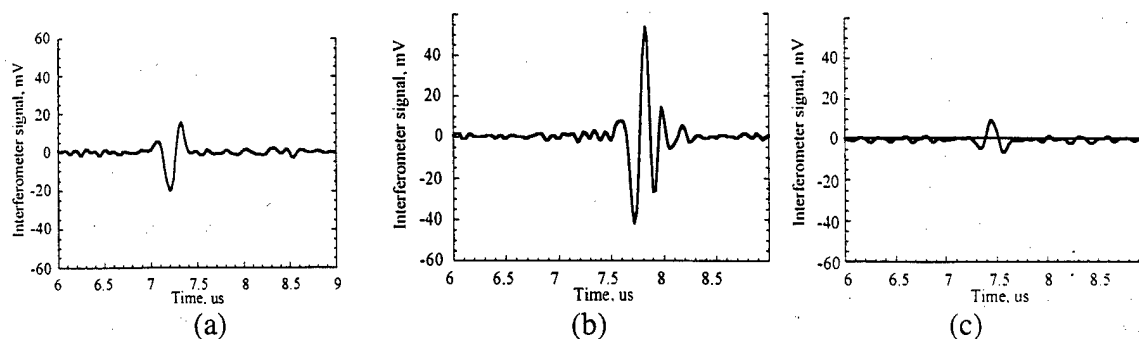


Figure 3. Representative ultrasonic signals detected by the Sagnac interferometer at a fixed location when the laser source is:
(a) far ahead, (b) close to, and (c) behind the defect.

(2) As the source approaches the defect, the amplitude of the direct signal significantly increases (Figure 3b). This increase (from a level that was already sufficiently above the noise floor) is more readily detectable with a laser interferometer than any weak echoes from the flaw. We attribute this increase in signal amplitude not only to possible interference of the incident wave with the wave reflected by the defect (as the source is very close to the defect), but possibly more importantly to the changes in the conditions of generation when the laser source is in the vicinity of the defect.

(3) As the source passes over the defect, the ultrasonic signal amplitude drops noticeably again presumably due to changes in the conditions of generation when the source is right above the defect. Subsequently, as the source moves behind the defect, the amplitude increases again to some level that is compatible with the transitivity of the flaw (Figure 3c). Note that when the flaw depth is smaller than the wavelength of the generated ultrasound, a significant portion of the sound can pass by the flaw when the source is behind it.

These data were obtained for an aluminum specimen with an EDM notch (length 4 mm, width 0.3 mm, and depth 0.2 mm). The Scanning Laser Source used in this experiment had the following parameters: line length 4 mm, width 0.3 mm, thermoelastic generation at 4 mJ per pulse. A narrow-band Sagnac interferometer was used as the ultrasonic detector.

All the advantages of laser based ultrasonics including non-contact and curved surface inspection apply to the SLS approach as well. Of particular importance are:

(a) Ease of Scanning: The proposed method for detecting small surface-breaking flaws requires the scanning of a very narrow ultrasonic source over a surface and over any existing flaws. Conventional ultrasonic sources such as pzt-transducers, EMATs and capacitive transducers are not small enough or do not lend themselves to easy scanning. Only laser ultrasound generation sources are small enough for this method, and being non-contact, they can be easily scanned across a test surface of complex geometry.

(b) Coupling Independence: The detection of the generated ultrasound is done at a fixed location and can be monitored using either a laser interferometer or a conventional pzt-transducer. The laser interferometer provides non-contact absolute measurements, and a pzt-detector provides higher sensitivity, and therefore this choice must be determined by the application. In either case, since the detection is at a fixed location, variabilities associated with pzt-coupling or laser speckles (for interferometric detection) are eliminated.

(c) Signal-to-noise improvement: The SLS approach provides enhanced signal-to-noise performance compared to conventional pitch-catch mode of operation. This is because the presence of a flaw is indicated by an *increase* in the amplitude of the detected ultrasonic signal rather than by the presence of a weak echo.

Publications from this Task:

1. Y. Nagate, J. Huang, J. D. Achenbach and Sridhar Krishnaswamy, "Computed Tomography System Using Laser-Based Ultrasonics," Review of Progress in Quantitative Nondestructive Evaluation, ed. D. O. Thompson and D. E. Chimenti, Plenum Press, New York, Vol. 15, pp. 861-868, 1996.
2. Y. Nagate, J. Huang, Sridhar Krishnaswamy and J. D. Achenbach, "Laser-Based Ultrasonics for Flaw Detection," Proceedings of the IEEE 1994 Ultrasonics Symposium, pp. 1205-1209, 1995.
3. Pavel Fomitchov, Liusheng Wang, J. Scott Steckenrider, Sridhar Krishnaswamy and J. D. Achenbach, "Laser-Based Ultrasonics of QNDE Applications," Proc. International Conference in Experimental Mechanics: Advances and Applications, F. S. Chau and C. T. Liu, Eds., Vol. 2921, SPIE Proceedings Series, pp. 166-176, 1997.
4. Pavel A. Fomitchov, Sridhar Krishnaswamy and J. D. Achenbach, "Compact Phase-Shifted Sagnac Interferometer for Ultrasound Detection," Optics and Laser Technology, 29, p. 333, 1997.
5. Pavel Fomitchov, S. Krishnaswamy and J. D. Achenbach, "A Prototype Fieldable Sagnac Interferometer for Ultrasound Detection on Rough Surfaces," Proc. Eighth International Symposium on Nondestructive Characterization of Materials, to appear.
6. Pavel A. Fomitchov, Alexei Kromine, Liusheng Wang, Sridhar Krishnaswamy and Jan D. Achenbach, "A Portable Laser-Based Ultrasonics System for the Inspection of Aging Aircraft Structures," Proceedings First Joint DoD/FAA/NASA Conference on Aging Aircraft, 1997.
7. Pavel Fomitchov, Alexei Kromine, Sridhar Krishnaswamy and Jan D. Achenbach, "Laser-Based Ultrasonics for Crack Detection," Proceedings Second Joint NASA/FAA/DoD Conference on Aging Aircraft, 1998.

TASK 1.2.2 DYNAMIC HOLOGRAPHIC INTERFEROMETRIC NDE SYSTEMS

1. OBJECTIVE

The objective of Task 1.2.2 was to develop optical NDE techniques based on dynamic (adaptive) holography using photorefractive crystals to provide high resolution and good signal contrast for better signal identification.

2. ACCOMPLISHMENTS

Two classes of dynamic holographic interferometric NDE systems have been devised:

1. Full-field systems for large area disbond detection in adhesively-bonded structures have been configured. These systems provide quantitative information over a large area about low frequency (kHz) and large amplitude (μm) object deformation.
2. An adaptive heterodyne interferometer has been developed for point measurement of high frequency (MHz) and low amplitude (0.1nm) ultrasonic signals.

These systems are useful in laser ultrasonic NDE for detection of cracks and other local defects.

3. TECHNICAL DETAILS:

In the following subsections, each of the above systems is explained in detail. Results of applications are presented.

3.1 Full-field dynamic holographic NDE system for detection of disbonds in adhesively-bonded structures

3.1.1 INTRODUCTION

Photorefractive crystals (PRCs) are becoming increasingly useful in holographic interferometry. PRCs appear to be a good alternative to electronic speckle pattern interferometry (ESPI) and classical holography using photographic emulsions or thermoplastic recording materials. Using PRCs for dynamic holographic interferometry (DHI) leads to better image quality than those associated with ESPI but unlike with the use of other holographic recording materials, PRCs do not require chemical or physical processing and therefore real-time visualization of the hologram is possible.

In photorefractive crystals under non-uniform illumination, electrons/holes that are trapped in impurities can be photo-excited into the conduction band. These electrons/holes migrate toward areas of dark illumination, where they get trapped again. A non-uniform space-charge field is then created, leading to spatial modulation of the refractive index via the electro-optic effect. Thus, PRCs can be used to store phase holograms. Since the first observation of the photorefractive effect in LiNbO_3 ^{3.1.1,2}, many photorefractive materials with different physical properties have been investigated. In order for PRCs to be widely use as dynamic holographic recording material, PRCs must be able to perform fast recording with moderate laser power and still allow for holographic interferometry with good fringe contrast. The serious difficulty that arises when one uses PRCs for holographic interferometry of diffusely reflecting object is the limited amount of object light that can be collected into the crystal. The sillenite family ($\text{Bi}_{12}\text{SiO}_{20}$, $\text{Bi}_{12}\text{TiO}_{20}$, $\text{Bi}_{12}\text{GeO}_{20}$) exhibits the highest sensitivity among presently known PRCs. Using the high-sensitivity of BSO associated with its efficient polarization separation of the recorded and reconstructed waves when using the anisotropic self-diffraction effect, high quality of dynamic holographic interferograms can be obtained^{3.1.3,4}.

Here we show that BSO crystals can be used in a quasi-real-time interferometer. In a first part, we demonstrate phase shifting interferometry of vibrating diffusely scattering opaque specimens. For this, a sequence of at least three double pulse interferogram are recorded with different phase shifts of the reference beam. Because of the high quality of the interferometric image, no post digital processing, such as low-pass filtering, is needed before phase unwrapping. In a second experiment, the phase map of a phase object under transient load is obtained through quasi-heterodyne holographic interferometry^{3.1.5}. In this case, two holograms corresponding to a deformed and the undeformed state are recorded with two separate reference beams. The read-out of the hologram is then done simultaneously with both reference beams. By introducing phase shifts between the two reference beams during the read-out, the phase maps can be obtained.

3.1.2 WAVE MIXING IN BSO CRYSTAL

For two-wave mixing in the cubic crystals, it has been found^{3.1.6} that the optimal crystal orientation is when the optical surfaces of the crystal are parallel to the (110) crystallographic planes and when the grating vector and applied external electric field are parallel to the $[1\bar{1}0]$ direction (see Fig. 3.1.1). If the incident reference W_R and the signal beams W_O have their polarization along the [001] axis, then the diffracted object W_{DO} and diffracted reference W_{DR} beams have their polarization plane rotated by 90° with respect to the transmitted object W_{TO} and transmitted reference W_{TR} beams^{3.1.2}. The signal of interest is contained in the diffracted reference beam W_{DR} which is typically collected in a camera, and all other light that is collected by the camera is essentially noise that degrades the signal. To obtain a holographic interferogram with a good signal-to-noise ratio (SNR), the intensity of the signal needs to be as high as possible, and the intensity of all other light which contribute to the noise must be as small as possible. The major optical noise collected by the camera come from: (i) the transmitted object beam, (ii) the simple scatter of the reference beam due to imperfections in the crystal, and (iii) the diffracted beam that arises from a secondary grating (noise grating) created by the input beams and the scatter noise. Due to the very low diffraction efficiency of the secondary noise grating, the magnitude of this component of the noise is very small compared to that of the signal. Since the first two of the above noise beams have their polarizations 90° rotated with respect to the diffracted reference W_{DR} which contains the signal of interest, they can therefore be minimized by the use of a polarizer that will pass essentially only the signal W_{DR} . By taking advantage of the polarization rotation for the diffracted signal, it is thus possible to have a continuous read-out with a SNR sufficient for most application (SNR up to 100). The noise is mostly due to the transmitted object beam that is not completely turned off by the pair of polarizers. If better SNR is needed, the object illumination can be turned off during the read-out (SNR up to 1000)^{3.1.4}.

The diffraction efficiency is defined as the ratio of the intensity of the diffracted reference beam (the signal) to the amount of incident reference: $\eta = I_{DR}/I_R$. It is a parameter that has a major bearing on the quality of the dynamic holographic interferometer. For small refractive index modulations, η is proportional to the square of the induced electric field inside the photorefractive crystal and we can assume the induced electric field follows an exponential buildup^{3.1.8}:

$$\eta(t) = \eta_{\text{sat}}(1 - \text{Exp}[-t/\tau])^2 \quad (3.1.1)$$

with τ being the time constant, and η_{sat} the value at saturation. In the case of the diffusion mechanism of charge transport (no applied external electric field), the diffraction efficiency of the BSO crystal is limited to small values. For example, using a $10 \times 10 \times 2 \text{ mm}^3$ BSO crystal, the maximum diffraction efficiency was measured to be 0.2%, corresponding to a writing-beam angle of 55° . Furthermore, the relatively large writing-beam angles required in this mode result in a rather slow time response of the crystal. The diffraction efficiency of the holographic grating can be greatly enhanced by applying an external electric field onto the crystal and by reducing the writing-beam angle⁴. An ac-rather than a dc-electric field is preferred since it leads to many advantages including increased stability, no requirement for uniform illumination of the crystal, and the avoidance of the electrode shadowing problem^{3,1,9}. Applying an external electric field not only increases η_{sat} but it also increases the time constant τ , and can be used to slow down the erasure of the hologram during the read-out.

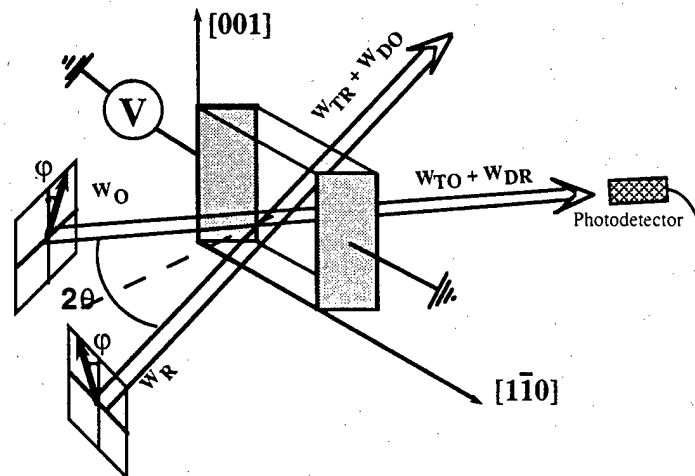


Fig. 3.1.1: Principle of the holographic interferometer using two-wave mixing in BSO crystal.

3.1.3 PHASE SHIFTING DOUBLE-EXPOSURE HOLOGRAPHIC INTERFEROMETRY

In double-exposure holographic interferometry, a hologram of the object in an arbitrary state at an instant of time is first recorded in the crystal. A second hologram of the object in another state at another instant of time is then recorded on top of the first one. Retrieval of the information is achieved by blocking the object beam and reading the double-exposure hologram with the reference beam.

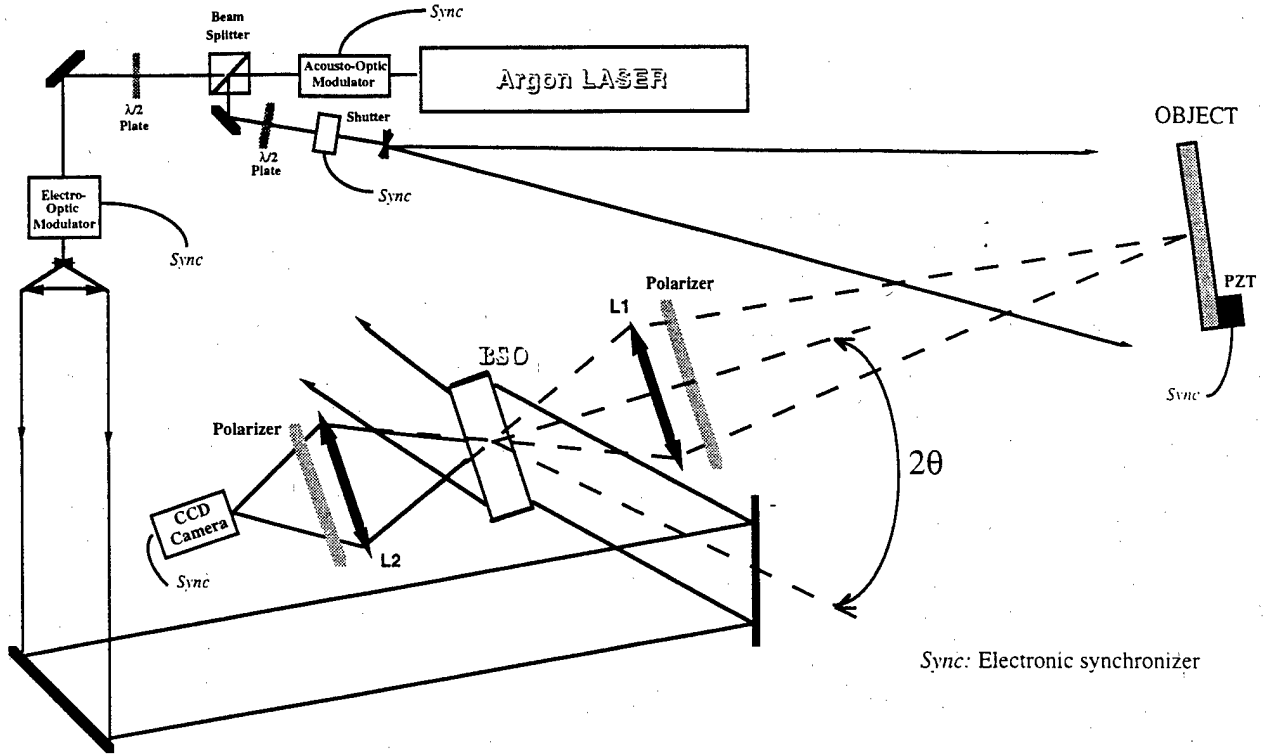


Fig. 3.1.2: Dynamic holographic interferometer setup.

The experimental setup used to study the vibration modes of continuously vibrating specimens is shown Fig. 3.1.2. An acousto-optic modulator is used to pulse the light from an Argon laser according to the extrema of the acoustic vibrational displacement, allowing continuous recording of a double-pulse hologram. In this way, the intensity recorded on the camera upon readout of the hologram exhibits fringes with a cosine dependence on the deformation. In our experiment a duty cycle of 22% is able to give reasonable cosine fringes, while still providing enough intensity. A sequence of three interferograms is obtained. An optical phase shift is introduced by means of the electro-optic modulator in the reference beam during the recording process between the time of the maximum and minimum acoustic deformation. The first hologram of the sequence has no phase shift between the maximum and minimum deformation:

$$I_1 = \beta I_0 (1 + \cos 2M) \quad (3.1.2)$$

In the second hologram of the sequence a phase shift of $-\pi/2$ and $+\pi/2$ is introduced at the minimum and maximum deformation, respectively, such that the fringe function obtained is:

$$I_2 = \beta I_0 (1 - \cos 2M) \quad (3.1.3)$$

In the third hologram, a phase shift of 0 and $+\pi/2$ is introduced at the minimum and maximum deformation, respectively, such that the fringe function obtained is:

$$I_3 = \beta I_0 (1 + \sin 2M) \quad (3.1.4)$$

The deformation signal of interest M can then be extracted via:

$$\tan 2M = \frac{2I_3 - [I_1 + I_2]}{I_2 - I_1} \quad (3.1.5)$$

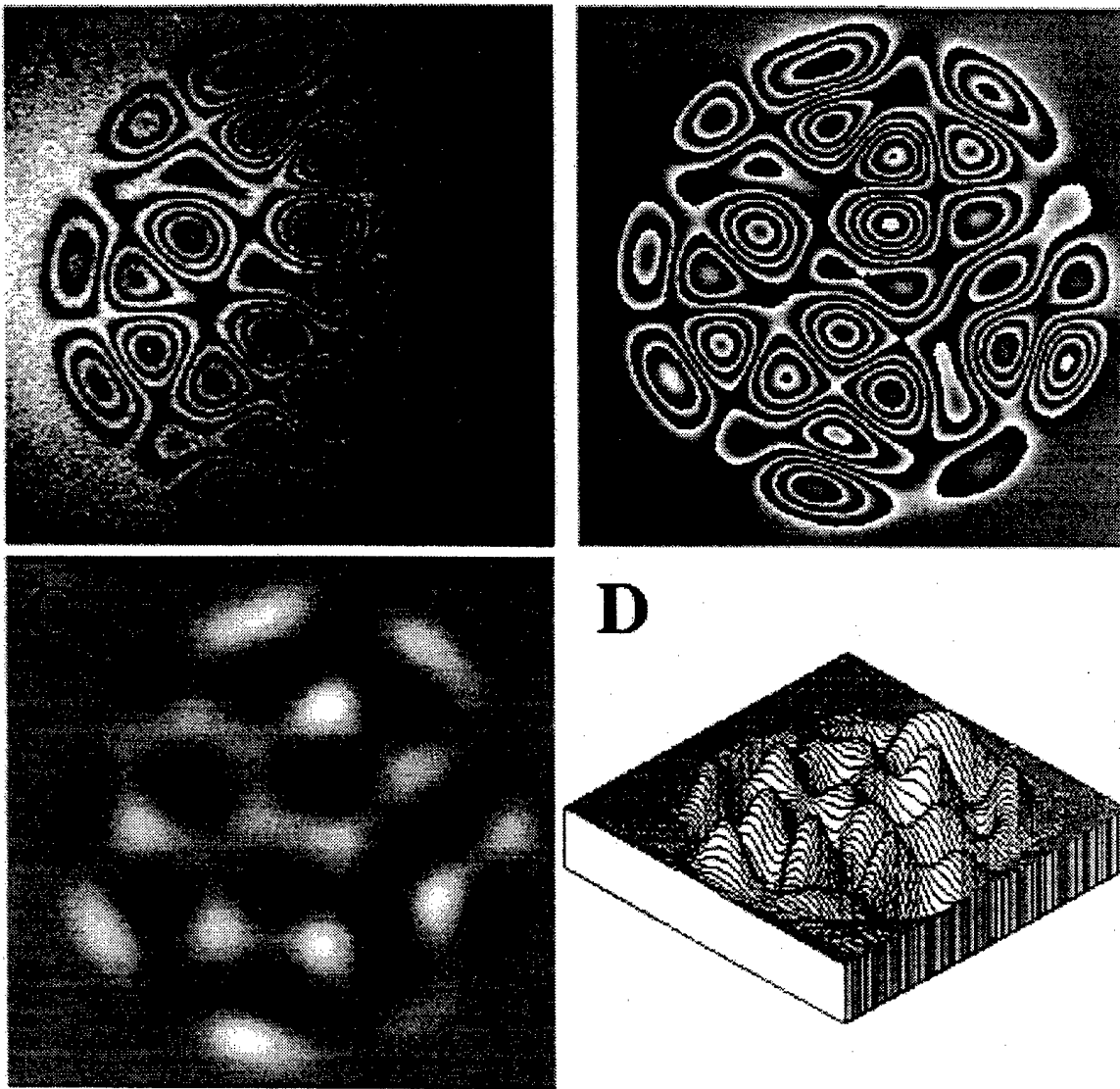


Fig. 3.1.3: Visualization using DHI of a clamped circular plate vibrating at 69 kHz. A) Holographic interferogram with no phase shift, B) wrapped phase map, C) unwrapped phase map, D) 3D view of the unwrapped phase map.

The 2π phase jumps in the phase map can be removed by a phase unwrapping procedure. Using such a procedure, we can see that an undetermination arises if locally the information term goes down to zero, corresponding to a dead pixel. Before using the phase unwrapping procedure one must first ensure that there are no dead pixels. This is usually done using low-pass filtering of the image. The number of pixels which are invalid due to speckle noise for phase calculation can thus be greatly decreased and ensures that the phase extraction procedure works satisfactorily. The main drawback of using a low-pass filtering procedure is its limitation of the fringe resolution. With DHI a large aperture imaging system can be used, leading to a speckle size much smaller than the pixel size of the ccd camera and thus leading to only few (if any) dead pixels, and so low-pass filtering is usually not needed. This is clearly a great advantage of using DHI compared to ESPI. In the case of ESPI it is not possible to record interferograms without dead pixels and low-pass filtering is mandatory. An example of phase unwrapping of DHI images is shown in fig. 3.1.3. It corresponds to a complex vibration mode of a circular membrane excited at 69 kHz. Sharp and dense fringes are resolved and no low-pass filtering was needed before the phase extraction procedure was applied. The separate lobes of vibration are clearly visible.

3.1.4 QUASI-HETERODYNE INTERFEROMETRY OF NON-RECURRING EVENTS

For the study of transient non-recurring events, the previous scheme cannot be used. In this case only one double exposure hologram can be recorded and a quasi-heterodyne technique is used to extract the phase information⁵. For quasi-heterodyne interferometry, independent access to the two recorded wavefronts is necessary in order to subsequently control their relative phase. This implies independent recording of each wavefront by using different reference beams. The optical arrangements for two-reference-beam holographic interferometry of a phase object is sketched in 3.1.4. The first object state O_1 is recorded by reference R_1 and the second object state O_2 by reference R_2 in the same crystal. During the read-out of the hologram, the interferogram is analyzed at least three times, and the relative phase between R_1 and R_2 is changed each time using a piezo-electric mirror. The local intensities I_k are then given by:

$$I_k(x) = a(x)(1 + m(x)\cos[M(x) + \phi_k]) \quad (3.1.6)$$

which correspond for $k=1,2,3$ to a system of three equations with three unknown values: the mean intensity $a(x)$, the fringe contrast $m(x)$, and the phase term $M(x)$. By using $\phi_k=0, \pi$, and $\pi/2$, the set of equations is similar to Eq. 3.1.2,3, and 4, and we can use Eq.3.1.5 to calculate the phase term M . In this case, because the object beam is specular, there is no problem associated with dead

pixels as with the case of speckle object beam. Fig. 3.1.5 shows an example result of the stress state near a crack in a PMMA plate with a pre-cut crack.

The specimen was placed in a load frame for testing in a three-point bend configuration. The acousto-optic modulator is used to pulse the laser beam at two load levels. An increasing load is applied to the specimen, and a double-pulse hologram is recorded when the load differential generates a sufficient number of fringes. The PRC being a dynamic recording material, the first recorded hologram will start to be erased during the recording of the second hologram. In order to obtain a fringe contrast $m(x)$ as close as possible to unity, the intensity and width of the second pulse is adjusted such that the exponential erasure of the first hologram and the exponential increase of the second hologram lead to two holograms with the same net diffraction efficiency. We must also take into account the time decay of the diffraction efficiency during the read-out process. In this case, $a(x)$ will not be the same for the three phase shifted images. Fortunately, by using low intensity reference beams for the read-out, and if necessary by applying an external electric field to slow down the decay, the mean intensity $a(x)$ can be assumed to be constant for the read-out of the three phase shifted images. It is thus possible to use such a system to study the phase maps generated by non-recurring events.

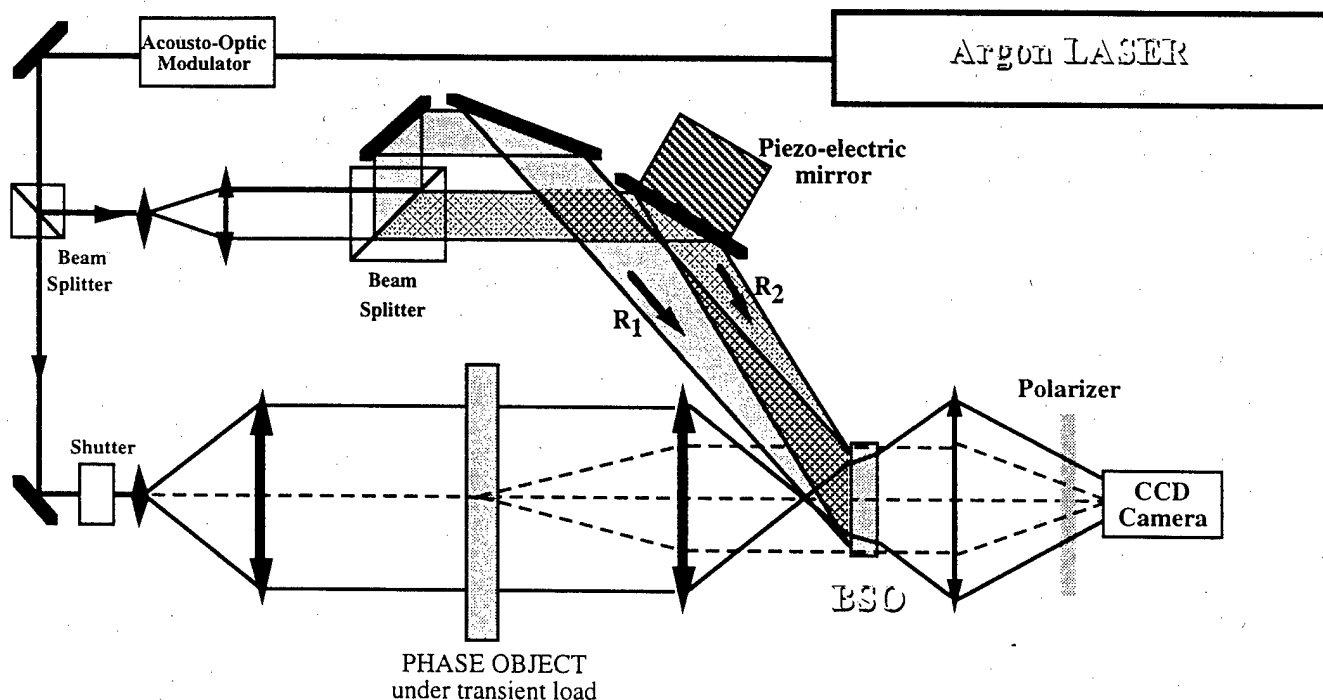


Fig. 3.1.4: Two-reference-beam dynamic holographic interferometer setup.

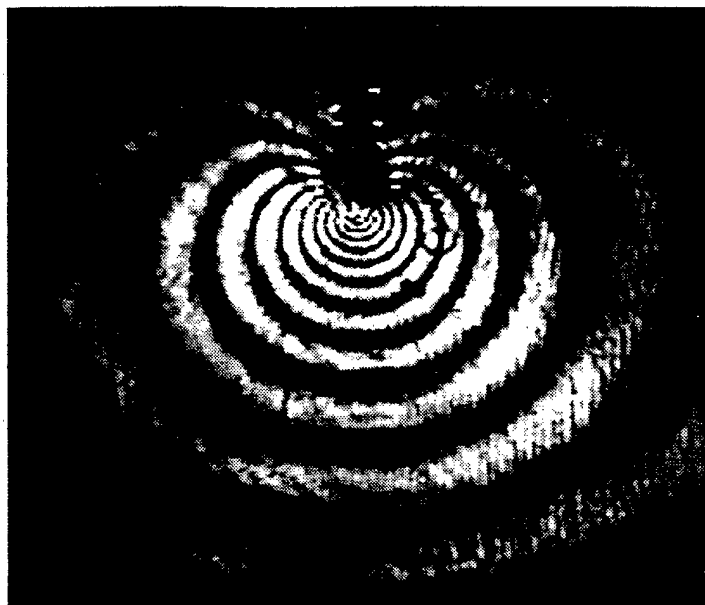


Fig. 3.1.5: Three-point bend of PMMA plate with pre-cut crack.

3.1.5 REFERENCES

- [3.1.1] A. Ashkin, G. D boyd, J. M. Dziedzic, R. G. Smith, A. A. Ballman, J. j. Levinstein, and K. Nassau, "Optically induced refractive index inhomogeneities in LiNbO₃ and LiTaO₃," Appl. Phys. Lett. **9**, 72 (1966).
- [3.1.2] M. P. Petrov, S. V. Miridonov, S. I. Stepanov, and V. V. Kulikov, "Light diffraction and nonlinear image processing in electro-optic BSO," Opt. Commun. **31**, 1, 301-304 (1979).
- [3.1.3] R. C. Troth and J. C. Dainty, "Holographic interferometry using anisotropic self-diffraction in BSO," Optics Lett. **16**, 1, 53-55 (1991).
- [3.1.4] B. Pouet and S. Krishnaswamy, "Dynamic holographic interferometry by photorefractive crystals for quantitative deformation measurements," Appl. Optics. **35**, 5, 787-794 (1996).
- [3.1.5] R. Dändliker and R. Thalmann, "Heterodyne and quasi-heterodyne holographic interferometry," Opt. Eng. **24**, 5, 824 - 831 (1985).
- [3.1.6] A. Marrakchi, J. P. Huignard, and P. Günter, "Diffraction efficiency and energy transfer in two-wave mixing experiment with BSO crystals," Appl. Phys. **24**, 131-138 (1981).
- [3.1.7] A. Marrakchi, R. V. Johnson, and A. R. Tangay, "Polarization properties of enhanced self-diffraction in selenite crystals," IEEE J. Quant. Elec. **QE-23**, 12, 2142-2151 (1987).
- [3.1.8] Pochi Yeh, "Introduction to photorefractive nonlinear optics," Wiley series in pure and applied optics (1993).
- [3.1.9] K. Walsh, A. K. Powell, C. Stace, and T. J. Hall, "Techniques for the enhancement of space-charge fields in photorefractive materials," J. Opt. Soc. Am. B **7**, 3, 288-303 (1990).

3.2 Adaptive heterodyne interferometer for non-contact ultrasound detection on rough surfaces:

3.2.1 INTRODUCTION:

For laser ultrasonics to be widely used in nondestructive evaluation (NDE) applications, the techniques must be able to perform equally well on different specimens independent of their surface quality. Laser generation of ultrasound is well known. Remote generation using optical fibers and various configurations used to improve ultrasound generation have been demonstrated. For the detection of ultrasound, various interferometers have been described in the literature^{3.2.1}. Only some of these are well adapted to the experimental conditions generally encountered in NDE. Primarily, the interferometer must be able to achieve good sensitivity on rough surfaces in an environment with large amplitude low frequency noise present. In addition, the interferometer should have a broadband detection. For convenience of use, the interferometer must also be able to operate with multimode optical fibers for remote detection.

Wave mixing in photorefractive crystals (PRCs) is an attractive way of realizing some of these requirements. Two-wave mixing in PRCs is used to create a diffracted beam that acts as a reference beam. The wavefront of the diffracted beam matches exactly that of the signal beam^{3.2.2}. The dynamic nature of the wave-mixing process enables the reference beam to adapt to changes in the signal beam wavefront. The ability of the system to work in a noisy environment depends on the dynamic characteristics of the mixing process and is mainly controlled by the nature of the photorefractive material, the total optical power density in the PRCs and other experimental parameters such as grating pitch and applied external electric field. To date, the rather long time response of the photorefractive effect has been the major limitation that has prevented wide use of these systems in industrial applications.

Here, we present an optimized heterodyne interferometer using photorefractive cubic crystal $\text{Bi}_{12}\text{SiO}_{20}$ (BSO). The interferometer demonstrates large étendue, absolute calibration and good noise protection. Two photorefractive crystals: BSO and BSO:Cr, which have different photorefractive characteristics are compared. The use of an external ac electric field applied to the PRCs, typically used to improve the diffraction efficiency, is also investigated. Finally, several applications to NDE are demonstrated.

3.2.2 INTERFEROMETER DESIGN AND OPTIMIZATION

The setup schematic is shown in Fig. 3.2.1. The signal beam that is scattered by a rough object surface and a reference (writing) beam that is directly derived from the laser are made to interfere inside the PRC. For heterodyning, a third beam (the reading beam) is also derived from the laser. The reading beam is polarization rotated, frequency shifted by f_b using a Bragg cell, and

then realigned with the writing beam. The writing and reading beams are thus collinear with cross-polarizations and

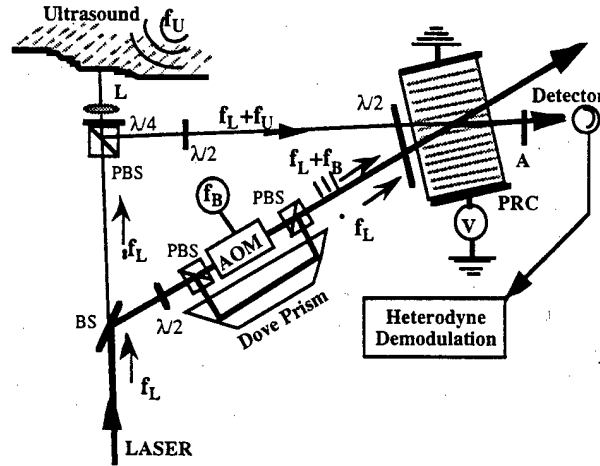


Figure 3.2.1: Schematic of the setup

two different frequencies, f_L and $f_L + f_B$, respectively. Only the grating due to the homodyne interference between the writing and the signal beams is created in the photorefractive crystal, as only this is stationary spatially. The grating vector is along the [001] crystal axis. Using this geometry, the diffracted beam has its polarization axis aligned with that of the transmitted beam. Following the standard theory of the photorefractive effect, the intensity detected after the analyzer can be written as^{3.2.3}:

$$\begin{aligned}
 I(t) = & |\gamma_{Ta}|^2 I_S + |\gamma_{Da}|^2 I_P + |\gamma_{D'a}|^2 I_{P'} \\
 & + 2|\gamma_{Ta}||\gamma_{Da}|\sqrt{I_P I_S} \cos(\varphi(t) + \phi_T - \phi_D) \\
 & + 2|\gamma_{Ta}||\gamma_{D'a}|\sqrt{I_P I_S} \cos(2\pi f_B + \varphi(t) + \phi_T - \phi_{D'}) \\
 & + 2|\gamma_{Da}||\gamma_{D'a}|\sqrt{I_P I_{P'}} \cos(2\pi f_B + \phi_D - \phi_{D'})
 \end{aligned}
 \tag{3.2.1}$$

Here I_S and I_P are respectively the intensities of the signal and writing pump beams, and $I_{P'}$ is the intensity of the read-out beam. γ_T and γ_D are the amplitude of the transmission coefficient for the signal beam and the diffraction coefficient for the writing pump beam, respectively. $\gamma_{D'}$ is the amplitude of the diffraction coefficient for the read-out pump beam. The subscript 'a' indicates the projection along the direction of the analyzer; ϕ_T , ϕ_D , and $\phi_{D'}$ are the phase terms of γ_T , γ_D , and $\gamma_{D'}$, respectively. $\varphi(t)$ is the small phase shift induced by the ultrasonic signal.

From eq. 3.2.1 we can see that homodyne detection coexists with the heterodyne detection. By choosing f_b large enough, the homodyne detection can be separated from the heterodyne detection. The advantage of using the heterodyne detection is the possibility of automatic absolute calibration. For doing that the signals at frequency f_b and $f_b \pm f_u$ are compared. f_u is the frequency of the ultrasonic signal. We can see in eq.3.2.1 that the last term is also at the frequency of the carrier f_b and it will perturb the calibration. Thus, in order to optimize the heterodyne detection of $\phi(t)$ we must have: $|\gamma_{Da}|=0$. In this case, eq. 3.2.1 reduces to the classical equation of heterodyne detection using a Mach-Zehnder configuration.

In a first step, the polarization angles are adjusted using a half-wave plate (without the analyzer in the set up) in order to maximize the heterodyne component γ_D . Then the analyzer is introduced and its direction is adjusted to block the homodyne diffracted signal, $|\gamma_{Da}|=0$. Finally, by adjusting the polarization of the signal beam, we allow a component of the signal beam to be transmitted by the analyzer such that $|\gamma_{Ta}|^2 I_s = |\gamma_{Da}|^2 I_p$, corresponding to maximum modulation depth of the interference heterodyne signal.

3.2.3 SPATIAL FREQUENCY RESPONSE

For optimization of eq. 1, we assume that $|\gamma_{Da}|$ and $|\gamma_{Ta}|$ have the same spatial distribution. In the case of light reflected by a diffusing surface, or if a multimode fiber is used for collecting the object beam, the speckled object beam entering the PRC is composed of various angular components. In order to satisfy the requirement that $|\gamma_{Ta}|^2 I_s = |\gamma_{Da}|^2 I_p$ for all the angular components, the PRC must have a uniform response at all spatial frequencies.

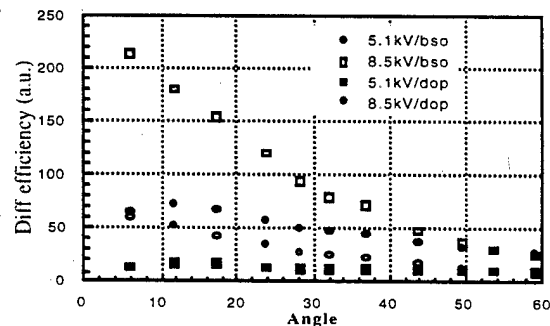


Fig. 3.2.2: Diffraction efficiency:BSO and BSO:CR marked bso/dop

However, the photorefractive effect is strongly dependent on the grating pitch (and hence to the angular components) in the PRC. We show in fig. 3.2.2, the comparison between an undoped BSO crystal and BSO:Cr. The BSO:Cr was grown at the A. F. Ioffe Physical-Technical Institute

of Russian Academy of Science^{3,2,4}. It is well known that when an external electric field is applied to a BSO crystal, the diffraction efficiency is improved. The resonant behavior of the diffraction efficiency in the presence of an electric field is clearly seen on fig. 3.2.2.

As expected, the presence of chromium decreases the diffusion length of the photo-excited carrier, resulting in a displacement and broadening of the maximum of the diffraction efficiency^{3,2,4}. With an applied field of 8.5kV/cm, at half value for the diffracted intensity, we measure an aperture angle of 45° for BSO:Cr and 26° for BSO. A larger aperture angle corresponding to a larger étendue allows collecting more of the light scattered by the object and leads to a higher contrast of the signal detected by the photodetector. Unfortunately, the introduction of chromium also increases the absorption. At $\lambda=514\text{nm}$, the BSO:Cr crystal was measured to have an absorption coefficient 2.5 times higher than the undoped BSO. Furthermore, the time response of the BSO:Cr was also slower than that of the undoped BSO; up to 2 times slower for a writing beam angle of 50°. The higher spatial frequency bandwidth of BSO:Cr is thus obtained at the expense of higher absorption and slower time response. For our applications, where the intensity onto the photodetector must be maximized to ensure shot noise-limited measurements and where protection to vibration noise is a concern, the undoped BSO was preferred.

3.2.4 INFLUENCE OF AN ELECTRIC FIELD

As mentioned above, an external electric field is applied in order to increase the diffraction efficiency. Unfortunately, applying an electric field induces linear birefringence and slows down the time response of the crystal. Optimization of the time response is achieved by reducing the angle between the object beam and the read/write beams. The smaller interaction angle corresponds to faster time response and at the same time leads to higher diffraction efficiency as shown in fig. 3.2.2. In our application, the slightly slower time response due to the applied electric field is largely compensated by the large increase in diffraction efficiency.

The simultaneous presence of linear birefringence and optical activity leads to elliptical polarization. In this case, a small component of the diffracted beam at frequency f_L is transmitted through the analyzer. The ellipticity of the polarization being small^{3,2,5}, this diffracted homodyne beam is of small amplitude. It must also be noted that now a component of the signal beam will interfere with the read-out beam. Fortunately, because of the frequency difference between both beams, the non-stationary fringe pattern will not be recorded in the PRC.

Another important optimization factor concerns the nature of the applied electric field. An ac rather than a dc electric field is preferred since this leads to increased stability, and allows partial illumination of the crystal, avoiding the electrode shadowing problem^{3,2,6}. The field that leads to the highest diffraction efficiency improvement is the square field. Unfortunately, the

generation of a high amplitude and high frequency square voltage is not easily done. Furthermore, one must keep in mind that the internal electric field differs from the applied electric field^{3.2.7}. When an ac field of 4kHz is applied, we find that the optical density has to be less than 2.8 mW/cm² in order for the internal field to follow the external applied field. For higher optical densities, the charges in the PRC have time to redistribute^{3.2.7} and the effect of the applied field is reduced. For our application, due to the simplicity of using resonant high voltage circuitry, a sinusoidal ac field is chosen.

3.2.5 ULTRASOUND DETECTION

We use a 600mW Argon laser emitting at 514nm. The frequency shift f_B introduced by the Bragg cell is 40MHz. An ac sinusoidal electric field of frequency 3 kHz and of amplitude 7.8kV/cm is applied along the <001> crystallographic axis of a 5x10x10mm³ BSO crystal.

Figure 3.2.3 shows the instantaneous ultrasonic signal detected on a rough aluminum surface. The ultrasonic signal is generated using a surface wave piezoelectric transducer of 5MHz central frequency. Both the generation and detection are on the same side of the aluminum specimen. The total optical intensity density onto the crystal is 1.6 W/cm² and the intensity received onto the photodiode is 0.6 mW. The modulation depth M of the heterodyne signal is measured at 40%. The electronic detection bandwidth used is 15 MHz and the rms noise level measured from the instantaneous signal is 0.066nm, corresponding to a sensitivity^{3.2.8} of $S=0.42 \times 10^{-6} \text{ nm} \cdot \sqrt{\text{W/Hz}}$. This value compares very well with the shot noise limited sensitivity $S=0.40 \times 10^{-6} \text{ nm} \cdot \sqrt{\text{W/Hz}}$, calculated using a detector quantum efficiency $\eta=0.4$ and $M=40\%$.

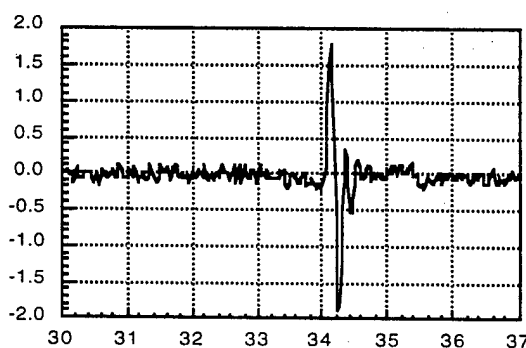


Fig. 3.2.3: Instantaneous ultrasonic signal detected on an aluminum specimen

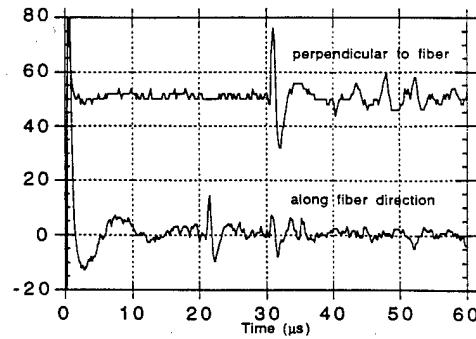


Fig.3.2.4: Ultrasonic signal detected on a graphite-epoxy composite specimen.

Figure 3.2.4 shows an example of application to laser-based ultrasonics on a composite material. In this experiment, the generation of surface waves is done using an Nd-YAG laser operating at 15 mJ per pulse with pulse duration of 20ns. The laser beam is focused to a line, resulting in a propagation direction of the acoustic surface wave perpendicular to the line. A graphite epoxy composite material made of 100 unidirectional layers is used. The detection is achieved without any surface preparation of the composite material which is almost black. Due to the poor optical reflection of the composite material surface, the object intensity decreases by a factor 16 compared to that from a rough aluminum specimen. This decrease of signal intensity leads to a lower SNR. For this experiment, we find a sensitivity $S=2.1 \times 10^{-6} \text{ nm} \cdot \sqrt{\text{W/Hz}}$. The top trace in Fig. 3.2.4 shows the recorded wave for propagation perpendicular to the fiber direction and the bottom is for propagation along the direction of the fibers. As expected, due to the higher velocity in the graphite fibers, the surface wave propagating along the direction of the fiber is faster than the surface wave propagating perpendicular to the direction of the fibers.

3.2.6 REFERENCES

- [3.2.1] J. P. Monchalin, "Optical detection of ultrasound", *IEEE Trans. Ultrason. Ferroelectr. Freq. Control*, vol. 33, pp. 485-499, 1986.
- [3.2.2] R. K. Ing, J. P. Monchalin, "Broadband optical detection of ultrasound by two-wave mixing in a photorefractive crystal", *Appl. Phys. Lett.* vol. 59, pp. 3233-3235, 1991
- [3.2.3] R. K. Ing, B. F. Pouet, S. Krishnaswamy, D. Royer, "Ultrasound detection on rough surfaces using heterodyne photorefractive interferometer: applications to NDE", *1996 IEEE Ultrasonics Symposium*, pp. 681-684, San Antonio, 1996.
- [3.2.4] E. V. Mokrushina, A. A. Nechitailov, V. V. Prokofiev, "Effect of low chromium impurity on properties of photoinduced charge carriers in BTO and BSO single crystals" *Optics Communications*, vol. 123, pp. 592-596, 1996.
- [3.2.5] A. Marrakchi, R. V. Johnson, A. R. Tanguay, "Polarization properties of enhanced self-diffraction in sillenite crystals", *IEEE J. Quant. Elec.* Vol. QE-23, pp. 2142-2151, 1987.

- [3.2.6] K. Walsh, A. K. Powell, C. Stace, T. j. Hall, "Techniques for the enhancement of space-charge fields in photorefractive materials", *J. Opt. Soc. Am. B*, vol. 7, pp. 288-303, 1990.
- [3.2.7] A. Grunnet-Jepsen, I. Aubrecht, L. Solymar, "Investigation of the internal field in photorefractive materials and measurement of the effective electro-optic coefficient", *J. Opt. Soc. Am. B*, vol. 12, pp. 921-929, 1995.
- [3.2.8] J. W. Wagner and J. B. Spicer, "Theoretical noise-limited sensitivity of classical interferometry", *J. Opt. Soc. Am. B*, vol. 4, pp. 1316-1326, 1987.

4. Publications Arising from this Task:

- [1] B.F. Pouet, R.K. Ing, Sridhar Krishnaswamy, and D. Royer, (1996) "Heterodyne interferometer using two wave mixing in photorefractive crystals for ultrasound detection on rough surfaces," *Applied Physics Letters*, vol. 69, No. 25.
- [2] R.K. Ing, B.F. Pouet, Sridhar Krishnaswamy and D. Royer, (1997), "Adaptive Heterodyne Photorefractive Interferometer for Ultrasound Detection: Optimization and Applications," Proceedings of the IEEE UFFC 1997 Symposium, Toronto, Oct. 5-8 1997.
- [3] R. K. Ing, D. Royer, Bruno F. Pouet, Sridhar Krishnaswamy, (1996), "Ultrasound detection on rough surfaces using heterodyne photorefractive interferometer: applications to NDE", *IEEE Ultrasonics Symposium*, pp. 681-684, San Antonio, Nov. 1996.
- [4] B.F. Pouet and Sridhar Krishnaswamy, (1996), "Dynamic Holographic Interferometry by Photorefractive Crystals for Quantitative Deformation Measurements," *Applied Optics*, vol. 35, No. 5, pp. 787-794.
- (*selected to appear in SPIE's Milestone series on Holographic Interferometry*)
- [5] B.F. Pouet and Sridhar Krishnaswamy, (1996), "Phase Shifting Dynamic Holographic Interferometry using BSO Photorefractive Crystals," in SPIE vol. 2921, Proceedings of the First International Conference on Experimental Mechanics, Singapore, Dec. 1996.
- [6] B.F. Pouet and Sridhar Krishnaswamy, (1995), "Application of Photorefractive Crystals for Holographic Interferometry of Vibrating Diffuse Specimens," *Optical Engineering Midwest*, SPIE vol. 2622; {Chicago, May 1995}.

TASK 2. NDE THEORY AND TECHNIQUES (Northwestern University)

Task 2.2.5 Measurement Models for Ultrasonics

1. Objectives:

The objective of Task 2.2.5 is to develop measurement models for selected ultrasonic measurement systems. A measurement model's principal purpose is to predict, from first principles, the measurement system's response to specific anomalies in a given material or structure, e.g., cracks, voids, distributed damage, corrosion, deviations in material properties from specification, and others. Thus, a measurement model includes the configuration of probe and component being inspected, as well as a description of the generation, propagation and reception of the interrogating energy.

The availability of a measurement model has many benefits. Numerical results based on a reliable model are very helpful in the design and optimization of efficient testing configurations. A good model is also indispensable in the interpretation of experimental data and the recognition of characteristic signal features. The relative ease of parametrical studies based on a measurement model facilitates an assessment of the probability of detection of anomalies. A measurement model is a virtual requirement for the development of an inverse technique based on quantitative data. Last, but not least, a measurement model whose accuracy has been tested by comparison with experimental data provides a practical way of generating a training set for a neural network or a knowledge base for an expert system.

2. Recent Accomplishments:

In early work on this project, the authors have presented theoretical and experimental results for the generation of focused surface wave motion by a linear array of surface wave transducers. It was shown that a single element generates a beam with an opening angle of approximately 20° , and a cross section which can be accurately represented by a Gaussian distribution of the normal displacements. For an eight-element array, the focused beam was modeled by superposition considerations. Comparisons of theoretical and experimental results, where the latter were obtained by the use of a laser interferometer, showed excellent agreement for the normal displacement both along a radial line and across the width of the beam. The transducer array with a center frequency of 5MHz was used for surface-defect detection, whereby the focal region was automatically adjusted to the defect location.

In recent work these results have been used to construct a measurement model for the ultrasonic measurement of the signal backscattered from a surface-breaking crack. The signal scattered back from the defect has been expressed in terms of a scattering coefficient based on the use of an elastodynamic reciprocity relation. The Kirchhoff approximation was used to compute the scattering coefficient for the experimental configuration. This approximation can be applied if the defects are considerably larger than the ultrasonic wavelength, and if the angle between incident field and backscattered field is small. A simplification of the mathematical description was achieved by using the plane-wave reflection coefficient for a surface wave derived by Achenbach *et al.* and Gautesen.

The array scattering coefficient was calculated for half-penny-shaped surface-breaking cracks and the theoretical values were compared with experimental results. Two half-penny-shaped EDM notches of different sizes were introduced into an aluminum slab. Very satisfactory agreement between theoretical prediction and experimental observation was obtained.

The transducer array which is placed on an acrylic wedge was positioned, such that the main propagation direction is x_1 . Each element produces surface waves within an opening angle that has been determined experimentally. An asymptotic solution at large r has also been derived, which can be used to construct the displacement field generated by a single element, at some distance from the element, in the general form

$$u_3(r, \theta, t) = \frac{e^{\frac{\theta^2}{2\theta^2}}}{\sqrt{r}} f\left(t - \frac{r}{c_R}\right), \quad (1)$$

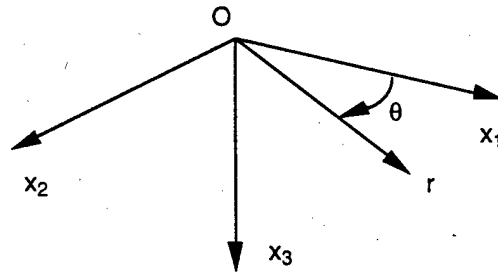


Figure 1. Coordinate system for surface waves.

where $r = \sqrt{x_1^2 + x_2^2}$ is the distance between the observation point and the source and where $\theta = \text{atan}(x_2 / x_1)$ is the polar angle in the x_1x_2 -plane, see Fig. 1. The array element is located at the origin of the coordinate system. The function $f(-)$ has been determined

experimentally, and c_R is the velocity of Rayleigh surface waves. The dependence on r resembles the solution for a point source of surface waves. The dependence on θ can be accurately approximated by a Gaussian distribution, as shown in Eq. (1). The angle $\hat{\theta}$ corresponds to the width of the Gaussian.

After establishing a model for a single array element, the field generated by the entire array is obtained by superposition

$$u_{3ARRAY}(\vec{r}, t) = \sum_{n=1}^8 u_{3,n}(\vec{r} - \vec{Pos}(n), t - T_n), \quad (2)$$

where n represents the element number, $Pos(n)$ are the positions of the array elements, and T_n are the excitation times of the individual elements in order to produce a focused wave at the focal point

$$T_n = \frac{r_F}{c_R} \left\{ 1 - \sqrt{1 + \left(\frac{Pos(n)}{r_F} \right)^2 - 2 \left(\frac{Pos(n)}{r_F} \right) \sin \varphi_F} \right\}, \quad (3)$$

where the position of the focal point is given in polar coordinates r_F and φ_F . The array is aligned parallel to the x_2 -axis and the center of the array coincides with the origin of the coordinate system. Therefore, the angle φ_F in Equation (3) is the steering angle of the array.

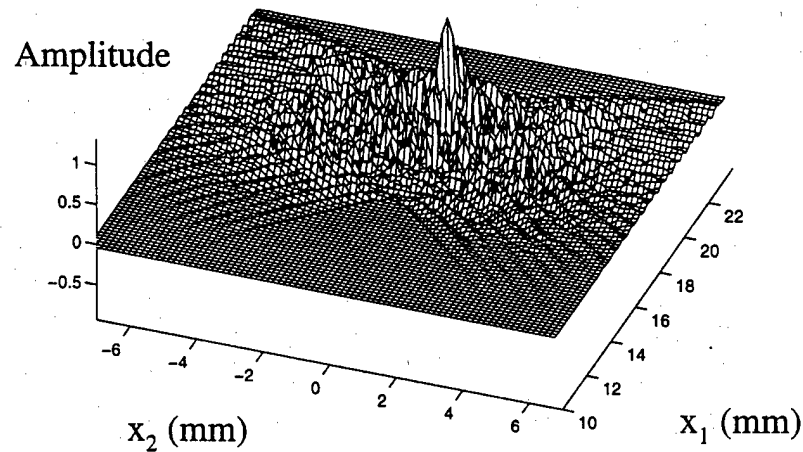


Figure 2 shows a snapshot of the calculated displacements for on-axis focusing of the array.

Figure 2 shows a snapshot of the calculated displacement distribution over the specimen surface with the focal point located at $x_1=20$ mm, $x_2=0$. The time delays for each element were chosen for optimal constructive interference. Figure 3a and 3b show cross sections of the snapshot along $x_2=0$ and $x_1=20$ mm, respectively. Both traces show the focusing effect. To compare the calculated results for the entire array with experimental results, the array was mounted on a flawless specimen and the focal point was adjusted for on-axis focusing ($x_1 = 0$ mm and $x_2 = 40$ mm). The normal displacement u_3 was measured across the focal point. The maximum peak to peak amplitude of the displacement along the center axis, and across the focused beam have been displayed elsewhere for comparison with numerical results. Across the beam, a main lobe and two side lobes of lower amplitude were observed. Good agreement between theoretical and experimental results was obtained.

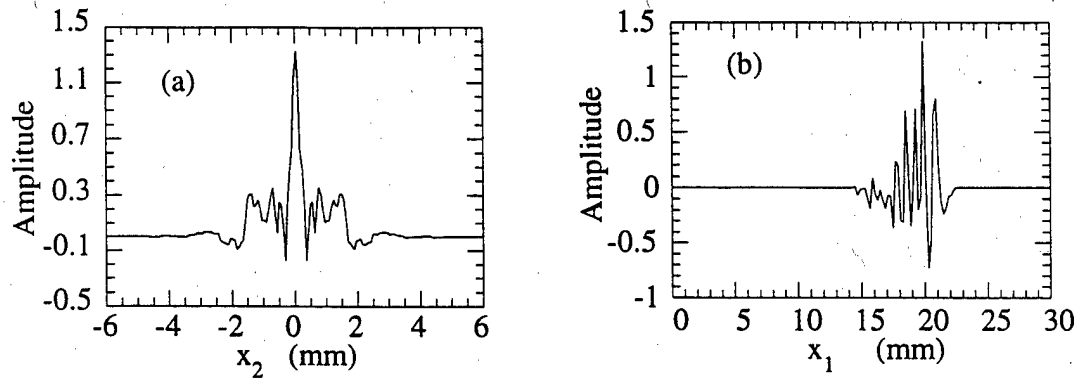


Figure 3. Cross sections of the snapshot along $x_1=20$ mm and $x_2=0$, respectively.

It has been shown that the scattering coefficient due to the presence of a crack, which is defined as

$$\overline{M}_{21} = M_{21}^F - M_{12}^{NF}. \quad (4)$$

can be expressed as

$$\overline{M}_{21} = \frac{1}{2 (A_{1T})^{(1)} (A_{2T})^{(2)} I^{(0)}} \int_{S_F} (\sigma_{ij}^{(2)} u_i^{(1)}) n_j dS. \quad (5)$$

where

$$I^{(0)} = \int_{S_1} (\sigma_{ij}^{(0)} u_i^{(0)}) n_j dS = \int_{S_2} (\sigma_{ij}^{(0)} u_i^{(0)}) n_j dS. \quad (6)$$

The integral $I^{(0)}$ is introduced for the integration over the transducer surface of the inner product of the reference displacement $u_i^{(0)}$ and the reference traction $\sigma_{ij}^{(0)} n_j$. It is assumed

that both transducers have the same surface area and are operated under the same conditions and therefore we can use for both transducers. Equation (5) describes the scattering of elastic waves for a flaw within a volume V if transducer 1 is used to sonify the volume. The characteristics of the transducers are incorporated by the amplitude constants for transmission and by the integral $I^{(0)}$. The stress $\sigma_{ij}^{(2)}$ in Equation (5) may be called the virtual stress produced by transducer 2 at the location of the flaw for the case that there is no flaw in the system. The displacement $u_i^{(1)}$ is caused by transducer 1 and is the actual displacement on the surface of the flaw.

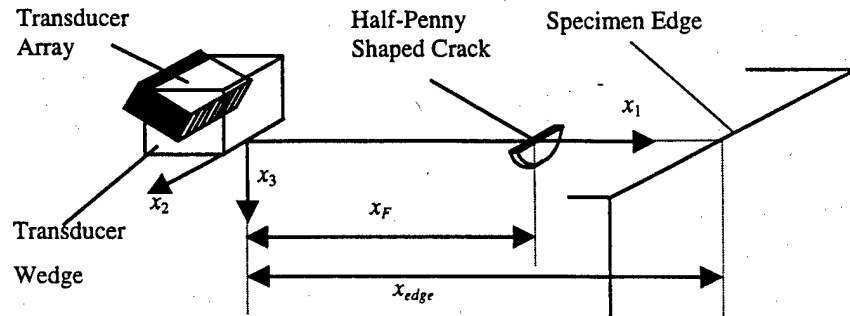


Figure 4. Focusing of Rayleigh waves on surface-breaking half-penny shaped cracks.

Equation (5) has been applied for the configuration shown in Figure 4. A linear surface wave array consisting of eight elements is used to sonify surface-breaking cracks of half-penny shape with a diameter d and a small width w . The array, both plane flaw faces and the specimen edge are all parallel to the x_2 -axis. The specimen surface defines the x_1x_2 -plane. Focused surface wave motion at the flaw location is generated by the transducer array which is coupled to the specimen surface with an acrylic wedge. The focal distance is x_F , and the distance between array and specimen edge is called x_{edge} .

The expression for focused surface wave motion can be used to compute the relevant fields. It has also been shown that the surface wave motion mainly affects the x_1x_3 -plane, i.e. the displacement u_2 and the stress σ_{12} are negligible. If we also assume that the flaw dimensions are larger than the ultrasonic wavelength and that most of the sound energy is reflected back into the direction of the incident wave, it is possible to apply the Kirchhoff approximation for this problem.

Figure 5 shows the experimental results for the scattering coefficients of the 2 mm and the 3 mm crack versus their theoretical values. A constant to scale the theoretical curve for the 3 mm crack was calculated by minimizing the error-squares between theoretical and experimental curve. The same constant is then used to scale the theoretical curve of the

2 mm crack. Good agreement of theory versus experiment has been obtained for both cracks.

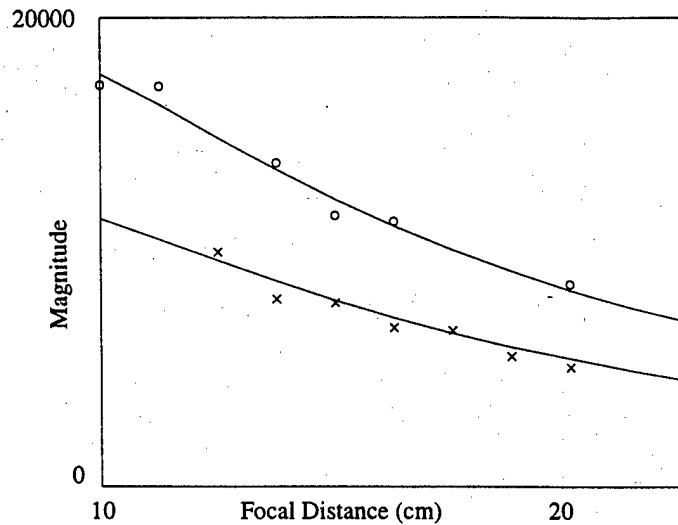


Figure 5. Comparison of theoretical scattering coefficient (solid lines) with experimental data for a 2 mm crack (crosses) and a 3 mm crack (open circles).

3. Publications on this Task:

1. J. D. Achenbach, I. N. Komsky and M. Zhang, "Oblique Pitch-Catch Imaging of Defects in Multi-Layered Structures, Acoustical Imaging, Vol. 22, Plenum Press, New York, pp. 745-750, 1996.
2. K. Zgonc and J. D. Achenbach, "A Neural Network for Crack Sizing Trained by Finite Elements Calculations," NDT & E International, Vol. 29, pp. 147-155, 1996.
3. Ming Zhang and J. D. Achenbach, "Numerical Simulation of Self-Focusing of an Array on an Interior Crack," Review of Progress in Quantitative Nondestructive Evaluation, D. O. Thompson and D. E. Chimenti, Eds., Plenum Press, New York, Vol. 17B, pp. 1705-1712, 1998.
4. W. A. K. Deutsch, A. Cheng and J. D. Achenbach, "Focusing of Rayleigh Waves: Simulation and Experiments," IEEE Transactions on Ultrasonics, Ferroelectrics and Frequency Control, in press.

TASK 2. NDE THEORY AND TECHNIQUES (Northwestern)

Task 2.3 Self-Focusing Techniques for Ultrasonic NDE Methods

1. Objectives:

The effectiveness of an ultrasonic technique for flaw detection and characterization can be greatly enhanced by a capability to focus ultrasound by the use of a focused transducer. A conventional ultrasonic focused transducer is, however, rather inflexible in that its direction of ultrasound radiation and its focal length are fixed. Direct focusing on a flaw is therefore often not possible or at least requires mechanical scanning. Greater flexibility can be obtained by the use of a phased array which can electronically generate a focal spot in the acoustic beam at a specified location and beam angle. A significant further improvement can be obtained by the use of a self-focusing technique that automatically focuses the beam on a flaw. The objective of the work reported here is to develop a self-focusing array and technique for the detection of defects in aircraft and engine components.

2. Accomplishments/New Findings:

In early work on the project, reported in a paper by Beardsley, Peterson and Achenbach, a self-focusing technique and its application to a linear array system have been developed. By application of this technique, the system is capable of both sonification and reception focusing. A low cost linear array was constructed to implement the self-focusing technique on a specimen in a water tank. Examples were presented to demonstrate the capability of the array to self-focus on single flat-bottom holes, as well as on the largest hole among a set of three holes in an aluminum specimen.

The work on self-focusing was extended to surface waves and Lamb waves, as reported in a paper by Deutsch, Cheng and Achenbach. An array of contact transducers has been constructed to generate surface waves and Lamb waves in thin-walled aircraft structures. The array has the capability to focus and thereby detect and size small cracks such as occur in widespread fatigue damage.

More recently an ultrasonic measurement model was developed to simulate self-focusing by a curved array of transducers on an interior crack. The far field radiated by each transducer element was modeled by rays with a Gaussian distribution of amplitudes over the beam width. The ray tracing method was used to determine both the focused wave field in the immersed specimen and the travel times from each array element to the crack. The self-focusing array was modeled for both sonification and reception focusing. The transducers in the array were excited with the appropriate time delays to achieve sonification focusing. After the incident wave field on the crack had been obtained, the crack opening volume was calculated.

For a pair of transducers, a reciprocal identity for two media in contact was used to determine the amplitudes of signals scattered back from the crack. The field transmitted and received by the entire array was obtained by superposition. Reception focusing was used to adjust the differences in signal arrival times for in-phase signal summation. It was shown that considerable signal amplification can be achieved by the self-focusing procedure, as was shown by comparison of scattered fields.

In further work, a method using a linear array to self-focus on an opposite side surface breaking crack and to detect the inclination angle of the crack was presented. The adaptive time-delay focusing technique was used. The far field of the transmitted waves from each transducer element of the array was modeled by rays with a Gaussian distribution of amplitudes over the beam width. The focused incident wave field in an immersed plate was modeled with the ray tracing method to show the energy concentration by self-focusing of ultrasound and to obtain the incident angle of the resulting focused displacement at the focal point. The inclination angle of the crack was determined by adjusting the array to a position so that the array was performing on-axis focusing on the crack and the resulting focused displacement of the incident wave was perpendicular to the surface of the crack.

For a surface-breaking crack which is normal to the surface of the plate, the self-focusing technique has been used to focus longitudinal waves on the edge of the crack. A comparison of edge diffracted fields for the focused and un-focused cases showed that considerable signal amplification has been obtained and the signal to noise ratio has been improved by the self-focusing technique. The location of the crack edge can be determined accurately from the time-of-flight between the array and the crack edge after application of the self-focusing technique.

For the simulation of self-focusing on an interior crack, the configuration for the modeling is shown in Figure 1. The array consists of eleven transducers. It is circularly pre-focused with a radius of curvature of 330mm. The array transducers are rectangular in shape with a width of 4mm and a height of 5mm. The natural focal point is located on the axis and behind the crack. The velocity V_0 of the transducer surface generated by a single pulse is shown in Figure 2. The pressure signal p^{ref} transmitted by a single element at the reference point has a center frequency of 5 MHz and the band width is about 2 MHz at 6dB attenuation.

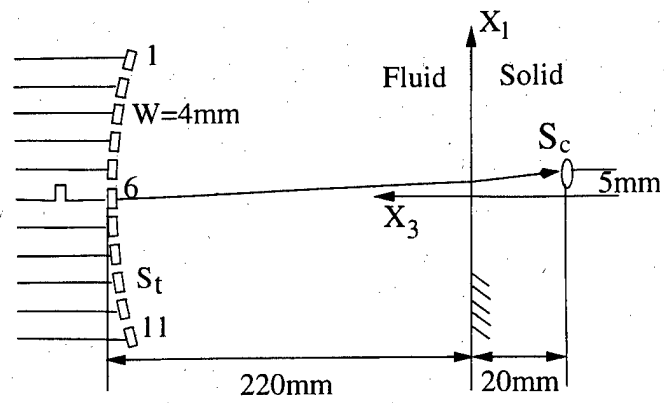


Figure 1: A system for detecting an interior crack.

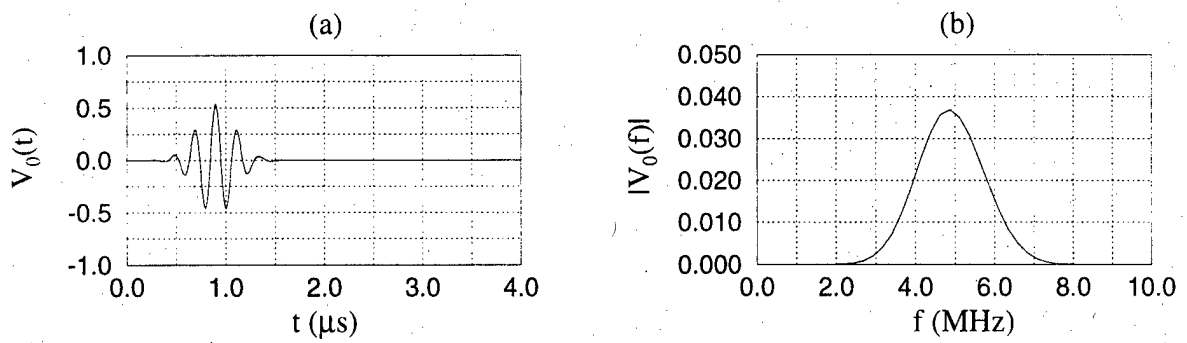


Figure 2: Velocity generated by single element transducer (a) in time domain (b) in frequency domain.

The focused displacement wave field in the specimen is the superposition of the displacement wave fields generated by each array element. For the case of on-axis focusing, the displacement field in direction x_1 is zero after superposition while in the case of off-axis focusing, the displacement field in direction x_1 is very small and it is omitted in the calculation. The focused displacement field in the x_3 direction is the superposition of the displacement field generated by each array element in the x_3 direction at the focal point

$$u_3(x_i, t) = \sum_{n=1}^{11} u_3^n(x_i - X_n, t - T_n) \quad (1)$$

where X_n is the location of the center point of ray radiation for the n th element and T_n is the excitation time delay. The excitation time delay is obtained by calculating the travel time differences from the array elements to a focal point in the specimen. Appropriate time delays are applied to array elements so that the maximum amplitudes of the displacement signals arrive at the focal point at the same time. Figure 3 shows the normalized displacement field of u_3/u_{pk}^{ref} when the ultrasound is on-axis focused. Here u_{pk}^{ref} is the peak-to-peak value of the reference displacement. The direction of u_3 is normal to the surface of the crack. The superposition of signals from each array element results in a peak amplitude at the focal point (0,0,-20)mm. By adjusting the time delays to each array element, the array focal point can be steered in the x_1x_3 plane as shown in Figure 4 where the focal point is moved to 5mm off-axis. There is a peak amplitude at the focal point (5,0,-20)mm, but the normalized amplitude is smaller than for on-axis focusing.

The received voltage signal is proportional to the pressure field at the transducer surface and can be represented by the received pressure signal. The total received signal p_A by the array is the superposition of the received pressure signal p_i^R by each array element. The numerical simulations have been performed for various configurations as shown in Figure 5. In the following numerical calculations, 80dB amplification has been applied to the scattered pressure signals and the received pressure signal p_A has been normalized to the peak-to-peak value of the pressure at the reference point. The first case shown in Figure 5(a,b) is for a circular crack with radius equal to 0.2mm. The signals are transmitted with appropriate time delays to achieve the sonification focusing and reception focusing is used to sum up the received signals. The total received signal is clean with a large amplitude.

The second case shown in Figure 5(c,d) is for the same configuration and crack size, but without applying self-focusing. The signals are sent out at the same time and the received amplitudes are summed up without reception focusing. The total displacement signal is not as nice and the amplitude is much smaller compared with the one calculated for self-focusing. The advantage of the self-focusing can be seen by comparing Figure 5(a) with Figure 5(c) and Figure 5(b) with Figure 5(d).

The third case shown in Figure 5(e,f) is for a circular crack with a smaller radius (0.1mm). The self-focusing procedure has been performed. For the smaller crack,

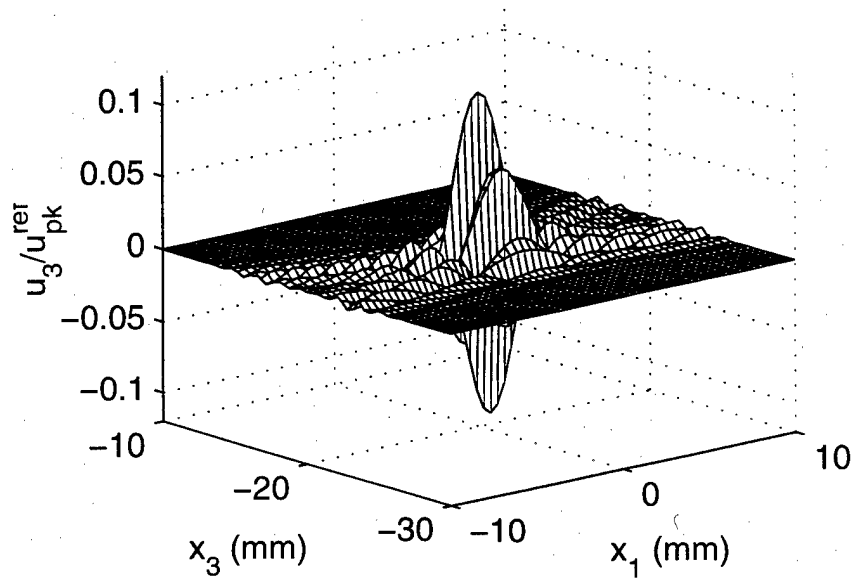


Figure 3: Normalized displacement field of u_3/u_{pk}^{ref} , on-axis focused.

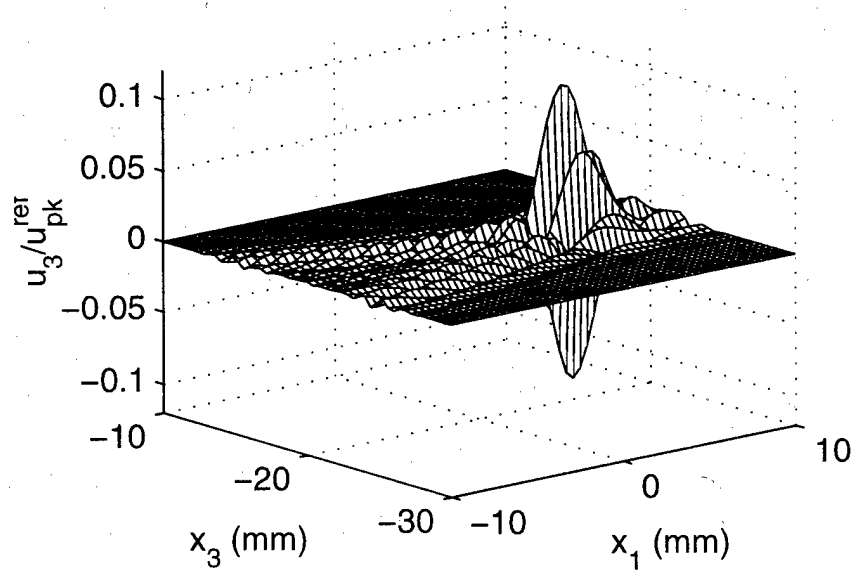


Figure 4: Normalized displacement field of u_3/u_{pk}^{ref} , off-axis focused at a point which is 5mm off the symmetric axis.

the same incident field will cause a smaller crack opening volume. Therefore, the scattering coefficient will be much smaller. The displacement amplitude is about one ninth of the one shown in Figure 5(a).

The last case shown in Figure 5(g,h) is for an elliptical crack with the long axis equal to 0.2mm and the short axis is 1/3 of the long axis. The self-focusing procedure has been performed. The crack opening volume of the elliptical crack is small and the final displacement signal is small as compared with the one for the circular crack of the first case. We also note from the plots in the frequency domain shown in Figure 5(f,h), that the small crack and the elliptical crack scatter more high frequency components as compared to the bigger circular crack.

The time-reversal mirror (TRM) method may focus better on a target through an inhomogeneous medium. The TRM method reportedly can compensate for distortions due to the inhomogeneity of the medium. However, the cost of the TRM electronic system is much higher than that for a time-delay method. For an isotropic, homogeneous and linearly elastic material, the numerical simulation of the two different self-focusing methods should show similar focusing effects. Only results for the adaptive time-delay method are presented in the paper.

For a surface-breaking crack which is normal to the surface of the plate, the self-focusing technique has been used to focus longitudinal waves on the edge of the crack. The set-up of the experiment is shown in Figure 6. The incident waves are indicated by solid lines and the diffracted waves are indicated by dotted lines.

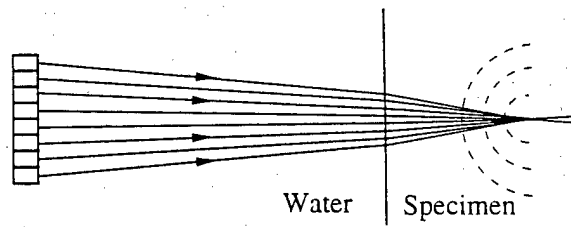


Figure 6: Self-focusing on the edge of a surface-breaking crack.

The results for the self-focusing process are shown in Figure 7. The signals are transmitted with appropriate time delays to achieve the sonification focusing. The Figure 7(a) shows the received signals after sonification focusing has been applied. In the reception focusing all signals are aligned with the earliest arrival so that peaks and valleys now occur at the same time. This ensures constructive interference for the focused signal. A large focused signal is obtained by superposition of the signals after reception focusing.

Figure 8 shows the results for the un-focused case. For un-focused transmission all elements were fired at the same time. The peak-to-peak amplitude of the backscattered signal is small and the signal to noise ratio is low. The superposition

of the eight received signals without time shifts is very noisy and the defect reflection signal cannot be distinguished clearly.

The advantage of the self-focusing can be observed by comparing the results for the focused and un-focused cases. The self-focusing procedure improves the signals significantly. The focused signal has a higher signal to noise ratio and it has a large amplitude. The time of flight from the array to the edge of the crack can be determined accurately from the focused wave signal, and the location of the crack edge can subsequently be determined from the time of flight.

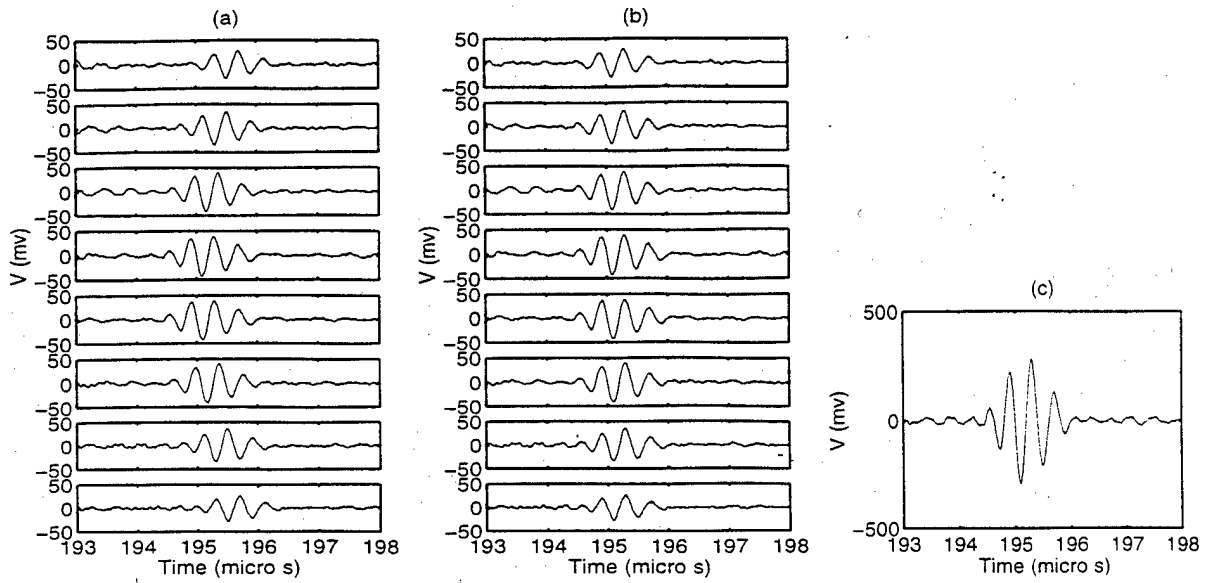


Figure 7: Results for self-focused system. (a) Transmission focusing is applied. (b) Reception focusing is applied. (c) Focused signal.

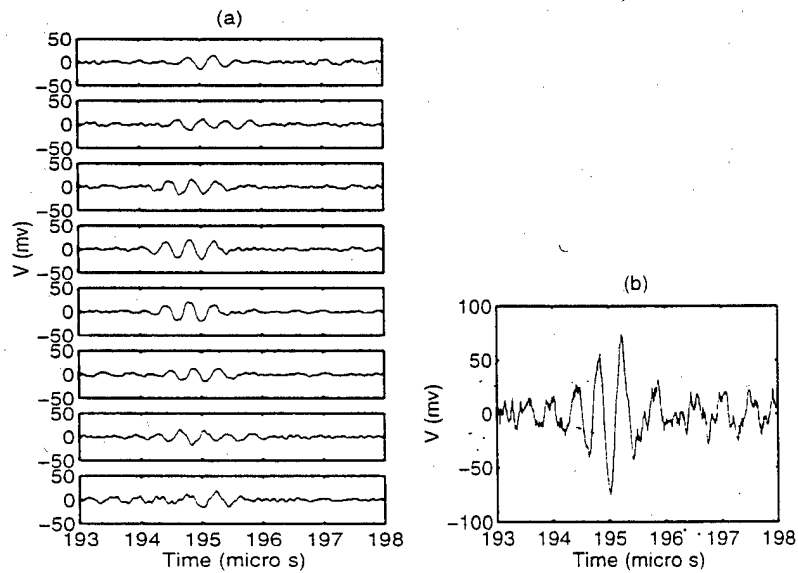


Figure 8: Results for un-focused system. (a) Un-focused transmission. (b) The superposition of un-focused signals.

3. Publications in This Task:

1. B. Beardsley, M. Peterson and J. D. Achenbach. "A Simple Scheme for Self-Focusing of an Array", J. Nondestructive Evaluation, 14: 169-180. 1995.
2. W. A. K. Deutsch, A. Cheng, J. D. Achenbach, "Self-focusing Surface-Wave Array", Review of Progress in QNDE, D. O. Thompson and D. A. Chimenti. Eds., Plenum Press, Vol. 16, 2077-2048, 1997.
3. W. A. K. Deutsch, A. Cheng, J. D. Achenbach, "Self-focusing of Rayleigh waves and Lamb waves with a linear phased array", Res. Nondest. Eval 9:81-95. 1997.
4. W. A. K. Deutsch, A. Cheng, J. D. Achenbach, "Self-focusing of Rayleigh waves: Simulation and Experiment", Review of Progress in QNDE D. O. Thompson and D. A. Chimenti, Eds., Plenum Press, Vol. 17B, 1697-1704, 1998.
5. Ming Zhang and Jan D. Achenbach, "Simulation of Self-Focusing by an Array on a Crack in an Immersed Specimen", Ultrasonics, in press.
6. Ming Zhang, A. Cheng and Jan D. Achenbach, "Self-Focusing by a Linear Array on a Surface-Breaking Crack at the Opposite Side of a Plate", Review of Progress in QNDE, D. O. Thompson and D. A. Chimenti. Eds., Plenum Press, Vol. 18, in press.

Task 4 - DAMAGE DETECTION IN COMPOSITE MATERIALS

Principal Investigator: I. M. Daniel

Contributors: S. C. Wooh, H. J. Chun, J. J. Luo and K. Durkin

1. INTRODUCTION

Damage in composite materials can take various forms, such as delaminations, matrix cracking, fiber/matrix debonding and fiber fractures. Defects may be introduced in composites during processing, and may be induced or enlarged in service with age, loading and environmental conditions. As in the case of other materials it is important to monitor the integrity of the material and components on a continual basis.

An important application of composite materials is in structural reinforcement and repair of aging aircraft. Composite repair patches are usually boron/epoxy or carbon/epoxy laminates adhesively bonded to the aluminum substrate where damage, such as fatigue or stress corrosion cracking, exists or is anticipated. The effectiveness and reliability of such repairs needs to be demonstrated and established.

The detection and characterization of defects and damage in composite materials and repair patches are usually accomplished by a variety of nondestructive evaluation methods. These include ultrasonic, radiographic, acoustic and acousto-ultrasonic methods.

This report describes the application and results of nondestructive evaluation (NDE) and other methods to the detection and characterization of the integrity of composite materials and the evaluation of the effectiveness and reliability of composite repairs for aging aircraft. Real-time NDE methods were developed and applied to composite laminates under monotonic loading to failure. Results from ultrasonic, acoustic emission (AE) and matrix cracking measurements were correlated with the macroscopic response of the material and its degradation. The effectiveness of composite patches in controlling damage propagation in a cracked aluminum substrate under fatigue conditions was also investigated by means of ultrasonic and acousto-ultrasonic methods.

2. REAL-TIME MONITORING OF DAMAGE DEVELOPMENT

2.1 Introduction

Studies on damage development in composite laminates have been conducted by many investigators [1-3]. In the case of crossply laminates under uniaxial tensile loading, whether monotonic or cyclic, the first stage of damage consists of transverse matrix cracking in the 90° plies. These cracks are nearly equidistant and increase in density up to a characteristic limiting value. In the later stages of loading, the damage evolves so that longitudinal cracks are generated in the 0° plies, followed by micro-delaminations at the intersections of the two sets of cracks, and finally fiber failures leading to global failure [1].

As the damage evolves, material properties are degraded. In particular, stiffness degradation due to matrix cracking is a significant indication of damage [4-6] and the measurement of matrix crack density is important in the prediction of residual life. It is often desirable to evaluate such damage in the material nondestructively.

For distributed types of damage, such as matrix cracking, stiffness degradation is related to residual strength and residual life. Currently available models provide relations between stiffness and damage state. Thus, if the damage state can be detected and characterized nondestructively, it is possible to use such nondestructive measurements for life prediction.

In this study, a real time nondestructive evaluation method was developed and applied to detection of damage evolution in composite materials for the purpose of developing damage accumulation and life prediction models. An attempt was made to characterize the damage and to correlate the ultrasonic backscattered energy and acoustic emission readings with damage in real time.

2.2 Experimental Procedure

The material used was IM7/8551-7A (Hercules) carbon/epoxy received in prepreg form. It was fabricated into coupons of $[0/90_4]_s$ crossply layup for mechanical and

nondestructive testing. The specimen was loaded in a servo-hydraulic tensile testing machine controlled by a host microcomputer while the damage was monitored by ultrasonic and acoustic emission (AE) methods. Figure 1 shows schematically the setup used in this study.

It is important to monitor crack density in real time as the material is loaded. Penetrant-enhanced X-radiography has been widely used as a means of measuring crack density because of its superior resolution in detecting cracks and other small flaws. However, the method is not suitable for real-time monitoring as it requires specimen preparation with an X-ray opaque penetrant, and interruption of specimen loading.

An alternative approach based on ultrasonic backscattering has been demonstrated by Wooh and Daniel [9]. The specimen, immersed in a water tank, is scanned with a relatively high frequency (10 MHz) focused transducer at oblique incidence. The ultrasonic beam is aimed in the direction perpendicular to the cracks in order to provide maximum polar backscatter from the cracks. The specimen is then scanned in a raster fashion to build an image of the damage. Because of the random nature of the acoustic scattering, the as-obtained image is of poor quality. An image processing algorithm is applied to measure the crack density. Although the method gives the damage map of the specimen for visual investigation, it is inefficient for quantitative measurements since it involves image processing with fuzzy factors. Also, this method may not be adequate for real-time monitoring because it requires interruption of specimen loading.

A different method was developed for quantitative measurement of transverse crack density. Preliminary tests were run in an immersion tank; see Daniel et al. [3]. The method uses exactly the same setup except that an unfocused transducer is used to measure average backscattered energy. The specimen is scanned along a line and the ultrasonic backscattered energy is acquired as a function of transducer location. Assuming that the backscattered energy is proportional to the number of cracks in the ultrasonic beam, a simple prediction was made and a very good correlation between backscattered energy and

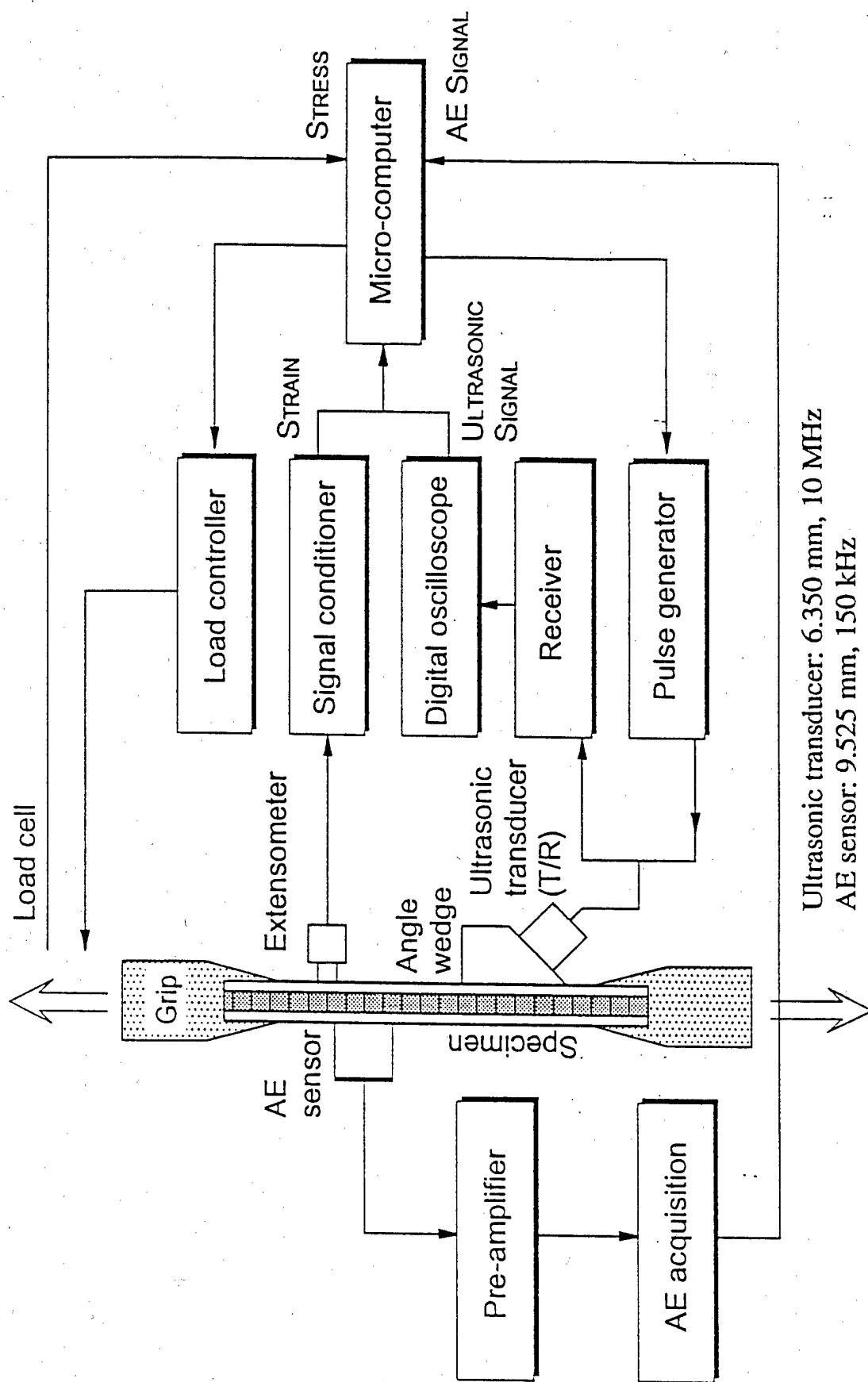


Fig. 1 Schematic Diagram of System used for Real-Time Monitoring of Damage in Composite Materials.

crack density was obtained. This method provides a simple and straightforward procedure for quantitative measurement and proved to be very sensitive.

These methods, however, are not suitable for real-time monitoring because the setup requires immersion of the specimen and the transducer. For real-time measurements, Wooh and Daniel [10] have successfully developed a method using a pair of contact transducers monitoring damage development in ceramic matrix composites. In this study, the method was extended by using an angle wedge mounted on the specimen in contact with the specimen instead of immersion.

An unfocussed transducer of 10 MHz center frequency was mounted on the surface of the specimen while the specimen was loaded in a servo-hydraulic testing machine. Figure 1 illustrates schematically the system setup used in this study. The transducer operating in pulse echo mode sends repetitive ultrasonic pulses onto the specimen at an oblique angle guided by the wedge. The propagating ultrasonic beam is then scattered back to the transducer from the tips of the cracks or other small flaws.

The loading was controlled by a host computer while the ultrasonic signals were acquired by a 200 MHz digitizing oscilloscope. During loading, the stress-strain curve as well as the corresponding backscattered signals at different stress levels were recorded. The as-obtained waveforms were numerically processed to compute the energy of the signal and correlated with the corresponding stress-strain curve.

In addition to the ultrasonic measurements, the edge replication technique was used to measure the crack density at the corresponding stress level for further correlation with ultrasonic measurements. The replication technique has the advantage over X-radiography in that there is no need to unload the specimen. The specimen edge was prepared with quickly evaporating acetone. The edge was then replicated with a thin replication tape (Ernest Fullam) before the acetone evaporated. This procedure can be completed within seconds during a brief pause in the test.

In addition to the ultrasonic backscattering measurements, acoustic emission (AE)

output was monitored with a sensor (9.525 mm dia., 150 kHz center frequency) mounted in contact with the specimen. AE signals result from the stress waves generated by the damage occurring in the composite, such as matrix cracking, delaminations, fiber fractures, and friction.

During loading, the acoustic emission output was independently recorded (Locan-AT, Physical Acoustics) and was correlated with corresponding strain levels and failure mechanisms. Since the frequency bands of the ultrasonic transducer and the AE sensor are far apart (10 MHz vs. 150 kHz center frequency), there was no interference between the signals. However, the repetition rate of the ultrasonic pulses may interfere with the AE signals so that proper setting of the pulse repetition rate was important.

Of the many AE parameters, only a few were investigated in this study, amplitude, counts, and events. All kinds of AE signals are possible during loading so that it is necessary to find the characteristics of the signal from various sources in order to identify damage mechanisms. One possible method is to collect waveforms and extract their signature by pattern recognition algorithms or neural networks. However, this technique requires sophisticated instrumentation and is usually beyond the limit of the storage capacity of the available machines. For example, internal friction in the material creates numerous signals of low amplitude which are recorded by the instrument resulting in the overflow of the acquisition memory buffer. An alternative approach was followed in this work by displaying the amplitude and count-frequency in terms of corresponding strain levels as will be discussed in the following section.

2.3 Results and Discussion

Figure 2 shows a typical stress-strain curve and the measured crack density versus strain curve for a $[0/90]_s$ carbon/epoxy laminate. The initial region of the stress-strain curve (A-B) corresponds to the linear elastic behavior of the laminate where no macroscopic damage was found. It is noted that the stress-strain curve deviates from

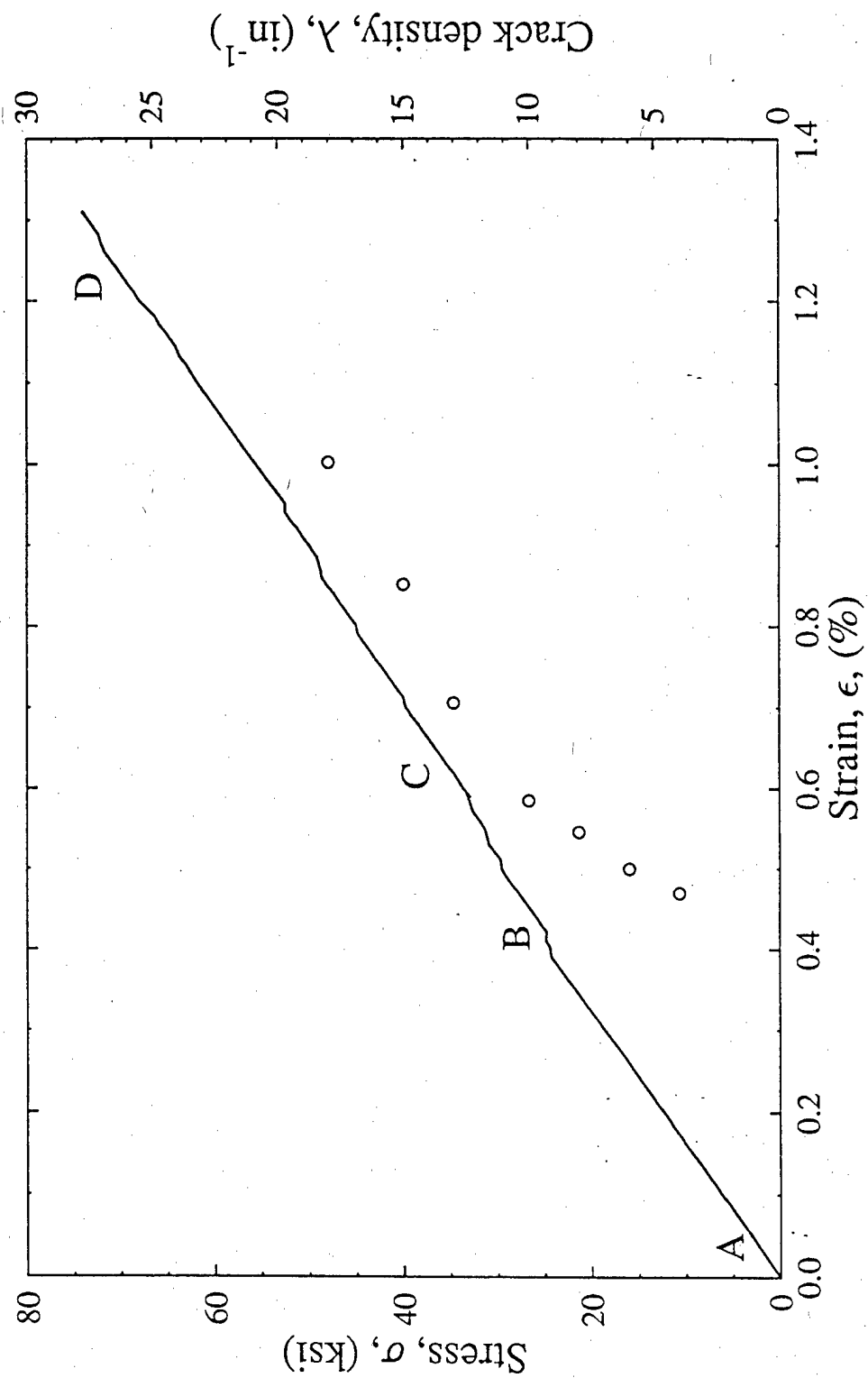


Fig. 2 Stress-Strain Curve and Transverse Crack Density as a Function of Applied Strain for [0/90₄]_s IM7/8551-7A Carbon/Epoxy Laminate.

linearity immediately after the first transverse matrix cracks are observed (Point B). As the load increases, the crack density increases at a constant rate. As a result, the tangential modulus of the material in this range becomes lower than the initial modulus. When the stress level reaches point C, cracking is stabilized or its rate slows down. Beyond this point, in region C-D, various failure mechanisms such as longitudinal matrix cracking, micro-delaminations, and fiber fractures take place. Eventually the laminate fails globally.

Figure 3 shows the stress-strain curve and the measured backscattered energy for a $[0/90_4]_s$ carbon/epoxy laminate. There exist some background scatter signals even for the virgin specimen. The initial energy level represents surface roughness and some material inhomogeneity. As long as the specimen-transducer contact condition remains constant, this quantity remains constant for the entire loading period. Thus, the backscattered energy can be normalized by the initial value before loading. Figure 4 shows typical backscattered signals for various crack densities. It is noted from this figure that the backscattered energy, that is, the area of the signal envelope, increases with increasing crack density.

In linear elastic range, of the stress-strain curve where no damage is found, the backscattered energy is constant. When the first macrocracks appear at approximately 0.55% strain, the stress-strain curve deviates slightly from linearity. In this matrix cracking region, the backscattered energy increases sharply in steps up to the point where cracking stabilizes. It should be noted that there exists some uncertainty in the detection of the first generation of cracks. This is particularly true when the size of the transducer is smaller than the average crack spacing. In our case, the diameter of the transducer was 6.35 mm (0.25 in.) and the minimum detectable crack density was 0.157 mm^{-1} (4 in^{-1}) as shown in Fig. 2.

At the crack stabilization point, the backscattered energy is stabilized or starts decreasing whereas the stress-strain curve becomes linear. In this region, damage appears in the zero degree layers (outer layers). Longitudinal cracks and micro-delaminations as well as fiber fractures in these layers make the ultrasound scatter in different directions and

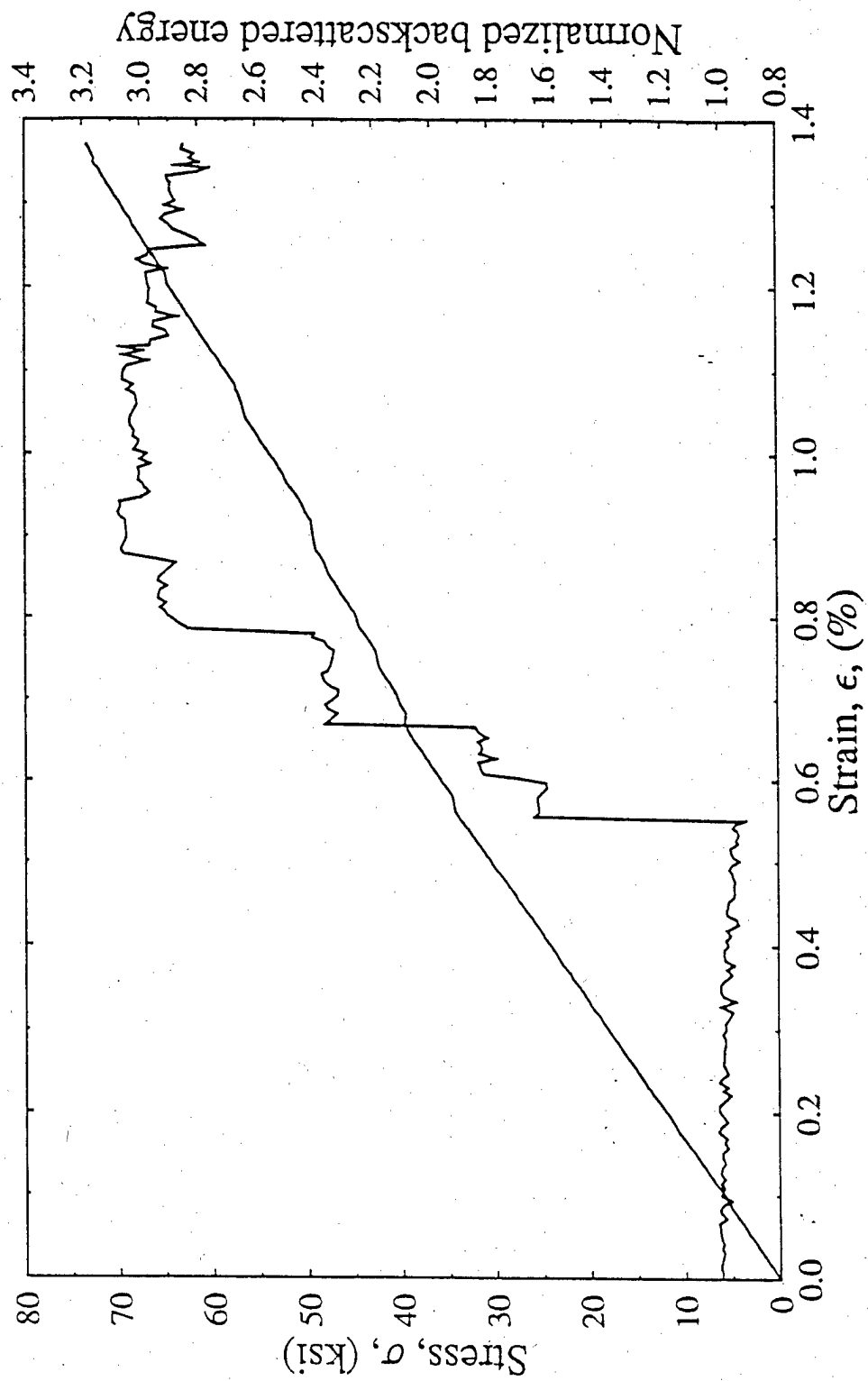


Fig. 3 Stress-Strain Curve and Ultrasonic Backscattered Energy as a Function of Applied Strain for $[0/90_4]_s$ IM7/8551-7A Carbon/Epoxy Laminate.

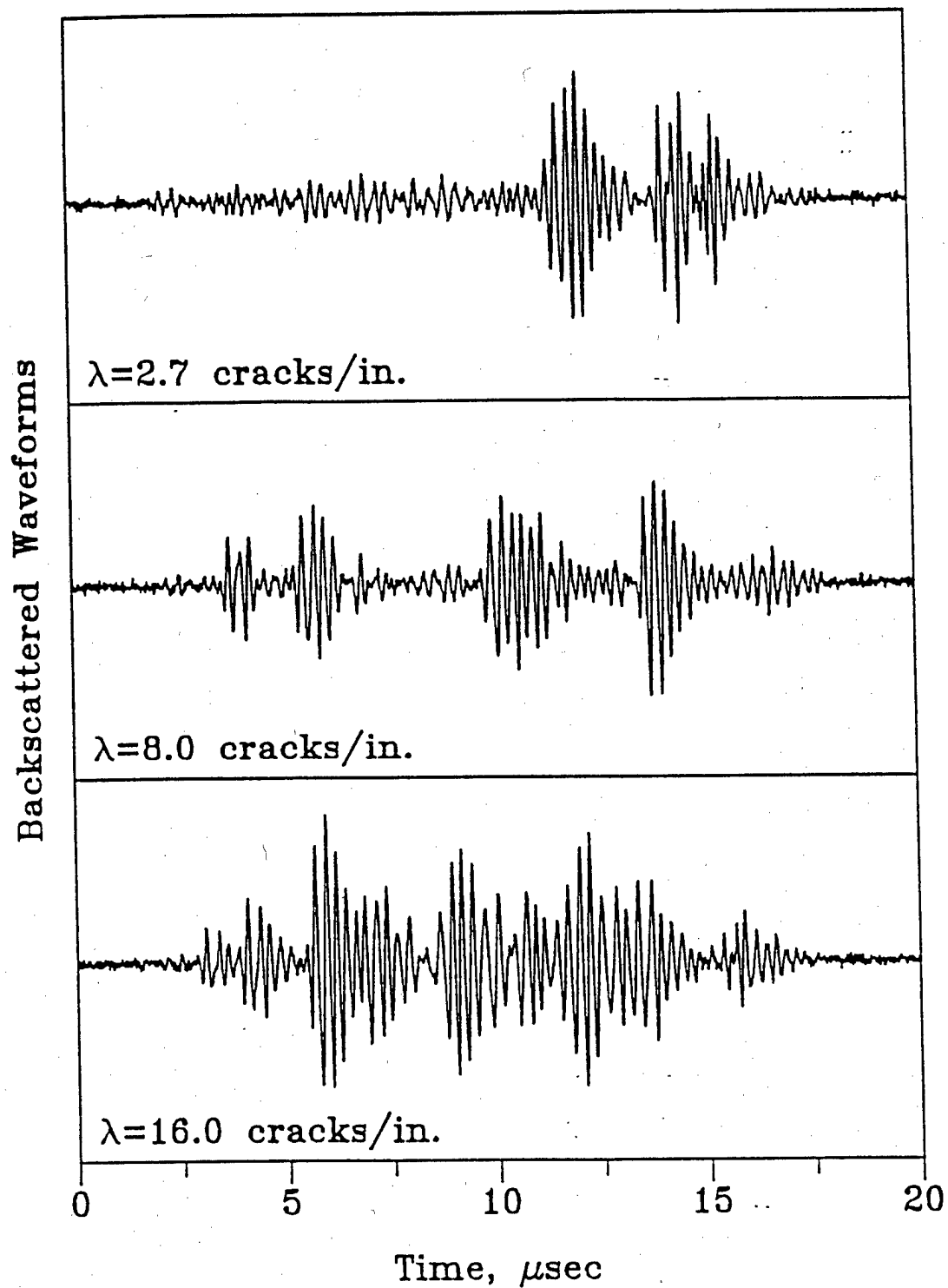


Fig. 4 Typical Backscattered Signals from Matrix Cracks for Various Crack Densities in Crossply Composite Laminates.

block its propagation to the inner layer where matrix cracks exist. As a result, the backscattered energy returned to the transducer is reduced.

If the contact condition between the transducer and specimen changes during loading, it is not possible to calibrate the instrument for crack density measurement. Therefore, it is necessary to verify the contact condition. This was done by a series of loading, unloading, and reloading tests. During loading, the signal was monitored and when a change was observed, the specimen was immediately unloaded at the same rate. Then, it was reloaded above the previous stress level. This procedure was repeated up to failure.

Figure 5 shows nine loops of loading and unloading stress-strain curves up to failure. Several typical curves of backscattered energy as a function of strain are shown in Figs. 6 through 8. There was no change in the backscattered energy in the first loop and the loading part of the second loop. As soon as the cracks developed, there was a sudden increase in backscattered energy as shown in Fig. 6. During unloading, the backscattered energy increases slightly. In loop 3 (not shown), the specimen was reloaded above the previous level but below the level that would cause further matrix cracking. It was observed in this loop that the backscattered energy curve for unloading followed the path of the loading curve. Note that the initial value of the backscattered energy in the reloading part of loop 4 coincides exactly with the last value of the unloading curve in loop 2 as shown in Fig. 7. As in the case of loop 3, loop 5 shows that the backscattered energy curve during unloading retraces the loading curve as there is no further cracking (Fig. 8).

Proper selection of the couplant is important because it must provide not only good contact between the transducer and specimen but also maintain the same contact condition during the entire loading period. Various couplants were tried and it was found that couplants of high viscosity do not dry. However, if the viscosity is too high, the couplant does not provide uniform contact, resulting in poor signals. The best couplant found was honey (Dutch Gold Wildflower Honey) that has an appropriate viscosity and does not dry

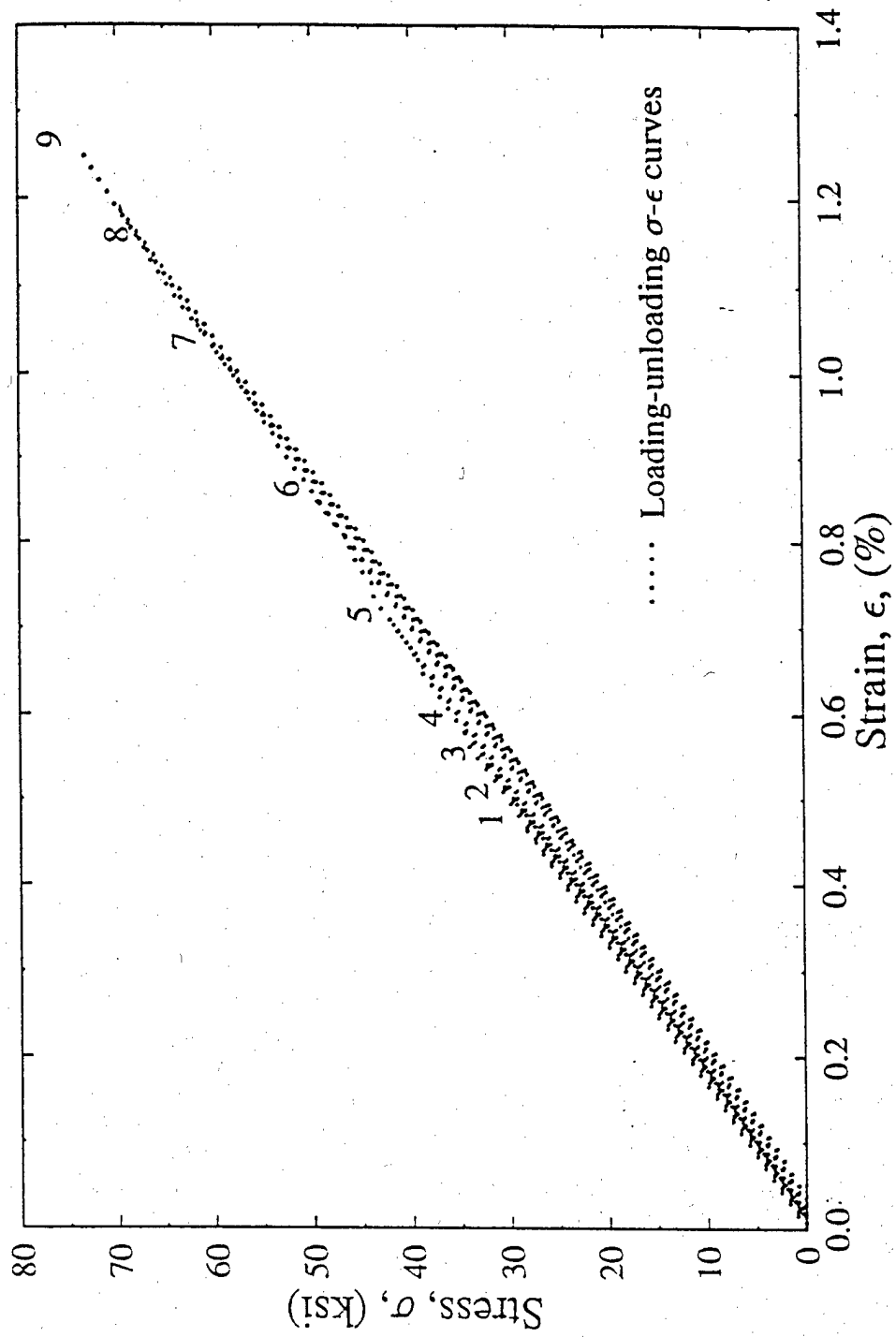


Fig. 5 Loading-Unloading Stress-Strain Curves for $[0/90_4]_s$ IM7/8551-7A Carbon/Epoxy Crossply Laminate.

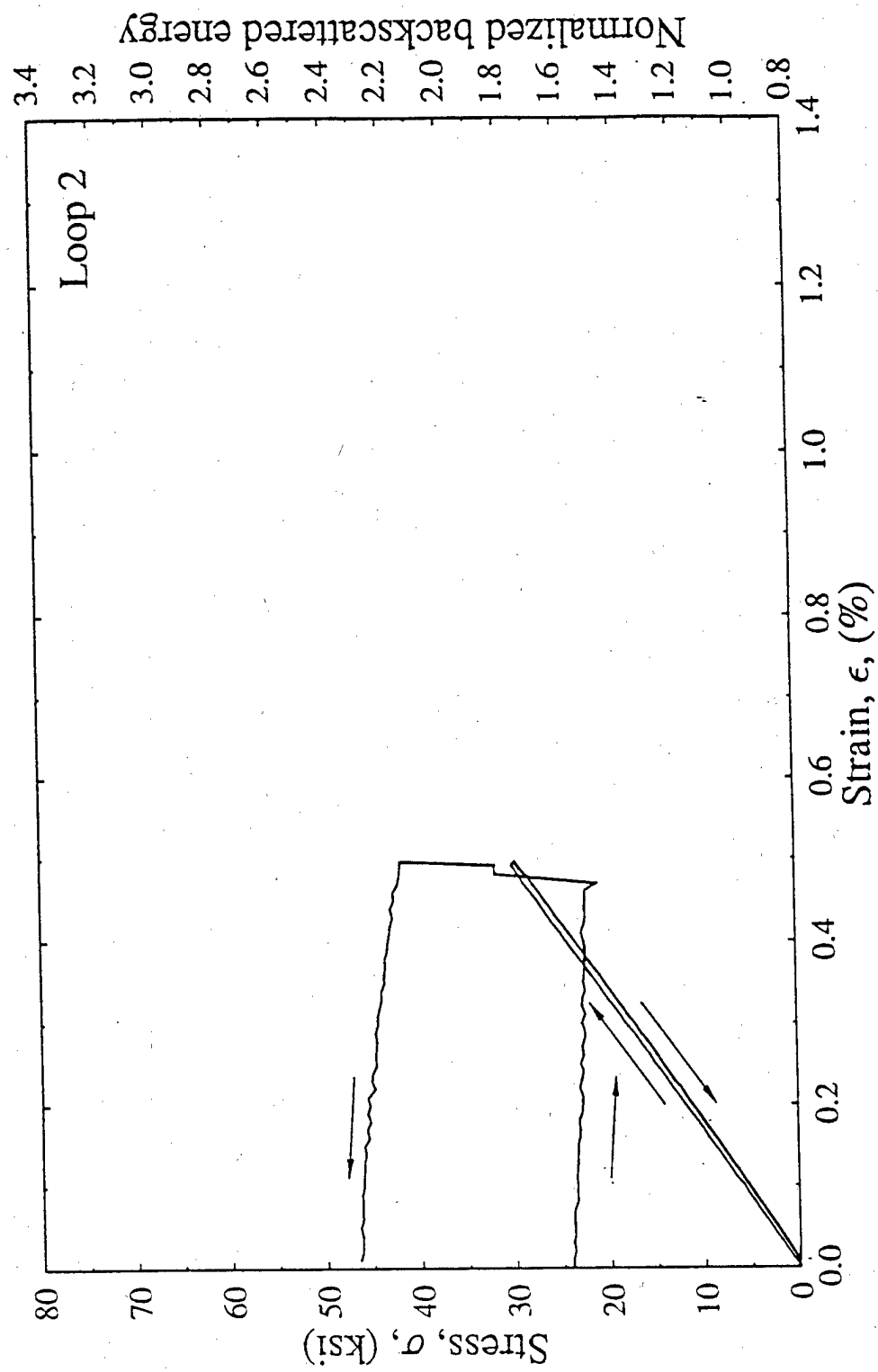


Fig. 6 Stress and Ultrasonic Backscattered Energy versus Strain for Loading and Unloading of $[0/90_4]_s$ IM7/8551-7A Carbon/Epoxy Crossply Laminate (Loop 2).

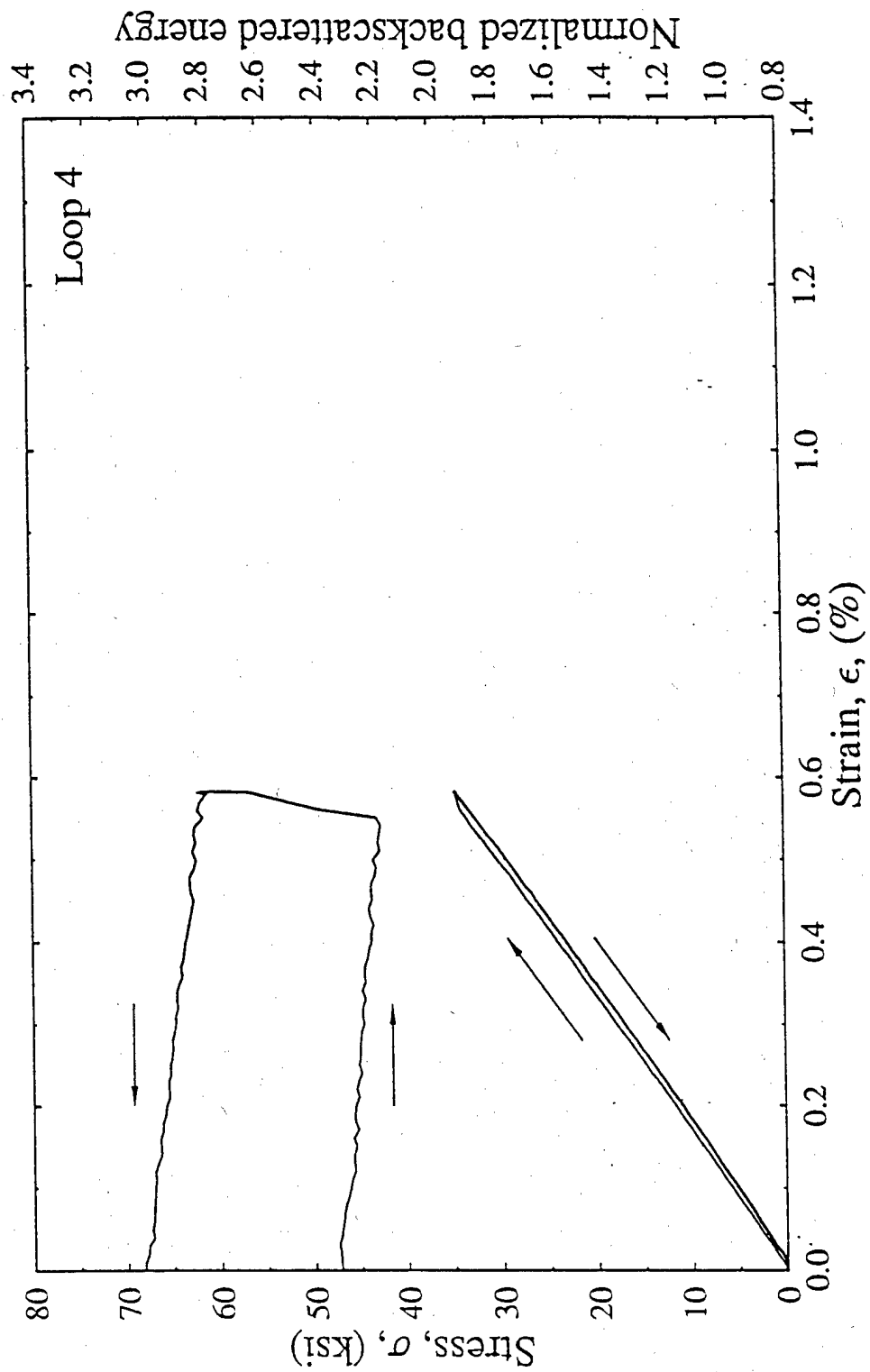


Fig. 7 Stress and Ultrasonic Backscattered Energy versus Strain for Loading and Unloading of $[0/90_4]_s$ IM7/8551-7A Carbon/Epoxy Crossply Laminate (Loop 4).

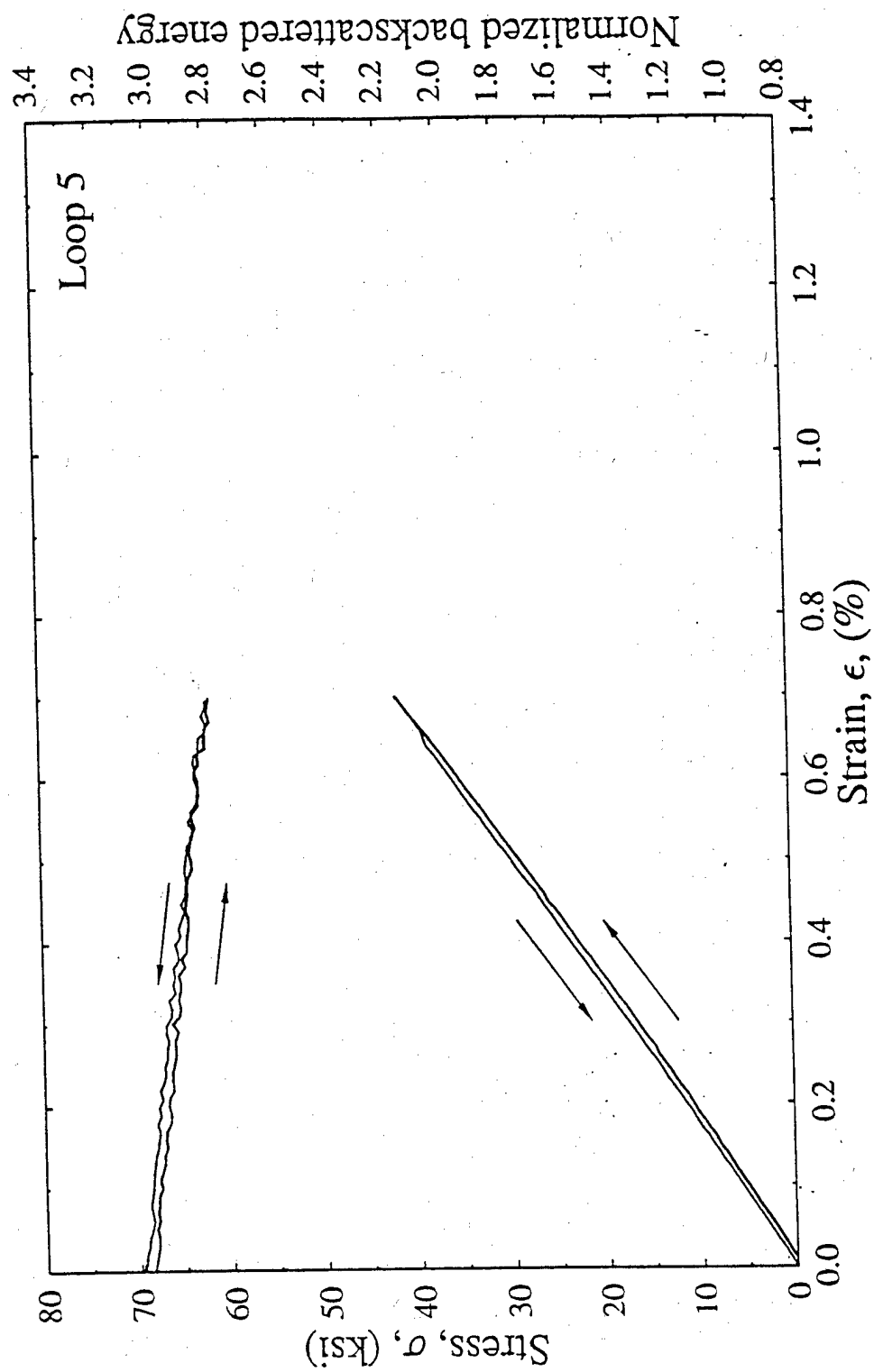


Fig. 8 Stress and Ultrasonic Backscattered Energy versus Strain for Loading and Unloading of $[0/90_4]_s$ IM7/8551-7A Carbon/Epoxy Crossply Laminate (Loop 5).

over time.

It was found from these experiments that the contact condition remains constant during loading. However, it is noted that the backscattered energy increases slightly in the unloading path. It is believed that this phenomenon is primarily due to the reduction in crack opening displacement during unloading. The backscattered energy curve may have to be adjusted to take this phenomenon into consideration.

Besides ultrasonic scattering, acoustic emission output was recorded. First, the amplitude of the AE events was studied. Figure 9 shows a histogram, or the probability density function (PDF), of AE events as a function of amplitude during the entire monotonic loading period. The distribution of the histogram is bimodal. This means that there are numerous signals of low amplitude as well as high amplitude but relatively fewer of medium amplitude. This histogram representation, however, gives no correlation of AE events with failure mechanisms.

The histogram was then plotted as a function of both amplitude and applied strain in the form of the three-dimensional plot shown in Fig. 10. This plot should be interpreted in connection with the corresponding stress-strain curve (Fig. 2). In the range of strains between points B and C where matrix cracking is predominant, there is a large number of AE events of amplitude between 85-90 dB (the peaks in the front of the plot). This leads to a conclusion that the highest amplitude AE signals correspond to matrix cracking. As the strain increases, there are numerous low amplitude signals (between 45 to 55 dB). These signals appear after most of the transverse matrix cracking is finished so that it is believed that they are due to frictional noise at the cracks and other damage. Also noted is a high amplitude peak at a high strain near ultimate failure of the material, that is, at the stage of fiber bundle fractures. Fiber fractures generate AE signals of amplitude as high as that of matrix cracking.

The frequency distribution of the AE signal is another useful parameter. The frequency content should be obtained from the AE signal by Fourier analysis. However,

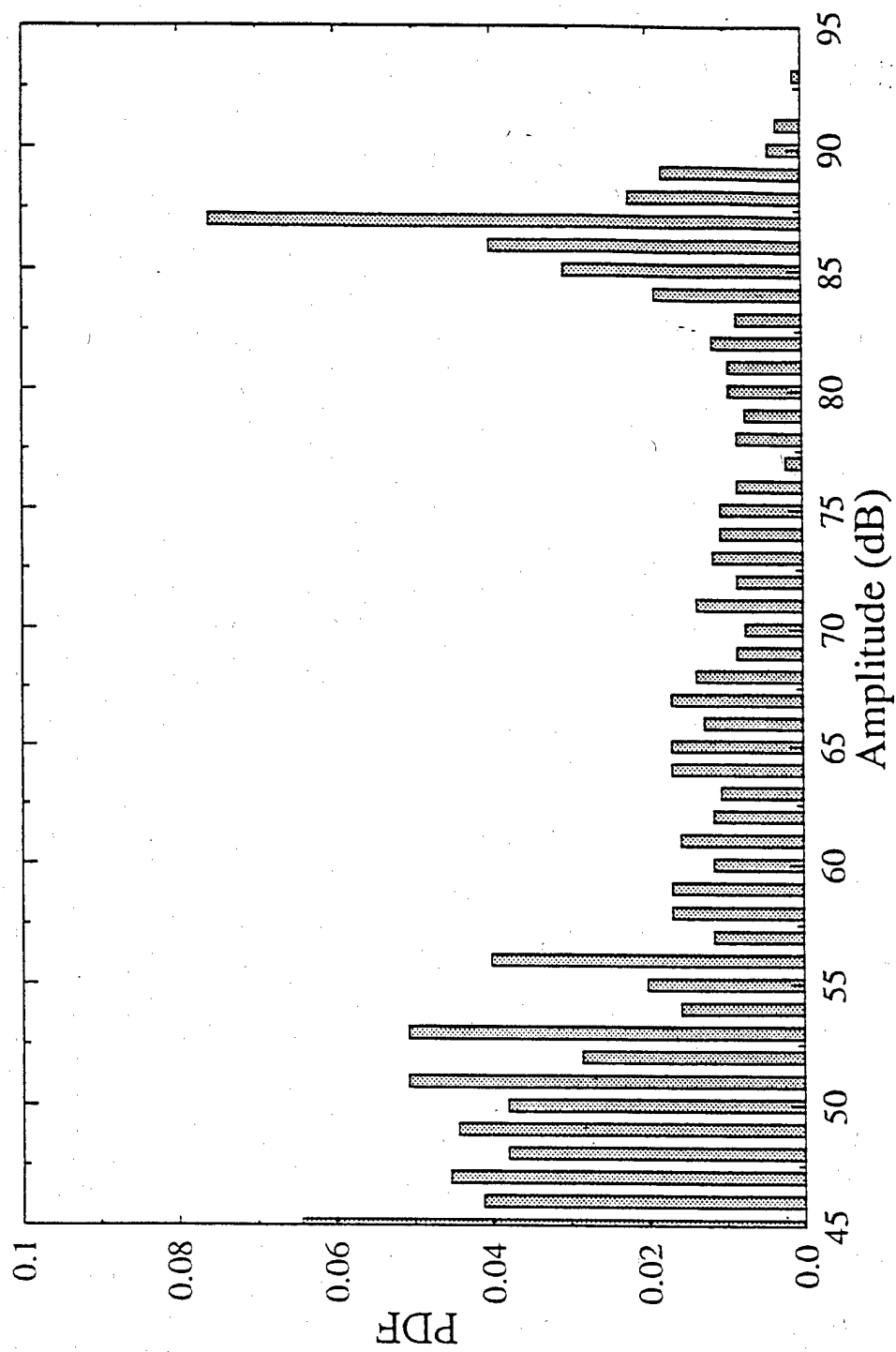


Fig. 9 Histogram of AE Events as a Function of Amplitude for [0/90₄]_s IM7/8551-7A Carbon/Epoxy Laminate.

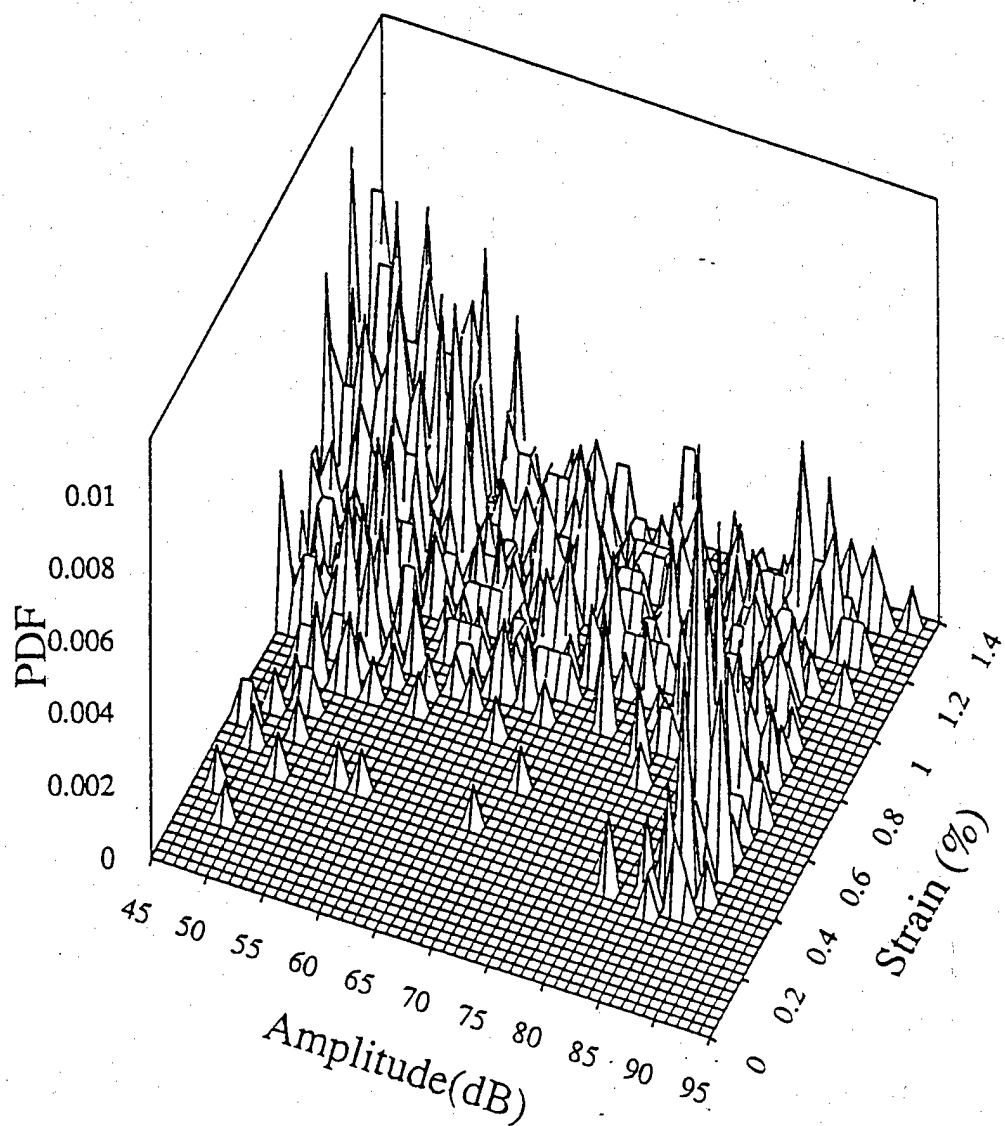


Fig. 10 Distribution of AE Events as a Function of Strain and Amplitude for $[0/90_4]_s$ IM7/8551-7A Carbon/Epoxy Laminate.

for convenience, the number of counts per event (count frequency), which represents approximately the frequency of the signal, was used in this study. Figure 11 shows a three-dimensional plot of the distribution of AE events as a function of strain and count frequency. Most of the low frequency signals are due to noise which resides in the strain range between 0.7 to 1.3%. Several peaks are found in the matrix cracking region, or the count/event range of 80-160. Also noted is a small peak near global failure corresponding to failure of fiber bundles. From these observations, it is concluded that the signals from matrix cracking and fiber bundle fractures are high in amplitude and frequency.

AE was monitored continuously during loading/unloading tests. Figure 12 shows the stress and cumulative AE counts as a function of applied strain. The envelope of the cumulative AE counts shows the rate of AE output. In the linear stress-strain range below 0.4% strain, no AE events were produced. The slope of the envelope is the highest in the matrix cracking region and decreases at a point beyond cracking stabilization.

The envelope of the loading/unloading stress-strain curves matches the monotonic stress-strain curve. This implies that the loading/unloading process produces no significant additional damage in the material. During reloading very few additional AE events were detected. This confirms the Kaiser effect for this material.

2.4 Summary and Conclusions

Matrix cracking was correlated with the associated ultrasonic backscattered energy and acoustic emission output. The stiffness degradation of the material due to matrix cracking can be correlated with ultrasonic measurements. Both types of measurement gave consistent results.

Ultrasonic backscattered energy was constant in the linear region of the stress-strain curve. In this region no acoustic emission events were detected.

In the matrix cracking region, matrix crack density increases quickly and the backscattered energy increases sharply in steps corresponding to stiffness degradation. In

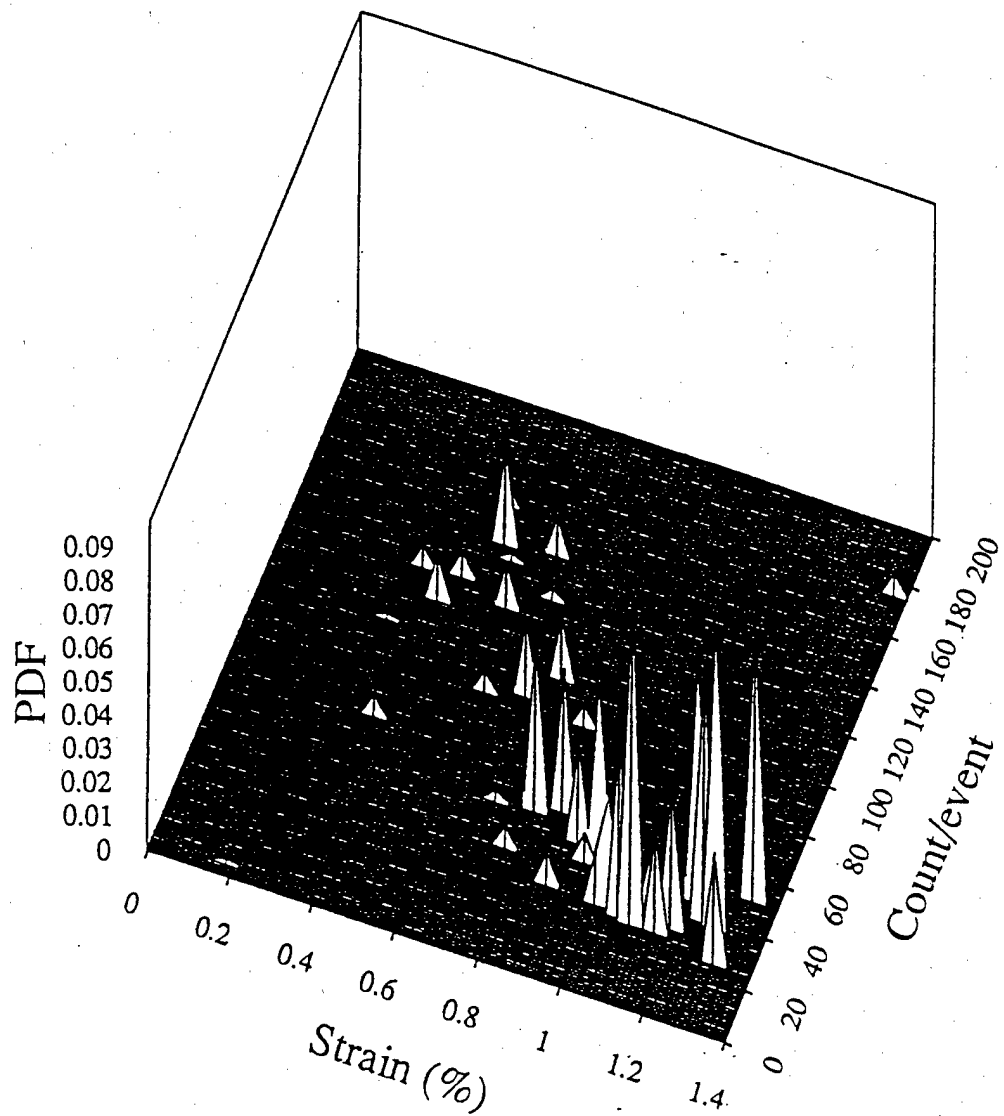


Fig. 11 Distribution of AE Events as a Function of Strain and Count Frequency for $[0/90_4]_s$ IM7/8551-7A Carbon/Epoxy Laminate.

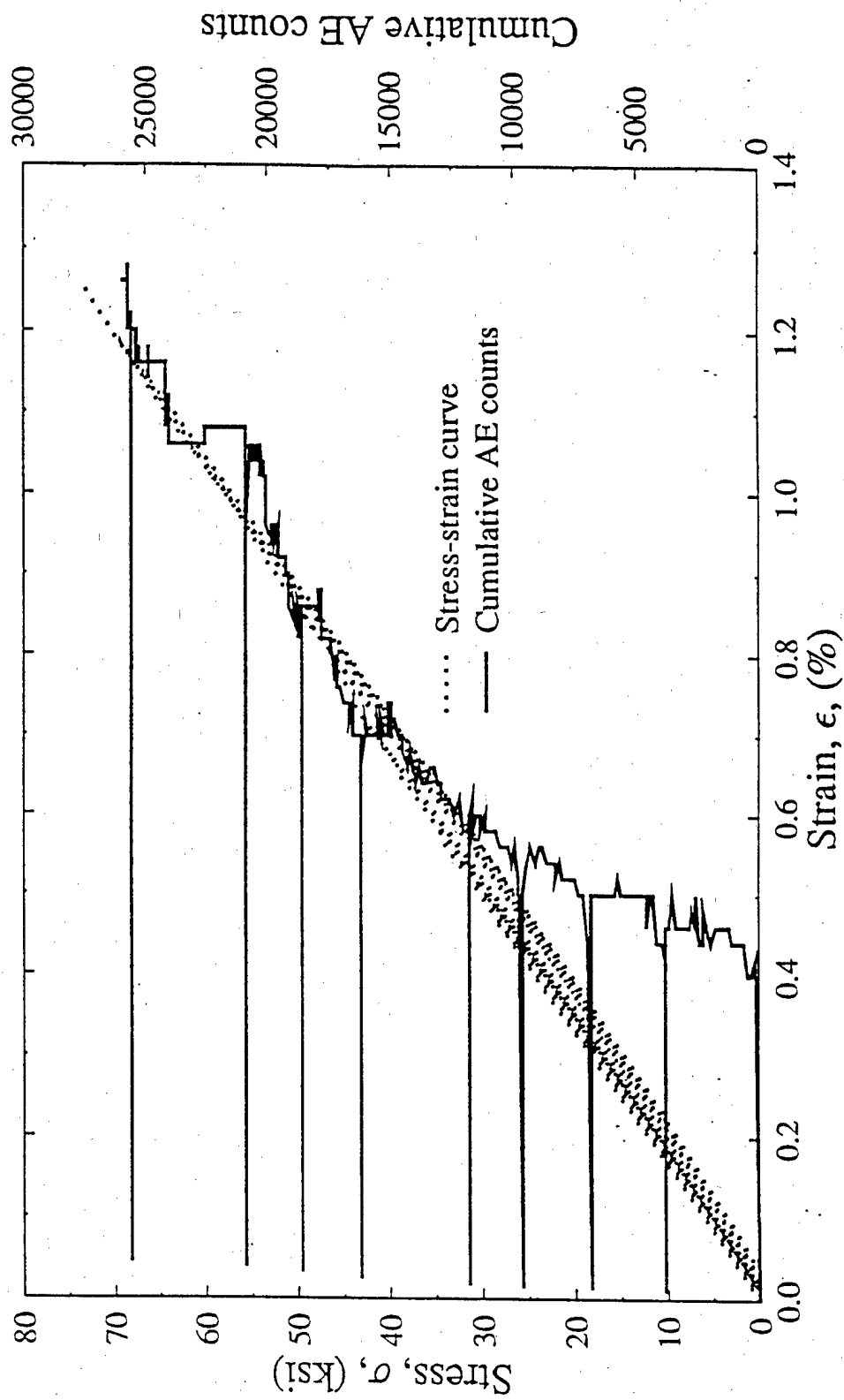


Fig. 12 Stress and Cumulative Counts versus Strain for Loading and Unloading of [0/90₄]_s IM7/8551-7A Carbon/Epoxy Laminate.

this region, numerous AE signals of high amplitude and high frequency are detected.

As the cracking and stiffness are stabilized, the backscattered energy is stabilized or starts decreasing whereas the stress-strain behavior becomes linear. High amplitude acoustic emission signals are reduced in this region but numerous AE signals of low amplitude and low frequency are produced. Isolated high amplitude AE signals are noticed in the last part of the stress-strain curve, possibly associated with other failure mechanisms.

A series of loading and unloading tests were conducted. Both backscattered energy and AE measurements during loading/unloading tests showed that no additional damage occurs upon reloading up to the previous peak loading, thus, confirming the Kaiser effect.

3. EVALUATION OF COMPOSITE REPAIR OF A CRACKED METALLIC SUBSTRATE

3.1 Introduction

Extension of the structural life of aging aircraft requires periodic inspections by available NDE techniques and, following detection of damage, retirement or repair of the aircraft. Typical defects detected are fatigue cracks around fastener holes or other regions of stress concentration. Conventional repair methods in use include welding, stop-drilling at the crack tips, and attaching metal reinforcing plates with rivets or bolts. However, these solutions have limitations such as stress concentrations, limited fatigue life, and limited corrosion resistance.

Composite materials offer many advantages over conventional materials in structural reinforcement and repair of aging aircraft. Composite repair patches are usually boron/epoxy or carbon/epoxy laminates adhesively bonded to the aluminum substrate where damage, such as fatigue or stress corrosion cracking, exists or is anticipated. Such patches are thin and lightweight, conform to curved surfaces and have high directional strength and stiffness. They can be installed relatively easily without causing damage to the existing structure and they do not cause any problems with fretting, corrosion, undesirable structural changes or balance.

Earlier studies on composite repairs were done by Baker et al. [11-13] and Ong and Shen [14]. A comprehensive study including analytical and experimental work was given by Atluri et al [15]. More recent studies, both analytical and experimental, have been reported by Aglan [16-18], Sun [19] and Minnetyan and Chamis [20]. Whereas the effectiveness and airworthiness of composite repairs have been demonstrated, further demonstration of their reliability and predictability is demanded. The main unresolved problem is a reliable prediction of bond strength and fatigue life based on nondestructive measurements during service. Evaluation and development of nondestructive techniques is needed for assessment of quality and reliability of composite repair patches.

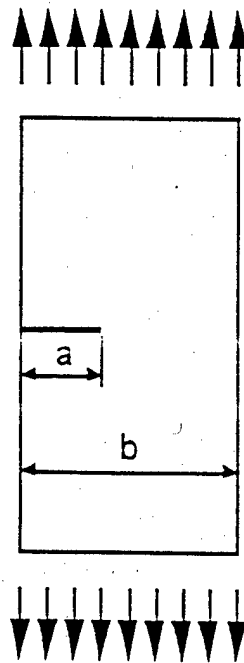
The objective of this task was to investigate the fatigue behavior of cracked aluminum panels repaired with carbon/epoxy patches. Experiments were performed to study and predict the debonding and failure of the adhesive bond and crack growth in the aluminum substrate. Ultrasonic C-scanning was used to monitor debond and/or crack growth at intervals during fatigue testing.

3.2 Experimental Procedure

Four types of specimens were prepared using 2024-T3 aluminum substrate and carbon/epoxy patches. The aluminum panels were 3.18 mm (0.125 in.) thick, 51 mm (2.0 in.) wide and 229 mm (9.0 in.) long. The first two types of specimens were used to study crack repairing and had edge and central cracks in the aluminum (Fig. 13). Edge cracks were made by sawing a 9 mm (0.35 in.) notch at the edge of the aluminum panel. For the center notches, a 6.4 mm (0.25 in.) diameter hole was drilled at the center and then two 1.6 mm (0.063 in.) long notches were sawed from the hole boundary along the horizontal axis. Then, the specimens were prefatigued to initiate crack growth. For crack initiation, or precracking, a cyclic stress of 69 MPa (10 ksi) with a stress ratio of $R = 0.1$ was applied at a frequency of 3 Hz. The precrack load was kept low so that the precrack stress intensity factor was lower than the K_{max} of the subsequent test, i.e., $K_{precrack} < K_{max}$.

SPECIMENS

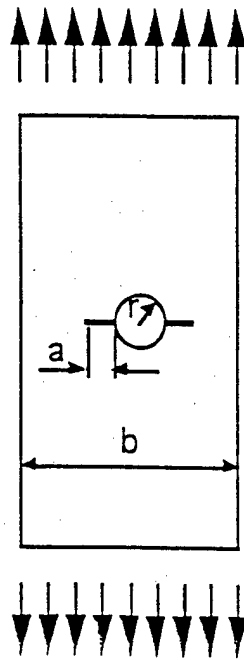
Single-Edge Crack



$$\Delta\sigma = \sigma_{max} - \sigma_{min}$$

$$\Delta K \cong 1.12\Delta\sigma\sqrt{\pi a}$$

Central Hole with Cracks



$$\Delta\sigma = \sigma_{max} - \sigma_{min}$$

$$\Delta K \cong c\Delta\sigma\sqrt{\pi(a+r)}$$

$$c = 1 + 0.256\left(\frac{a}{b}\right) - 1.152\left(\frac{a}{b}\right)^2 + 12.2\left(\frac{a}{b}\right)^3$$

Fig. 13 Aluminum Specimens with Edge and Central Cracks.

The surface of the specimen that would not be covered by the patch was well polished to show clearly the crack extension in the specimen. The crack length extension was measured by a small high magnification camera (GP-MS112, Panasonic). A TARGA M8 (Truevision Inc.) board was used to capture the images. In the specimen a known reference length was marked and the crack length was measured by comparing it with the reference length.

The composite repair patches were 50.8 x 50.8 x 0.91 mm (2 x 2 x 0.036 in.) $[0_3 / \overline{90}]_s$ carbon/epoxy laminates (IM7/8551-7A). The composite patches were bonded to the aluminum panels with FM-73 film adhesive (CYTEK). The aluminum panels and the composite patches underwent surface treatments before being bonded. All surfaces were cleaned with a solvent, methyl ethyl ketone (MEK). Then, the surfaces to be bonded, on both the aluminum and the composite, were abraded with Scotch-Brite pads and de-ionized water. The aluminum also underwent a surface treatment with a silane coupling agent. A 1% aqueous solution, which had been hydrolyzed for 1 to 2 hours, was applied to the aluminum with a clean paintbrush. The surface was kept moist for 10 minutes and then air dried [21]. The FM-73 adhesive was placed on the aluminum and the patches were applied. The specimens were then cured at 180° F (82° C) and a pressure of 172 kPa (25 psi) for 8 hours. The specimens were allowed to cool and then received an hour-long postcure of 121° C (250° F) without pressure. A silicone rubber sealant was applied around the edges of the patch and over the cracks to prevent leakage of water into the adhesive during immersion ultrasonic scanning.

The third and fourth type of specimen were used to study the adhesive bond characteristics of the patches. The first of these was a symmetric lap joint made by cutting the aluminum panel in half and then bonding composite patches on either side. The patches were bonded with the 0° fibers oriented normally to the joint for maximum stiffness. A 2 mm (0.08 in.) wide and 0.051 mm (0.002 in.) thick strip of Teflon was placed over the joint between the adhesive film and the aluminum surface in order to create an initial

debonded area. The fourth type of specimen had only one patch bonded on one side and, thus, it was an asymmetric lap joint. The geometries of a single edge cracked and a single lap joint specimen with composite patches are illustrated in Fig. 14.

All specimens were subjected to tension-tension fatigue loading in an Instron servohydraulic testing machine with a stress amplitude of 69 MPa (10 ksi), a frequency of 3 Hz and a stress ratio of $R = 0.1$. In the cracked specimens, crack length was monitored optically and also by means of ultrasonic scanning. In the adhesive bond tests, ultrasonic C-scans were performed at various intervals of the fatigue test.

3.3 Results and Discussion

3.3.1 Fatigue Behavior of Patched Panels with Cracks

Figures 15 and 16 show fatigue crack growth of unpatched aluminum specimens with edge and center cracks, respectively. The crack growth rate, da/dN , was calculated from these curves by regression analysis as follows:

Assuming a crack length \bar{a}_i at cycle N_i

$$\bar{a}_i = k_0 + k_1 \frac{(N_i - C_1)}{C_2} + k_2 \frac{(N_i - C_1)^2}{C_2^2}$$

where

$$-1 \leq \frac{(N_i - C_1)}{C_2} \leq 1$$

k_0 , k_1 and k_2 are regression parameters
and

$$C_1 = \frac{(N_{i-n} + N_{i+n})}{2}, \quad C_2 = \frac{(N_{i+n} - N_{i-n})}{2}$$

are scaling parameters.

The crack growth rate at cycle N_i is expressed as

Specimen Geometry

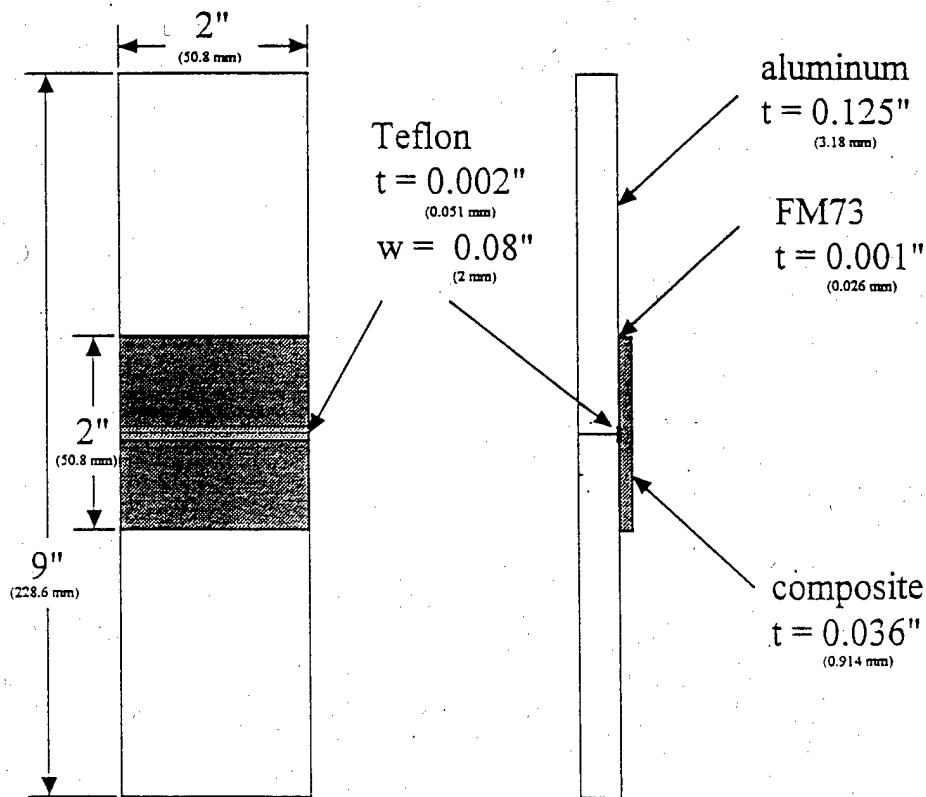
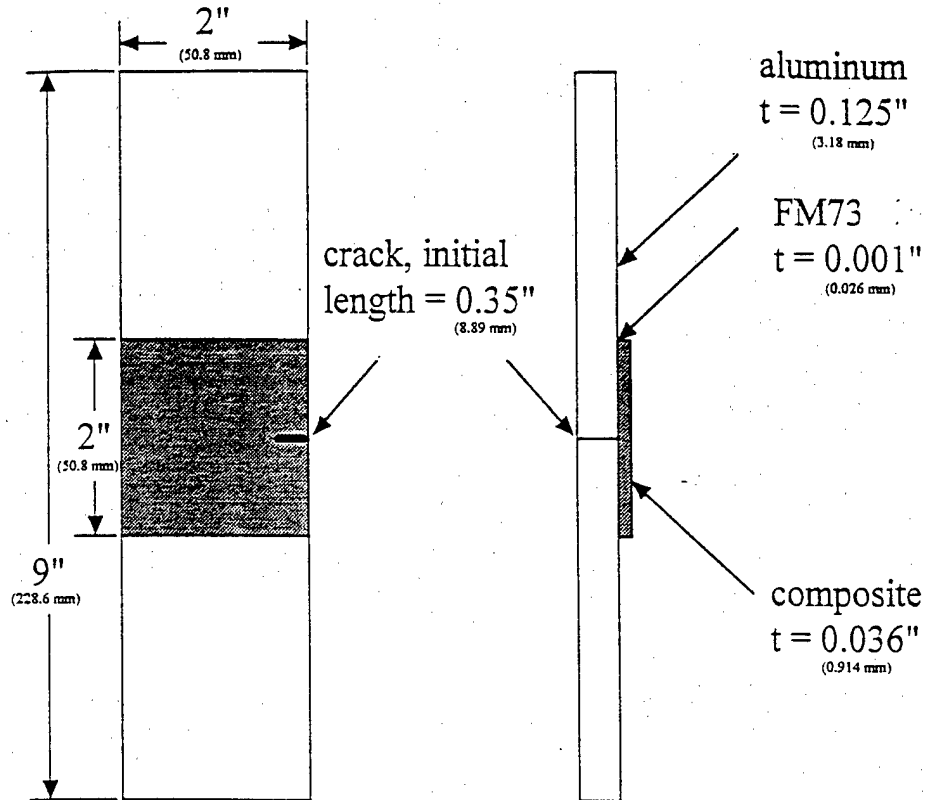


Fig. 14 Edge-Cracked and Single Lap Joint Specimens with Composite Patches.

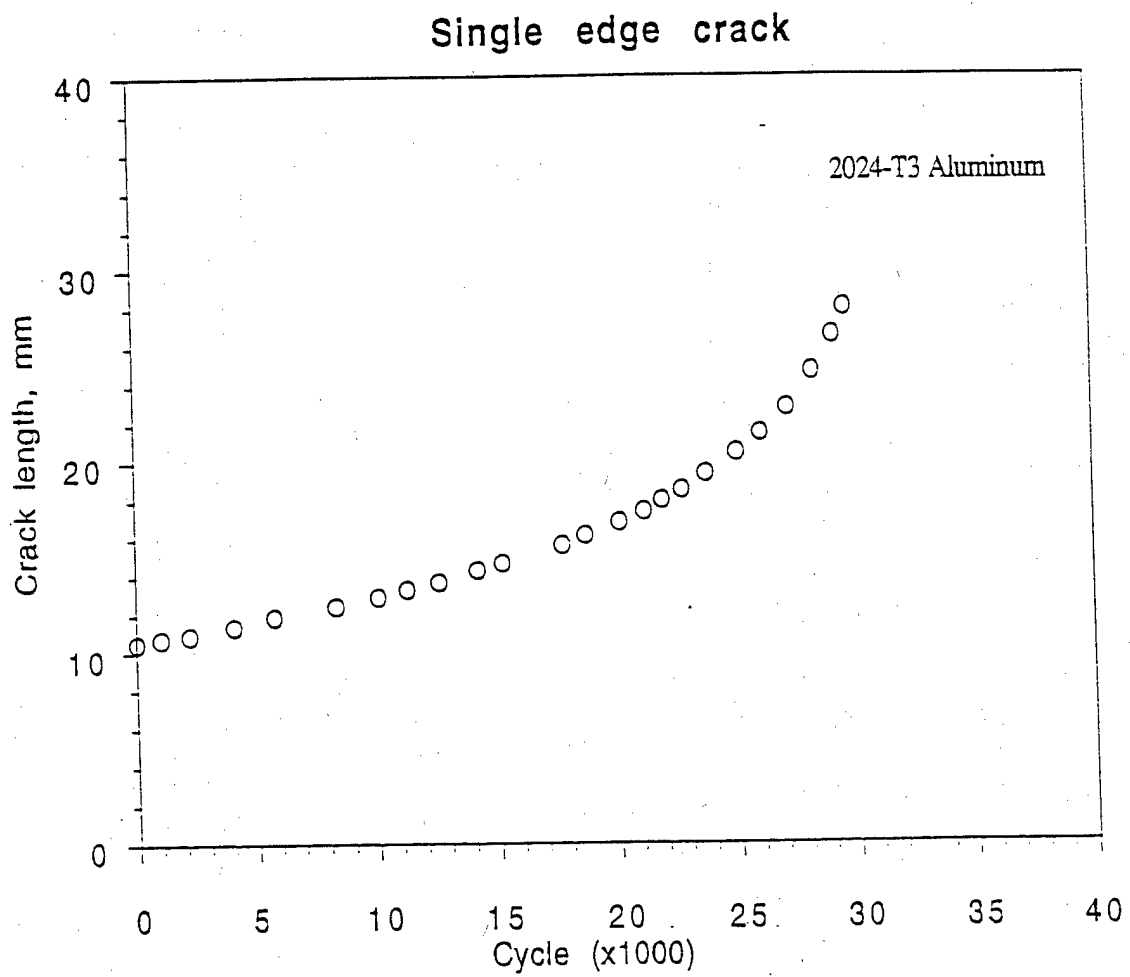


Fig. 15 Crack Growth as a Function of Fatigue Cycles for Unpatched Aluminum Specimen.

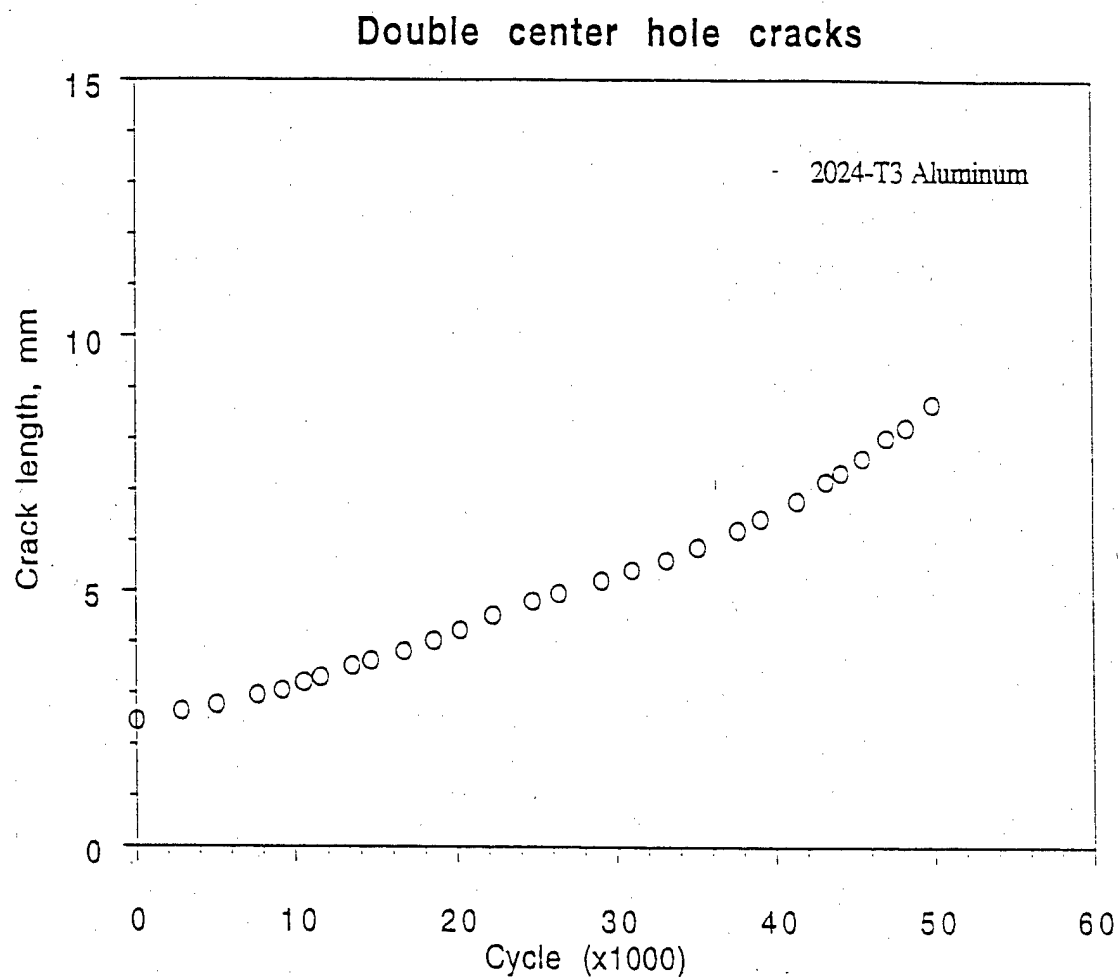


Fig. 16 Crack Growth as a Function of Fatigue Cycles for Unpatched Aluminum Specimen.

$$(da/dN)_{a_i} = \frac{k_1}{C_2} + 2k_2 \frac{(N_i - C_1)}{C_2^2}$$

The stress intensity factor ranges for the two types of specimens were calculated as (Fig. 13)

$$\Delta K \approx 1.12 \Delta \sigma \sqrt{\pi a}$$

for the edge-cracked specimen, and

$$\Delta K \approx c \Delta \sigma \sqrt{\pi (a+r)}$$

for the center-cracked specimen,

where

$$\Delta \sigma = \sigma_{\max} - \sigma_{\min}$$

$$c = 1 + 0.256 \left(\frac{a}{b} \right) - 1.152 \left(\frac{a}{b} \right)^2 + 12.2 \left(\frac{a}{b} \right)^3$$

Figure 17 shows the variation of crack growth rate, da/dN , with stress intensity factor range ΔK . Results are the same for both specimens. Figure 18 shows the fatigue crack growth in the edge-cracked specimen with a patch compared with that in the unpatched specimen. The retardation of crack growth in the patched specimen is apparent. The effect of patching on crack growth rate is also shown in Fig. 19 where a reduction in crack growth rate is observed in the patched specimen. Similar results are shown for the center-cracked specimen in Fig. 20.

Ultrasonic C-scans of the edge-cracked specimens were taken at various fatigue life intervals as shown in Fig. 21. They show clearly both subsurface crack propagation in the aluminum and patch debonding around the crack. An interesting observation is the shape of the debonded area. It has the shape of a narrow band near the crack front, but it assumes a wedge shape behind the front. This is not in agreement with a numerical

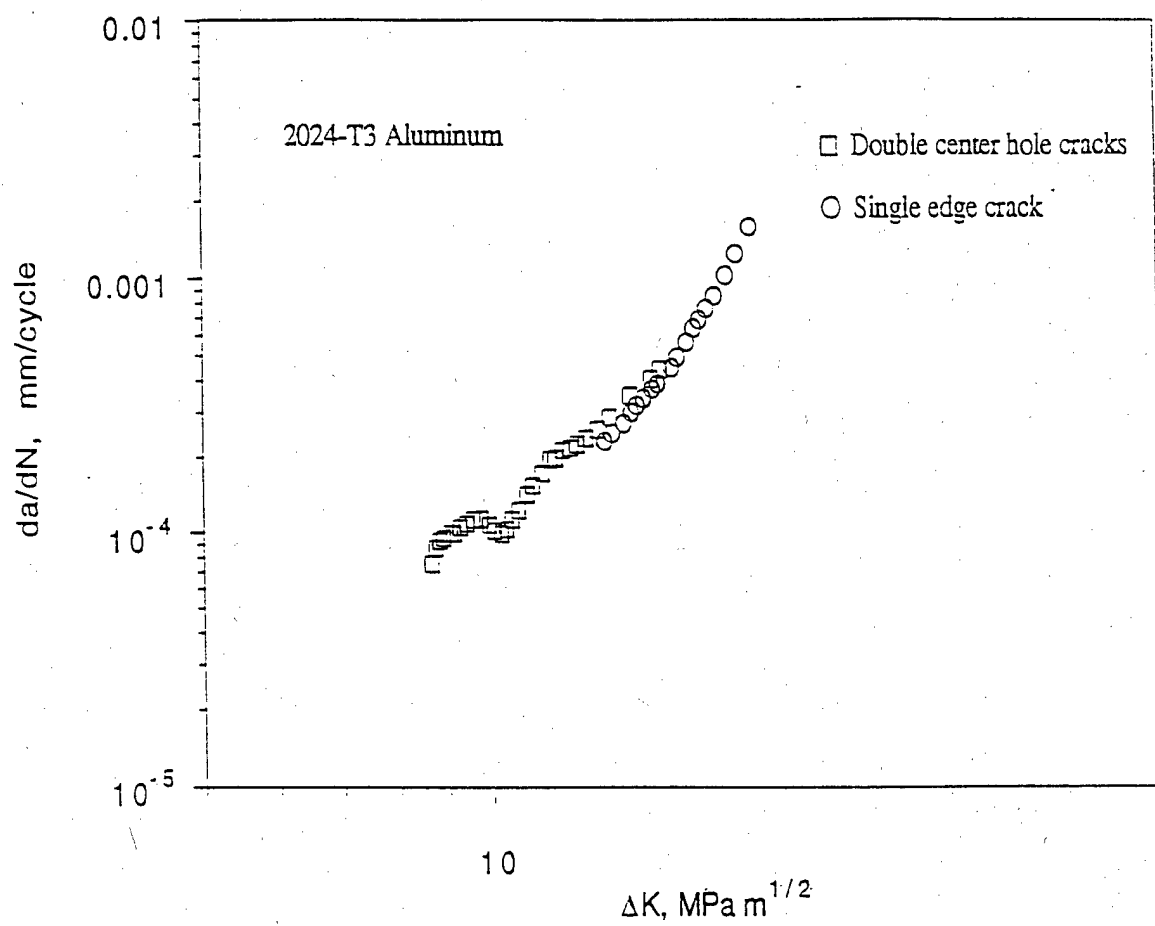


Fig. 17 Crack Growth Rate for Unpatched Aluminum Specimens.

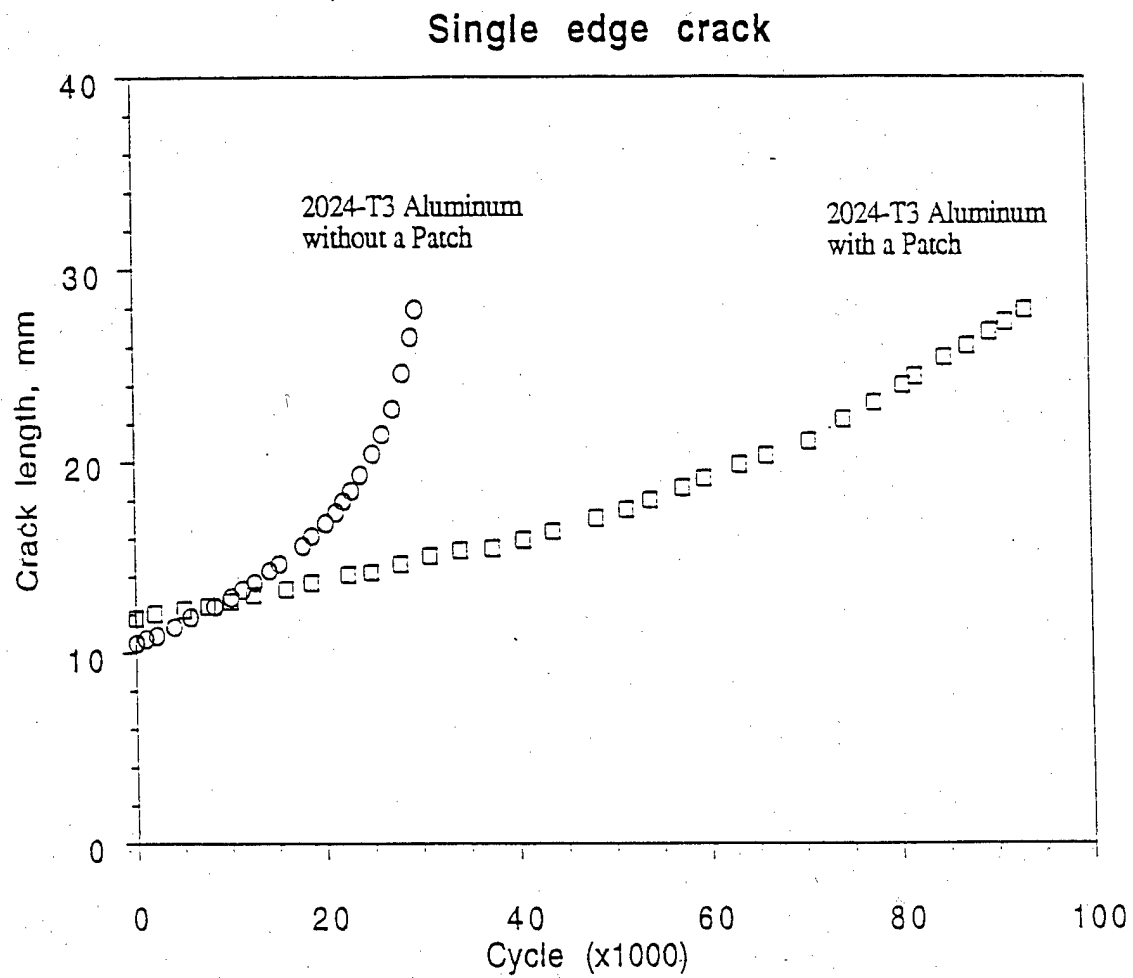


Fig. 18 Crack Length as a Function of Cycles for Patched and Unpatched Specimens.

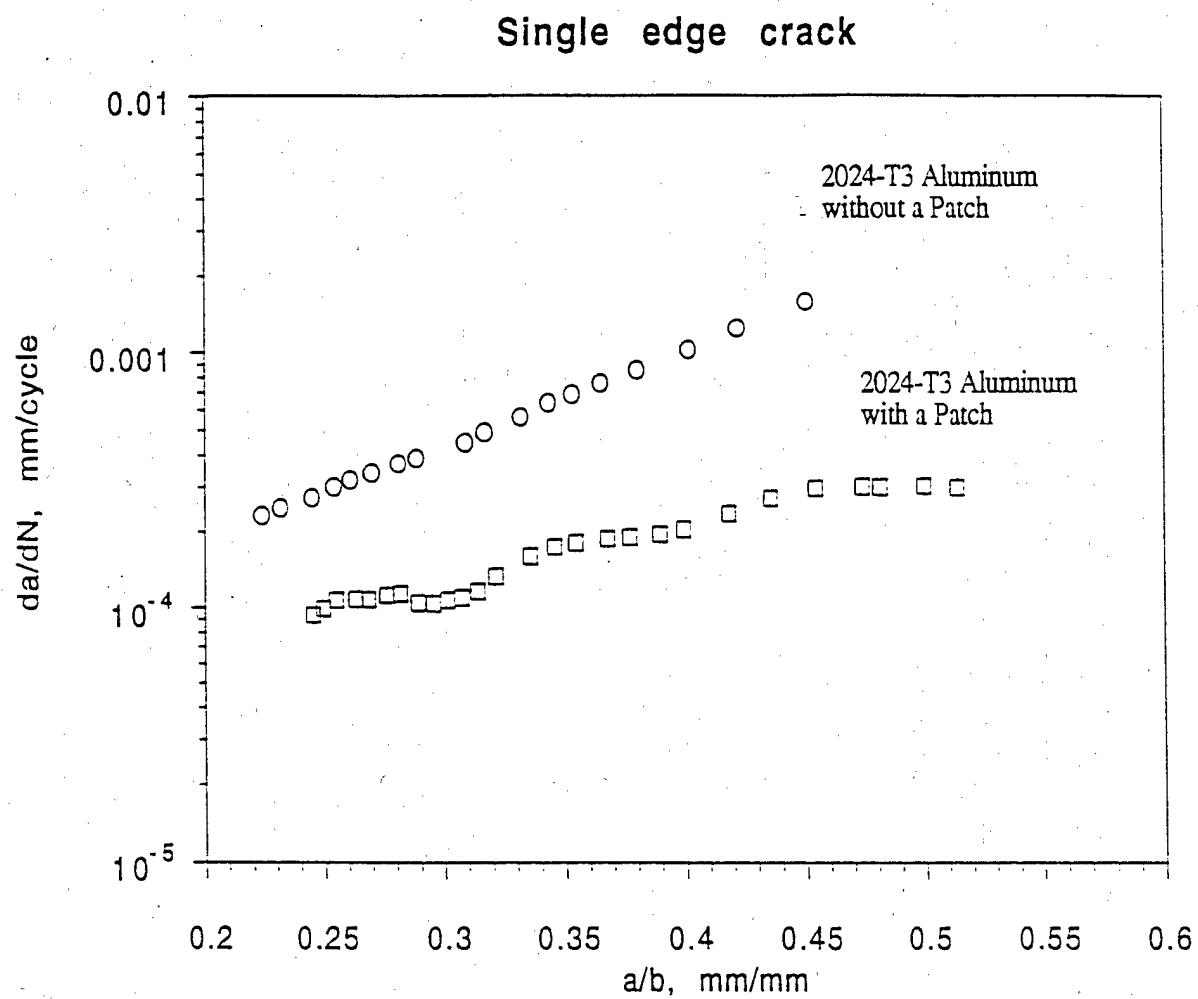


Fig. 19 Crack Growth Rate for Patched and Unpatched Specimens.

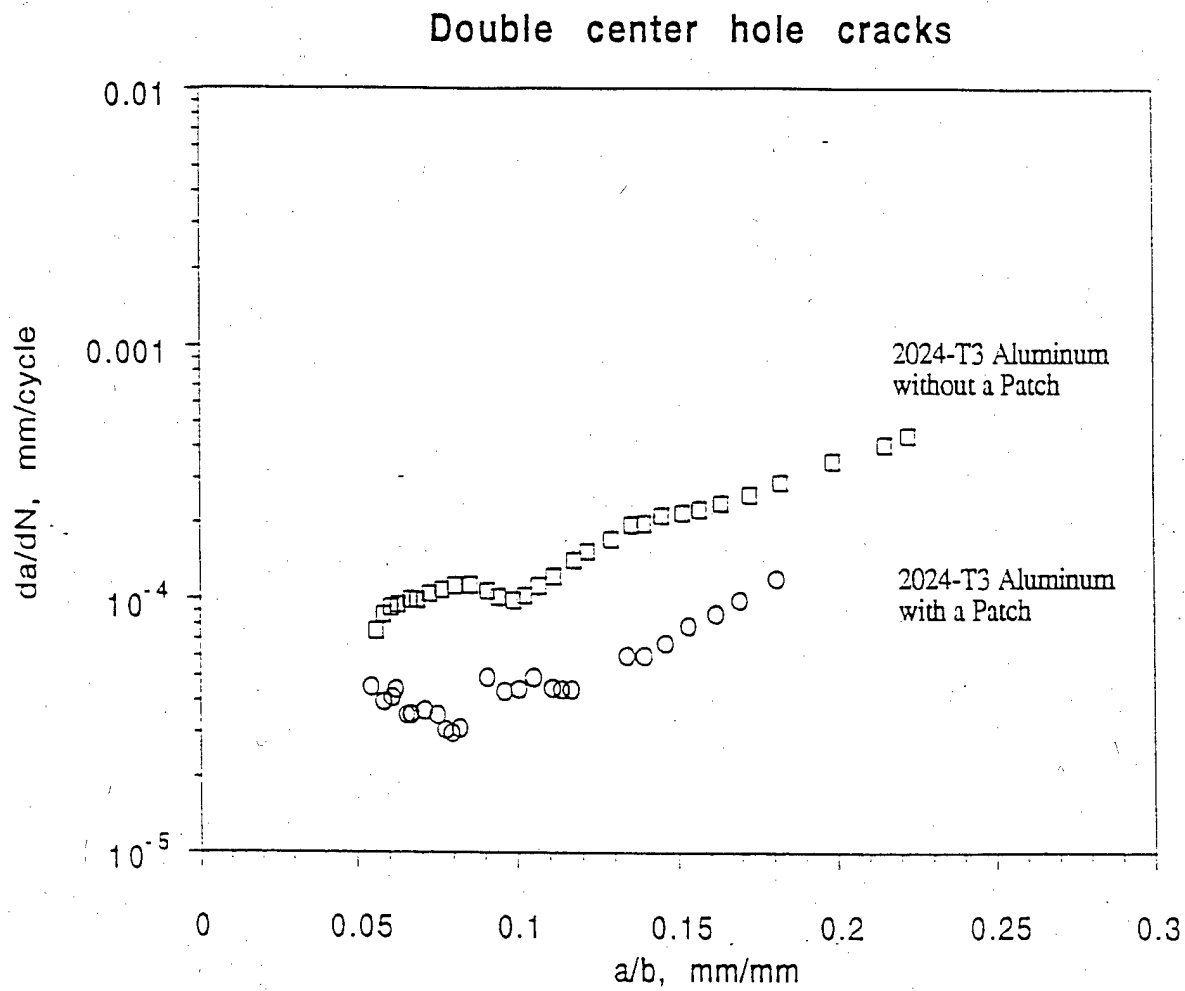


Fig. 20 Crack Growth Rate for Patched and Unpatched Specimens.

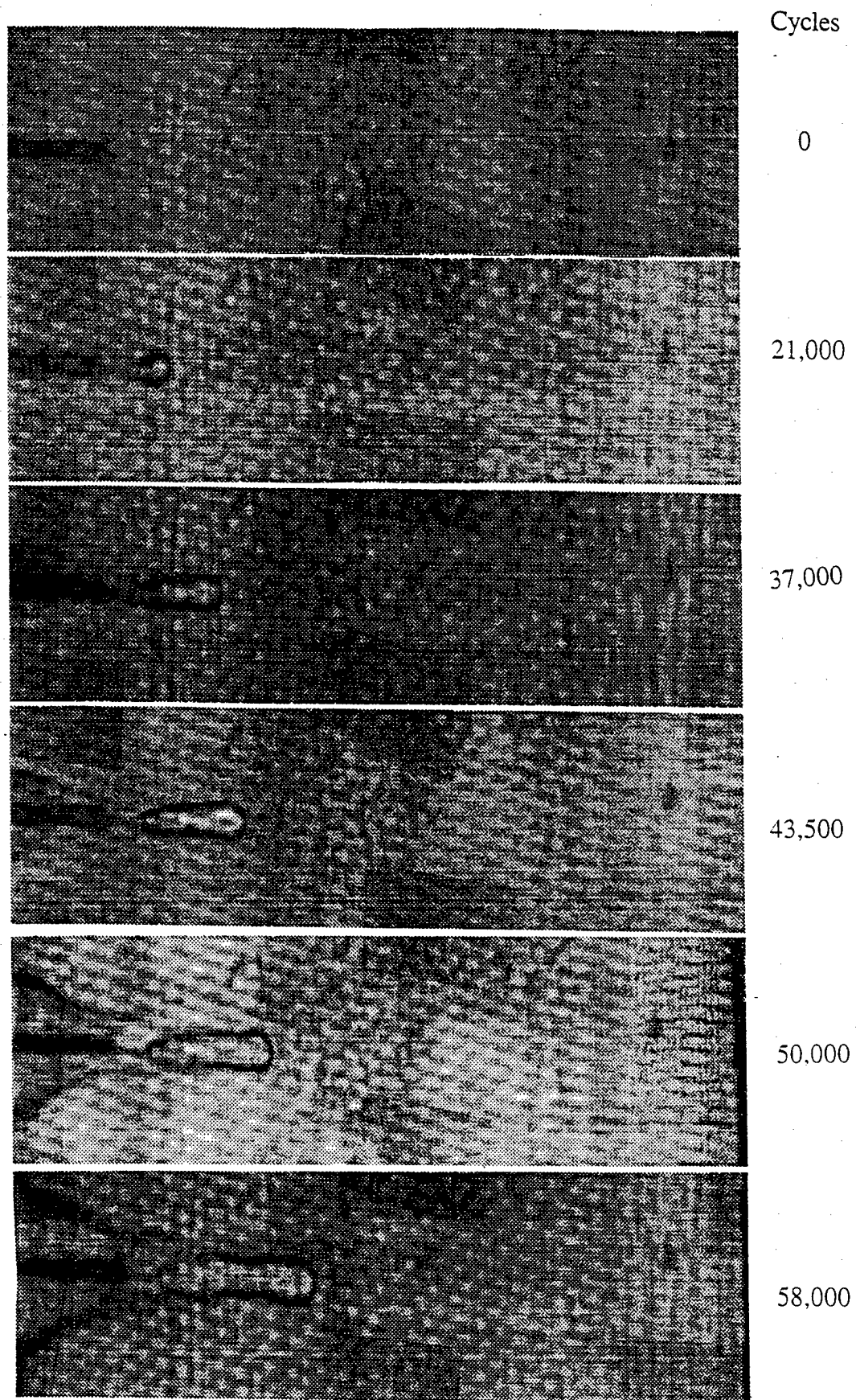


Fig. 21 Ultrasonic C-Scans of Composite Patch in Edge-Cracked Specimen under Fatigue Loading.

analysis which predicts an elliptically shaped debonded zone [19].

The experimental results were introduced into a finite element model representing an edge-cracked specimen. The model was simplified by a two-dimensional representation by assuming that the stresses in the area where the patch remained bonded could be approximated by the rule of mixtures and that the composite patch bridging the debonded area could be modeled by spring elements.

3.3.2 Fatigue of Adhesive Bond

The adhesive bond characteristics of the composite repair patches were studied by means of the second specimen type described in Fig. 14. Fatigue tests were conducted at several cyclic stress amplitudes, 34.5 MPa (5 ksi), 51.8 MPa (7.5 ksi) and 69 MPa (10 ksi). The width of the debonded area, or interface crack length, was monitored by periodic ultrasonic C-scanning as shown in Fig. 22. The crack length (or width of debonded area) was plotted versus fatigue cycles as shown in Fig. 23. From these results plots of da/dN versus σ_{max} and da/dN versus the range of the strain energy release rate ΔG were produced. The latter was approximated using the formula

$$\Delta G = \frac{(\Delta \sigma)^2 E_2 t_2 (t_1 + t_2)}{2E E_1 t_1}$$

where

$$E = \frac{E_1 t_1 + E_2 t_2}{t_1 + t_2}$$

t is the material thickness, E_i is Young's modulus, and subscripts 1 and 2 refer to the aluminum patch, respectively.

The debond growth rate da/dN was plotted versus ΔG to obtain a Paris law type of relationship for debonding under fatigue. A straight line was fitted to the three data points on the $\log (da/dN)$ versus $\log \Delta G$ plot of Fig. 24, yielding a Paris-like relation of the type

$$\frac{da}{dN} = C (\Delta G)^n$$

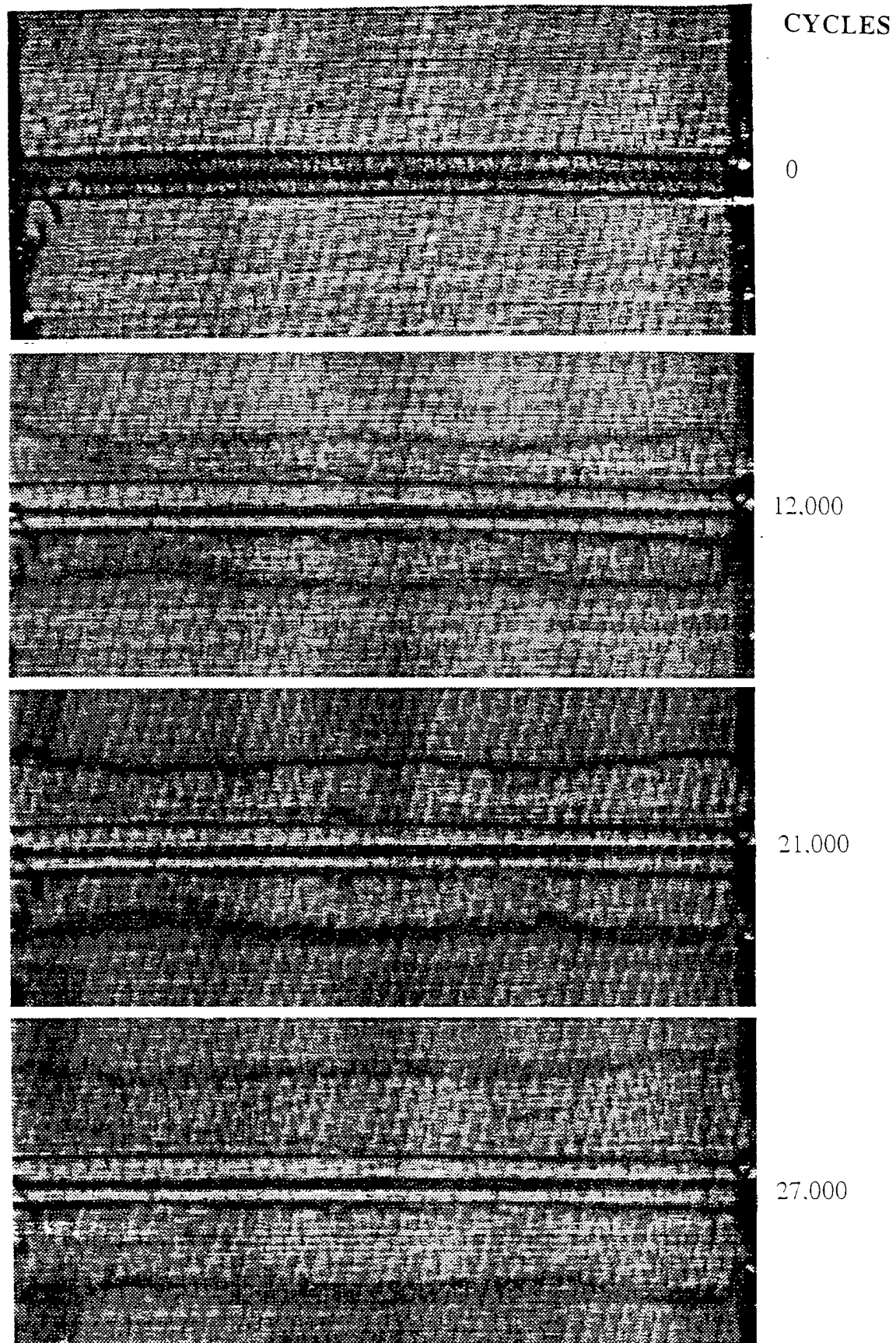


Fig. 22 Debond Growth in Aluminum Lap Joint with Composite Patch (Lap) under Fatigue Loading.

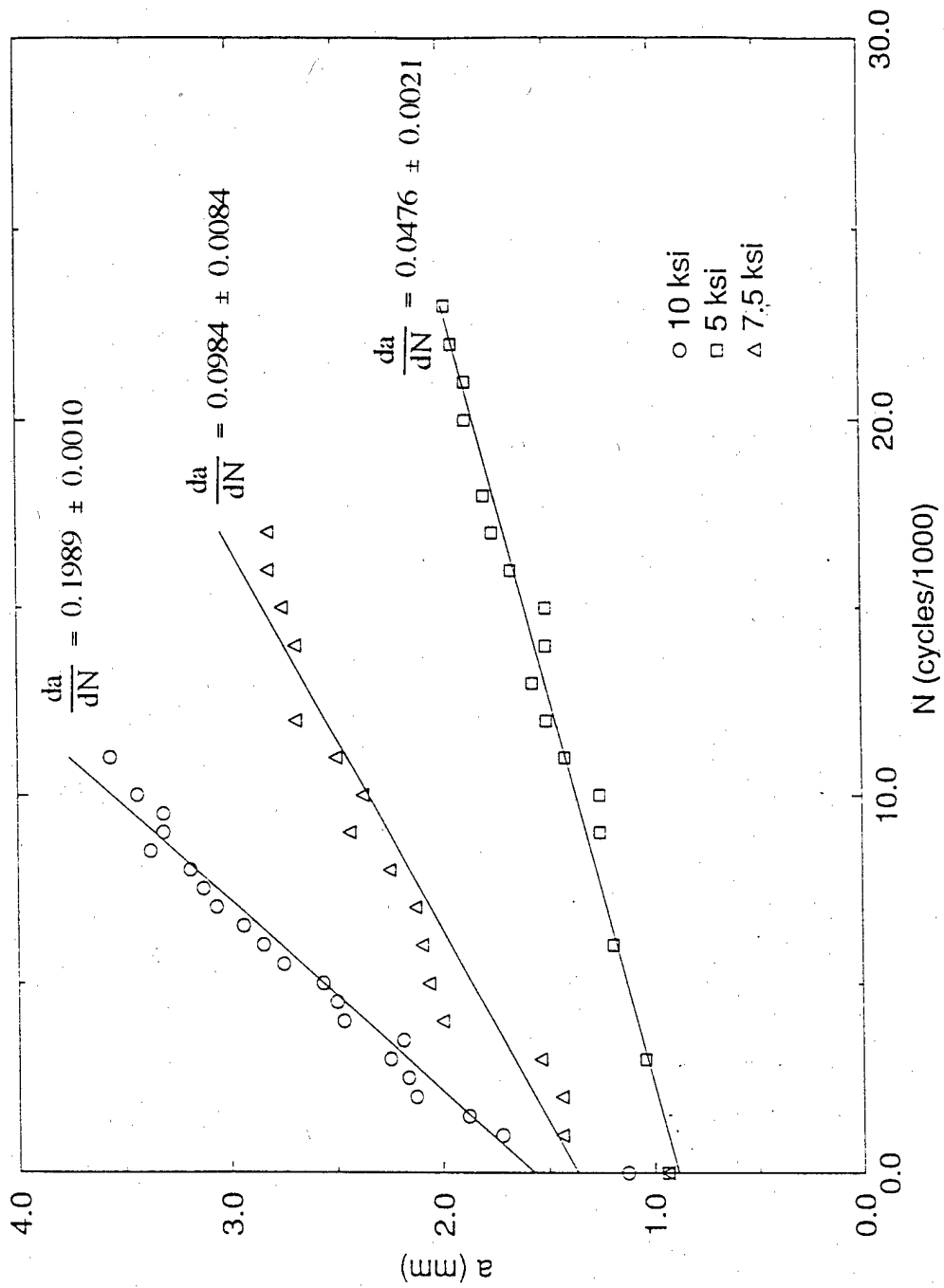


Fig. 23 Debond Crack Growth in Aluminum Single-Lap Joint with Composite Lap under Fatigue Loading.

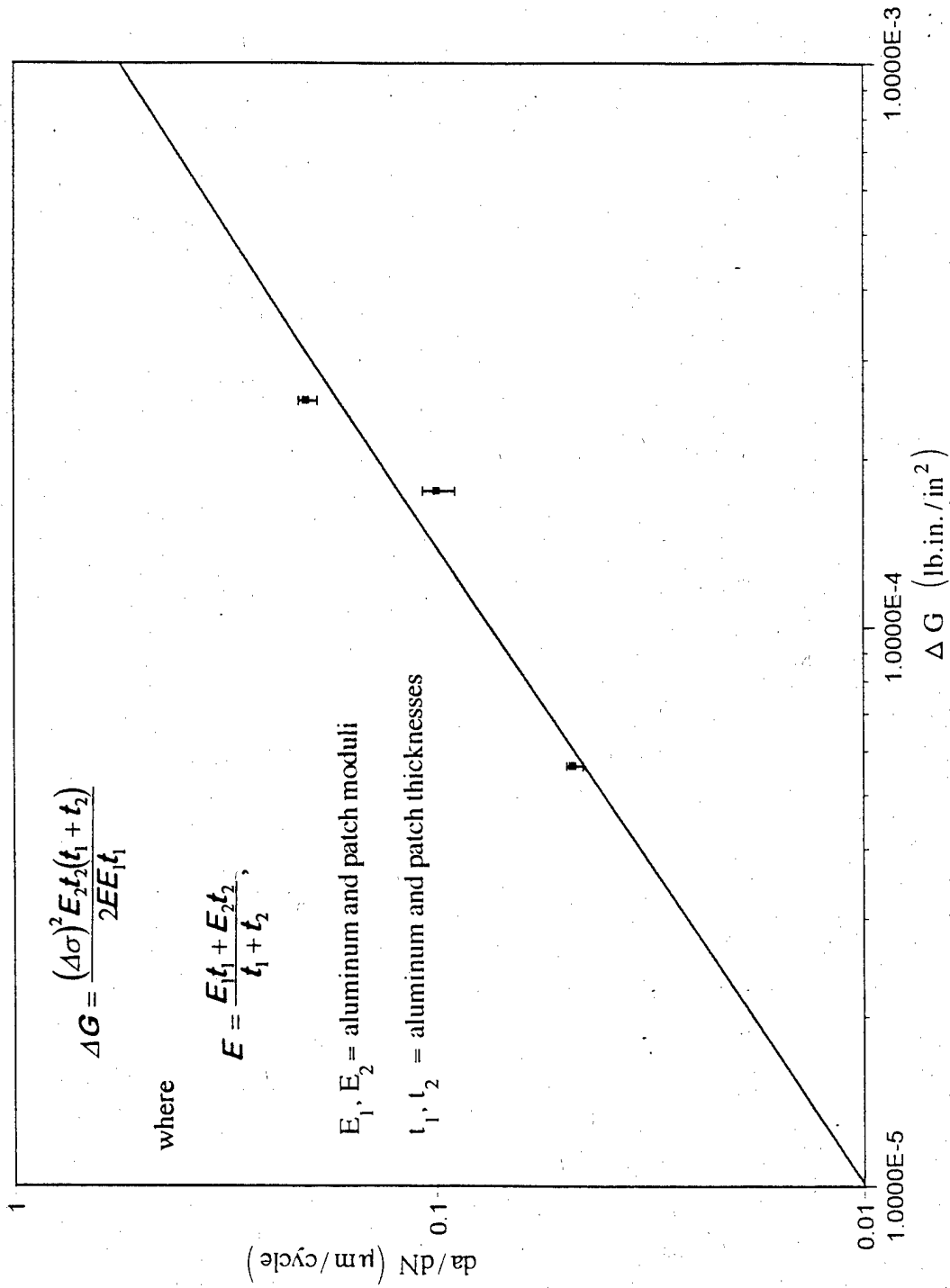


Fig. 24 Debond Growth Rate vs. Range of Strain Energy Release Rate.

3.4 Conclusions

Composite patches are very effective in slowing down damage growth in cracked metallic substrates, such as aluminum. The most common form of fatigue damage in a cracked metallic panel with a composite patch is debonding around the propagating crack. Crack propagation in a metallic panel with a composite patch is related to the interfacial fracture toughness of the adhesive joint under fatigue conditions.

Experimental measurements of crack propagation in an unpatched metallic panel and debond growth of a patch provide the needed input for calculation of crack propagation in a cracked panel with a repair patch and for prediction of the geometry of the debonded region. Thus, the life of a patched cracked specimen could be predicted.

References

1. A. Charewicz and I. M. Daniel, "Damage Mechanisms and Accumulation in Graphite/Epoxy Laminates," *Composite Materials: Fatigue and Fracture*. ASTM STP 907, ed. H. T. Hahn, ASTM, Philadelphia, 1986, pp. 274-297.
2. I. M. Daniel and J.-W. Lee, "Damage Development in Composite Laminates under Monotonic Loading," *J. Composites Technology and Research*. Vol. 12. No. 2. 1990, pp. 98-102.
3. I. M. Daniel, S. C. Wooh and J. W. Lee, "Nondestructive Evaluation of Damage Development in Composite Materials," *Elastic Waves and Ultrasonic Nondestructive Evaluation*, S. K. Datta, J. D. Achenbach, and Y. S. Rajapakse eds., Elsevier, 1990, pp. 183-189.
4. R. Talreja, "Transverse Cracking and Stiffness Reduction in Composite Laminates," *J. Comp. Mat.*, Vol. 19, 1985, pp. 355-375.
5. S. L. Ogin, P. A. Smith, and P. W. R. Beaumont, "Matrix Cracking and Stiffness Reduction During the Fatigue of a $[0/90_2]_s$ GFRP Laminate," *Composites Science and Technology*, Vol. 22, 1985, pp. 23-31.
6. C.-L. Tsai and I. M. Daniel, "The Behavior of Cracked Crossply Composite Laminates under General In-plane Loading," *Damage in Composite Materials*, ed. G. Z. Voyiadjis, Elsevier, 1993, pp. 51-66.
7. S. C. Wooh, I. M. Daniel and H. J. Chun, "Real-time Monitoring of Damage Development in Crossply Composite Laminates by Means of Ultrasonic and Acoustic Emission Methods," *Review of Progress in Quantitative Nondestructive Evaluation*. Vol. 14, ed. by D. O. Thompson and D. E. Chimenti, Plenum Press, New York, 1995, pp. 1383-1390.

8. S. C. Wooh, I. M. Daniel and H. J. Chun, "Real-time Ultrasonic and Acoustic Emission Monitoring of Damage in Graphite/Epoxy Laminates," *Composites Engineering*, Vol. 5, No. 12, 1995, pp. 1403-1412.
9. S. C. Wooh and I. M. Daniel, "Enhancement Techniques for Ultrasonic Nondestructive Evaluation of Composite Materials," *J. of Engineering Materials and Technology*, Vol. 112, 1990, pp.175-182.
10. S. C. Wooh and I. M. Daniel, "Real-time Ultrasonic Monitoring of Fiber-Matrix Debonding in Ceramic-Matrix Composite," *Mechanics of Materials*, Vol. 17, 1994, pp. 379-388.
11. A. A. Baker, "Repair of Defective Metallic Aircraft Components with Advanced Fibre Composites - An Overview of Australian Work," *Composite Structures*, Vol. 2, 1984, pp. 153-181.
12. A. A. Baker, R. J. Callinan, M. J. Davis, R. Jones and J. G. Williams, "Application of BFRP Crack Patching of Mirage III Aircraft," *Proceedings 3rd Int. Conf. Composite Materials*, ICCM 3, Paris, Pergamon Press, Oxford, 1980. pp. 1424-1438.
13. A. A. Baker, "Fibre Composite Repair of Cracked Metal Aircraft Components - Practical and Basic Aspects," *Composites*, Vol. 18, No. 4, 1987, pp. 293-308.
14. C. L. Ong and S. B. Shen, "Study on Composite-Patching Repairs for Metallic Aircraft Structures," *Proceedings of 36th Int. SAMPE Symposium*, Vol. 36, eds. J. Stinson, R. ADsit and F. Gordaninejad, April 15-18, 1991, pp. 2291-2305.
15. S. M. Atluri, J. H. Park, E. F. Punch, P. E. O'Donoghue and Rhys Jones, "Composite Repairs of Cracked Metallic Aircraft Structures," DOT/FAA/CT 92/32 Report, May 1993.
16. H. Aglan, "Fatigue Lifetime Assessment of Adhesive Joints by Ultrasonic and Thermal Wave Imaging," *J. Adhesion Scie. and Technology*, Vol. 8, No. 2, 1994, pp. 101-115.
17. H. Aglan and Z. Abdo, "An Innovative Approach to Fatigue Disbond Propagation of Adhesive Joints," *J. Adhesion Scie. and Technology*, Vol. 10, No. 3, 1996. pp. 183-198.
18. H. Aglan, T. Rowell, Z. Zhang, T. Ahmed and R. Thomas, "Evaluation of Bonded Boron/Epoxy Repairs on Aircraft Skin with Simulated Damage," presented at Review of Progress in QNDE, San Diego, 1997.
19. C. T. Sun, J. Klug and C. Arendt, "Analysis of Cracked Aluminum Plates Repaired with Bonded Composite Patches," *AIAA Journal*, Vol. 34, No. 2, 1996. pp. 369-374.
20. L. Minnetyan and C. C. Chamis, "Structural Durability of Damaged Metallic Panel Repaired with Composite Patches," *J. Reinforced Plastics and Composites*, Vol. 16, No. 3, 1997, pp. 200-216.
21. A. N. Rider, D. R. Arnott, A. R. Wilson and O. Vargas, "Influence of Simple Surface Treatments on the Durability of Bonded Aluminum Alloy Plates," *Mat. Scie. Forum*, Vols. 189-190, 1995, pp. 235-240.

PERSONNEL SUPPORTED ON GRANT

Professor I. M. Daniel, Principal Investigator

Drs. H. J. Chun and S. C. Wooh, Post-Docs

J. J. Luo, K. Durkin, Graduate Students

PUBLICATIONS

S. C. Wooh, I. M. Daniel and H. J. Chun, "Real-time Monitoring of Damage Development in Crossply Composite Laminates by Means of Ultrasonic and Acoustic Emission Methods," *Review of Progress in Quantitative Nondestructive Evaluation*, Vol. 14, ed. by D. O. Thompson and D. E. Chimenti, Plenum Press, New York, 1995. pp. 1383-1390.

S. C. Wooh, I. M. Daniel and H. J. Chun, "Real-time Ultrasonic and Acoustic Emission Monitoring of Damage in Graphite/Epoxy Laminates," *Composites Engineering*, Vol. 5, No. 12, 1995, pp. 1403-1412.

I. M. Daniel, J.-J. Luo and H.-M. Hsiao, "Acousto-Ultrasonic Techniques for Evaluation of Bond Integrity of Composite Repair Patches," *Review of Progress in Quantitative Nondestructive Evaluation*, Vol. 17, ed. by D. O. Thompson and D. E. Chimenti, Plenum Press, New York, 1998, pp. 1331-1338.

NOTICE OF SUBMISSION (NOS)

THIS DOCUMENT IS UNCLASSIFIED

DATE 01-01-01 BY 1045

REASON: 1.1.1

CLASSIFICATION